



Spectroscopy of excited states in ^{94}Pd and
development of tools
for Slowed Down Beams at FAIR

Inaugural-Dissertation
zur
Erlangung des Doktorgrades
der Mathematisch-Naturwissenschaftlichen Fakultät
der Universität zu Köln

vorgelegt von
Aleksandrina Yaneva
aus Varna

Köln 2024

Berichtersteller:

Prof. Dr. Jan Jolie
Prof. Dr. Peter Reiter

Tag der mündlichen Prüfung:

17.09.2024

Abstract

This doctoral thesis presents results from the first experiment of the DESPEC campaign performed at GSI Helmholtzzentrum für Schwerionenforschung (Darmstadt, Germany) as part of FAIR Phase-0. The goal of the experiment was precise measurement of electromagnetic transition rates in the $T_z = +1$ ^{94}Pd nucleus, in particular the lifetimes of the yrast $I^\pi = 8^+$ and 6^+ states below the $I^\pi = 14^+$, $T_{1/2} = 499(13)$ ns isomer. The nuclei of interest were produced by the fragmentation of ^{124}Xe primary beam impinging on a 4 g/cm^2 ^9Be target, after being accelerated to 982 MeV/u in the UNILAC and the SIS18 synchrotron. The reaction products were separated and identified on an event-by-event basis in the FRS and then transported to the final focal plane, where the DESPEC setup was located. There the fragments were implanted in the AIDA active stopper. Subsequent γ -rays following the decay of populated isomeric states in the nuclei of interest were detected by the GALILEO and FATIMA detector arrays. The half-life of the 8^+ state in ^{94}Pd was measured by employing the Generalized Centroid Difference method, which uses the fast-timing methodology. In addition, a limit for the half-life of the 6^+ state in ^{94}Pd was obtained. The experimental electromagnetic transition rates $B(E2)$ were determined using the measured lifetimes and the values were compared to shell-model calculations, employing different interactions and model spaces.

This thesis also reports on an experiment aimed at testing detector prototypes for future HISPEC-10 slowed-down beam campaigns at FAIR. With the goal of observing Coulomb excitations of even-even stable nuclei, a ^{64}Ni (or similar) beam was requested impinging on a ^{197}Au target. However, only a ^{208}Pb primary beam was available and the experiment was finally performed using this beam. As the ^{208}Pb primary beam at 250 MeV/u reaches the experimental cave, it interacts with a thick β Plastic detector, the signal from which was used as the trigger for all other detector systems. A mechanical structure holding degraders with different thicknesses was used to slow down the beam. For ion tracking and time-of-flight measurement three MCP detectors were used. After interacting with the ^{197}Au target, located downstream of the MCPs, the beam was stopped in a ΔE -E telescope, used for tracking and identification. For detecting γ -rays two three-fold DEGAS HPGe clusters were used, pointed towards the target. The data from this experiment is still being analyzed, but some findings are reported in this work.

Contents

1	Introduction	1
1.1	Physics motivation	2
2	Theoretical background	7
2.1	The Nuclear Shell Model	7
2.1.1	Independent particle model. Single-particle states.	8
2.1.2	Many-body system. Residual interaction.	11
2.2	Isotopic spin	13
2.3	Electromagnetic transition rates and Weisskopf estimates	14
2.4	Interaction of photons with matter	17
2.5	The fast timing technique	17
3	Experimental setup	21
3.1	The GSI accelerator facility	21
3.2	Production of exotic nuclear beams	22
3.3	The fragment separator	23
3.3.1	The $B\rho$ - ΔE - $B\rho$ separation method	24
3.3.2	The ToF- $B\rho$ - ΔE identification method	25
3.4	The decay spectroscopy setup	28
3.4.1	The implantation setup	28
3.4.2	The FATIMA detector array	31
3.4.3	The high-purity germanium cluster detectors	32
3.4.4	Data acquisition	33
4	Data Analysis	35
4.1	Calibration of the FRS detectors	35
4.1.1	Time-of-flight calibration	36
4.1.2	MUSIC velocity calibration	36
4.1.3	Z calibration and drift correction	38
4.1.4	Angle correction	39
4.1.5	Selecting the ions of interest	40

4.2	Calibration of the FATIMA detectors	41
4.2.1	Energy calibration	41
4.2.2	Time calibration	44
4.3	Prompt Response Difference and PRD curve	47
4.4	Cleaning conditions	48
4.5	E_γ - E_γ - ΔT matrices	50
4.6	Background treatment	51
4.6.1	Background treatment for exponential fit method	52
4.6.2	Background treatment for the GCD method	54
5	Results	59
5.1	^{96}Pd benchmark case	59
5.2	^{94}Pd case	62
6	Discussion	67
7	The HISPEC Slowed-Down Beam concept and test experiment	75
7.1	Experimental setup	76
7.1.1	β Plastic	77
7.1.2	Micro-Channel Plates	77
7.1.3	ΔE - E telescope	80
7.1.4	DEGAS	82
7.1.5	Data acquisition	83
7.2	Preparation and execution of the experiment	83
7.3	Data analysis and results	83
8	Conclusion	85
	Bibliography	86
	List of Publications	101
	Acknowledgements	103
	Curriculum vitae	105
	Erklaerung zur Dissertation	107

Chapter 1

Introduction

The atomic nucleus is a complex system of (positively charged) protons and (neutral) neutrons. The fact that nuclei exist despite the influence of the repulsive Coulomb force acting between protons, leads to the conclusion that a strong attractive force exists. This so called nuclear force is able to overcome the Coulomb interaction and binds the nucleons together.

From experimental studies of nuclear radii, separation energies, binding energy per nucleon, etc. some of the basic characteristics of this strong force have been established: short range attractive force that saturates. Along with the existence of magic numbers (either for protons or for neutrons or for both), empirical data also suggests that the approximation of independently moving nucleons in an average central potential is valid. The latter represents the basic assumption of the nuclear shell model [1, 2], which was developed in an attempt to explain the properties of atomic nuclei.

In terms of the independent motion hypothesis, the shell model allows for the many-body nuclear problem to be solved by solving the single particle (in a central potential) problem for each nucleon individually. However, the interaction between nucleons is not entirely accounted for by the central potential. Thus, the so called residual interaction is treated as a perturbation to the independent motion and causes configuration mixing. The nucleus is described in terms of energy levels or orbitals (separate for protons and neutrons), where different orbitals are grouped in shells with gaps in between shells in the order of a few MeV. The orbitals are filled according to the Pauli principle forming a fully filled closed shell core and a partially filled shell, containing the valence nucleons.

The shell model succeeds in reproducing the magic numbers as well as many other nuclear properties such as energy levels, spins, magnetic moments, etc. It gives good descriptions of stable doubly magic nuclei, however becomes less reliable for nuclei located farther away from the valley of stability. In this sense, the doubly-magic neutron-deficient ^{100}Sn nucleus and its neighbours provide the

perfect base to test shell model predictions at the $N = Z = 50$ double shell closure.

1.1 Physics motivation

^{100}Sn ($N = Z = 50$) is the heaviest self-conjugate doubly-magic nucleus. The nuclear structure of the hole states in the region "south-west" of ^{100}Sn (Fig. 1.1) is dominated by the $0g_{9/2}$ orbit, which is part of the $N = 4$ gds harmonic oscillator shell. It is energetically and by spin very well separated from the lower $N = 3$ pf-shell, allowing only even-particle even-hole excitations into the intruder orbit. To describe the structure of high-spin orbitals, the quantum number seniority ν is defined, counting the number of unpaired nucleons (separately for protons and neutrons), which occupy the same shell-model orbital. Due to the strong spatial overlap of proton- and neutron-hole wave functions, strong proton-neutron (pn) correlations are induced, giving rise to unique structural features such as spin-gap, seniority and parity-changing isomerism, as well as proton-neutron pairing and seniority induced symmetries. This makes the region "south-west" of ^{100}Sn one of the most attractive areas for both experimental and theoretical studies in the nuclear chart [3, 4].

Early shell-model studies employing empirical interactions in the $\pi\nu(1p_{1/2}, 0g_{9/2})$ model space [5–8] to this day provide accurate predictions for the structure of

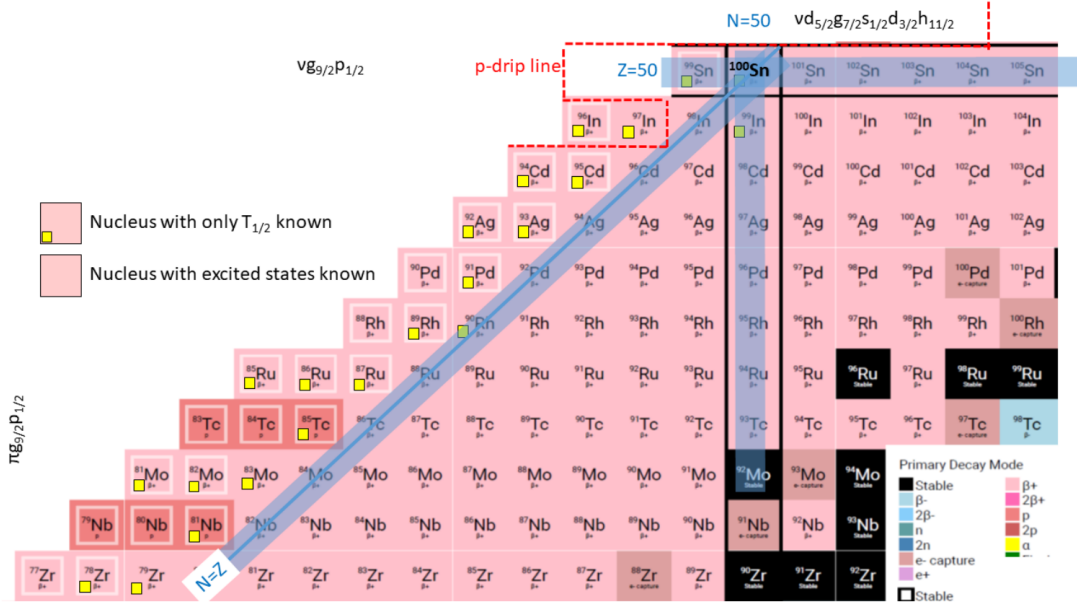


Figure 1.1: Partial chart of nuclei in the ^{100}Sn region showing experimental information on the ground-state lifetime and excited states. The yellow square indicates nuclei, for which no excited states have been reported and only the ground-state lifetime is known. Taken from Ref.[4]

^{100}Sn and its neighbours. More recent efforts include calculations using empirical [9] and realistic [10, 11] interactions in the full $\pi\nu(f_{5/2}pg_{9/2})$ model space as well as Large Scale Shell Model (LSSM) calculations using the Nowacki-Sieja interaction in the upper $\pi\nu(gds)$ shell [12]. The topic of seniority breaking (or partial seniority conservation) in the $0g_{9/2}$ orbit is excessively discussed in the Ref. [13–21]. Moreover, the influence of remnants of the seniority level scheme in the open $\pi\nu(g_{9/2})$ orbitals is addressed in Ref. [22].

Experimental efforts aimed at studying the structure of nuclei approaching ^{100}Sn include the discovery of core-excited isomers in ^{98}Cd [23, 24] and ^{96}Ag [25]; spectroscopy of ^{92}Pd [26]; decay studies of the spin-gap isomers and yrast sequence in $^{96,97}\text{Cd}$ [12, 27–29] and ^{94}Ag [30, 31]; isomer, β and β -proton decay spectroscopy of fragments in the region [32–34]; as well as the discovery of delayed rotational alignments in the even-even $N = Z$ nuclei ^{84}Mo [35] and ^{88}Ru [36].

In the $\pi\nu(g_{9/2})$ orbital the proton-neutron interaction strength manifests in the strongly-binding $T = 0$ $(g_{9/2})^2$, $I^\pi = 9^+$ isoscalar two-body matrix element (TBME), which is comparable to the $T = 1$ isovector pairing [5, 6]. In order to shed light onto the role of pn pairs with maximum aligned spin of 9^+ in the ^{96}Cd , ^{94}Ag and ^{92}Pd $N = Z$ nuclei, a series of multi-step shell-model and Interacting Boson Model (IBM) studies were performed [26, 37–40]. The contents of several pn -pairs within the nuclear wave functions in the three nuclei were analyzed. Overlap between the 9^+ -boson wave functions and the exact shell-model was established only at low- and high-spin states, with minimal overlap observed at intermediate spin levels [40]. However, these conclusions are subject to changes, when taking into account the full $\pi\nu(f_{5/2}pg_{9/2})$ and $\pi\nu(gds)$ model spaces.

Predictions about the B(E2) values and spectroscopic quadrupole moments in the ^{96}Cd and ^{92}Pd nuclei for these model spaces were compared to results from a pure $(g_{9/2})^n$ approach in Ref. [41]. For low-spin states with $I \leq 6$ the three approaches show identical results for excitation energies and B(E2) values, however considerable differences are displayed for quadrupole moments (currently experimentally inaccessible). Furthermore, signs of quadrupole deformation can be found for lower- Z nuclei in the $g_{9/2}$ orbital [36]. With increasing spin and in nuclei closer to the $N = Z = 50$ doubly-magic closure, this deformation is expected to evolve due to model space exhaustion, resulting in the gradual reduction in collectivity.

The $T_z = +1$ ^{94}Pd nucleus is situated at a crucial point of this evolution. With its four proton and two neutron holes in the $g_{9/2}$ orbital below the ^{100}Sn core nucleus, ^{94}Pd is the neighbour of the even-even $N = Z$ systems ^{96}Cd and ^{92}Pd and represents the $T = 1$ isospin partner for states in the odd-odd $N = Z$ system ^{94}Ag . In order to demonstrate the role of the isoscalar ($T = 0$) versus isovector

($T = 1$) pn interaction, in Fig. 1.2 the experimental spectra of $^{92,94,96}\text{Pd}$ nuclei are compared to shell-model calculated level schemes from Ref. [6]. ^{96}Pd displays a typical seniority type spectrum, maintained by the $T = 1$ pn interaction, and is well reproduced by the shell-model calculations. On the other hand, ^{92}Pd shows an equidistant spectrum mainly due to the $T = 0$ part of the pn interaction. In this evolution from the seniority type $N = 50$ ^{96}Pd towards the $N = Z$ ^{92}Pd , which exhibits strong pn correlations, ^{94}Pd displays an intermediate character.

Experimental information on the excited states in ^{94}Pd is available up to spin-parity $I_\pi = (20^+)$. It was obtained from decay studies of the $I_\pi = 14^+$ and 19^- isomeric states in ^{94}Pd [42–44] as well as β -decay studies of ^{94}Ag [30, 31]. Fig. 1.2 demonstrates good agreement between the experimental and shell-model calculated level schemes, however no experimental information is available on lifetimes and $B(E2)$ values of excited states below the $I_\pi = 14^+$ isomer. This points to the main goal of the experiment presented in the current work and namely, the measurement of the half-lives of the $I_\pi = 8^+$ and 6^+ states in ^{94}Pd . This lifetime measurement will provide access to the nuclear properties of these

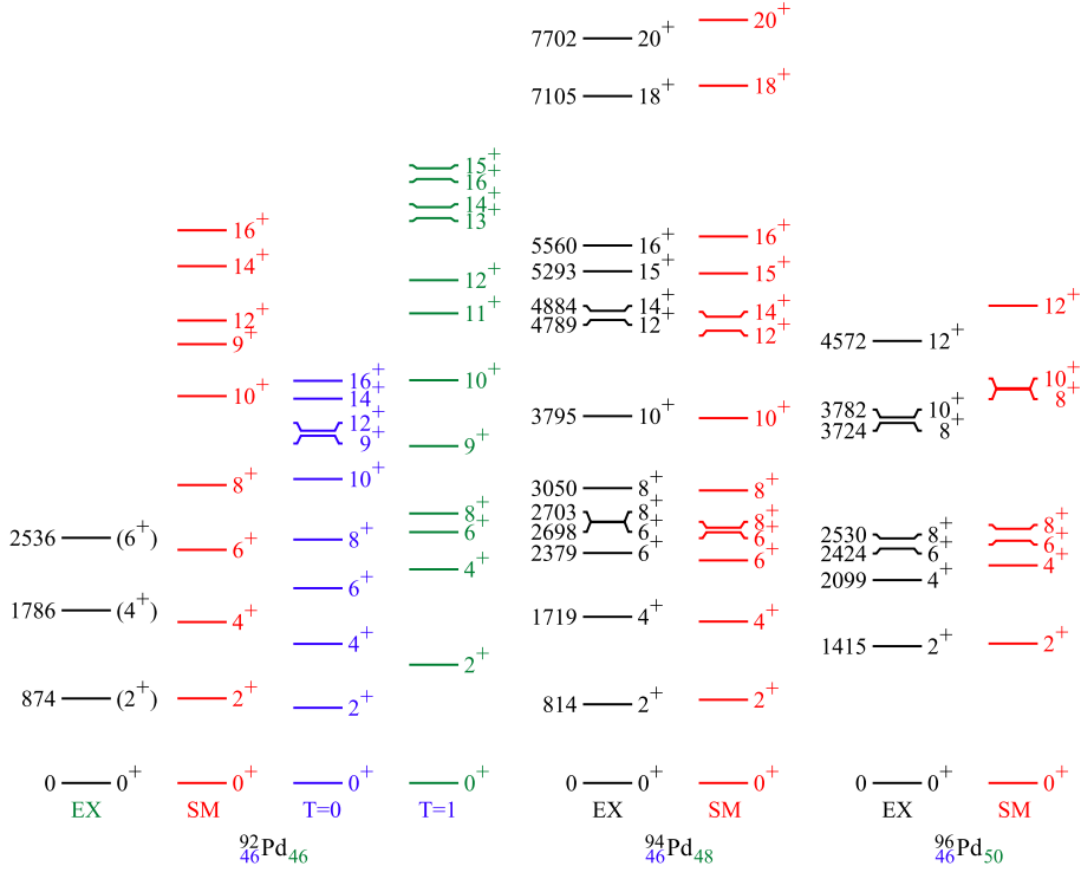


Figure 1.2: Experimental and shell-model data showing the evolution of the proton–neutron interaction and even-parity yrast structure for $^{92,94,96}\text{Pd}$. Taken from Ref. [3]

states. Studies of the detailed structure of the 8^+ seniority remnant in ^{94}Pd will reveal the interplay between the isovector and isoscalar coupling of the pn pairs. Moreover, in terms of seniority-mixed states the structure of ^{94}Pd may provide an indication of emerging collectivity, when nucleons are removed from the doubly-magic system ^{100}Sn . The emergence of deformation is supported by predictions indicating that favored pn $T = 0$ pairs arrange in a spin-aligned configuration, forming shear blades characteristic of Anti-Magnetic Rotational (AMR) behavior in the yrast band of ^{92}Pd [45]. A recent theoretical study using the EXVAM (Excited VAMPIR) beyond-mean-field approach [46] highlights the connection between the $T = 0$ pn -pairing component and the emergence of prolate deformation and shape coexistence in ^{94}Pd .

Chapter 2

Theoretical background

Any theoretical model attempting to describe the atomic nucleus should be able to reproduce existing experimental findings as well as make accurate predictions about future experimental results. In this context, one of the most successful and easy to understand models is the Shell Model (SM). It performs well in the vicinity of stable doubly-magic nuclei, reproducing accurately many nuclear properties like spin, parity and energy of both ground and excited states. Moreover, this is also the case for systems far from stability, but close to magic numbers like $^{100,132}\text{Sn}$. However, as one moves farther away from the valley of stability and reaches nuclei with extreme neutron-to-proton ratios, the SM becomes less reliable and additional correction needed to be considered.

In this chapter, the basic concept of the nuclear shell model will be introduced, discussing the independent particle model and the residual interaction. A description of electromagnetic transition rates and Weisskopf estimates will be given and finally, the nuclear structure in the vicinity of ^{100}Sn will be explored, with an emphasis on the ^{94}Pd nucleus.

2.1 The Nuclear Shell Model

According to the atomic shell model [47], each electron moves independently in an external central Coulomb potential, created by the positively charged nucleus. The nuclear shell model [1, 2], as an attempt at using a similar approach to explain the properties of atomic nuclei, assumes that each individual nucleon moves independently in an average central potential. However, this potential is not external (like the Coulomb potential created by the nucleus in the atomic shell model), but rather created by the other nucleons in the nucleus (nuclear interaction). Another essential difference between the two models is the existence of two types of particles (protons and neutrons) in the nucleus, which gives rise to a new quantum number called isospin.

From the point of view of quantum mechanics, the Hamiltonian for a nuclear system, consisting of A number of nucleons moving independently in a mean field potential, can be expressed as

$$H_0 = \sum_{i=1}^A [T_i + U_i(r)], \quad (2.1)$$

where T_i denotes the kinetic energy and $U_i(r)$ is the single-particle potential, r representing spatial coordinates. However, the nucleus is a many-body system, for which the Hamiltonian consist of the kinetic term $\sum_i T_i$ and the two-particle interaction $\sum_{i<j} V_{ij}(r)$:

$$H = \sum_{i=1}^A T_i + \sum_{i,j=1}^A V_{ij}(r). \quad (2.2)$$

Using Eq.2.1, Eq.2.2 can be rewritten as

$$H = \sum_{i=1}^A [T_i + U_i(r)] + \left(\sum_{i,j=1}^A V_{ij}(r) - \sum_{i=1}^A U_i(r) \right) = H_0 + H_{res}. \quad (2.3)$$

Here H_0 is the Hamiltonian of the independent particle model and H_{res} represents a residual interaction, showing that the nucleons in the atomic nucleus do not move completely independently.

Only for nuclei with a single nucleon outside a closed shell, can the independent particle model be used. The nucleon single-particle energies are then given by the solutions to the Schrödinger equation with H_0 (more details in Section 2.1.1).

In the case of nuclei with more than one valence nucleon, the residual interaction causes a coupling effect and gives rise to the most important nuclear features: spin, magnetic dipole and electric quadrupole moments. The residual interaction, represented by H_{res} , can be evaluated using the two-body matrix elements (TBME) with the help of the perturbation theory (more details in Section 2.1.2).

2.1.1 Independent particle model. Single-particle states.

An important step in developing the nuclear shell model is choosing the potential (the type of interaction). To a first approximation, the interaction between a single nucleon and all other nucleons in the nucleus can be simplified to a central potential. This assumption is the basis for the independent particle model.

The single particle energies (SPE) e_a can be obtained by solving the Schrödinger

equation:

$$[T + U(r)] \phi_a(r) = e_a \phi_a(r), \quad (2.4)$$

where $\phi_a(r)$ are the single-particle wave functions, a denoting the quantum numbers of a specific state. For a nucleus with A number of nuclei the Schrödinger equation can be expressed in terms of the independent particle model:

$$H_0 \Phi_a = E_a \Phi_a, \quad (2.5)$$

where H_0 is given by Eq.2.1, the eigenfunctions $\Phi_a = \phi_{a_1} \dots \phi_{a_A}$ are constructed as the product of A single-particle functions and the eigenenergies are given by:

$$E_a = \sum_{i=1}^A e_{a_i}. \quad (2.6)$$

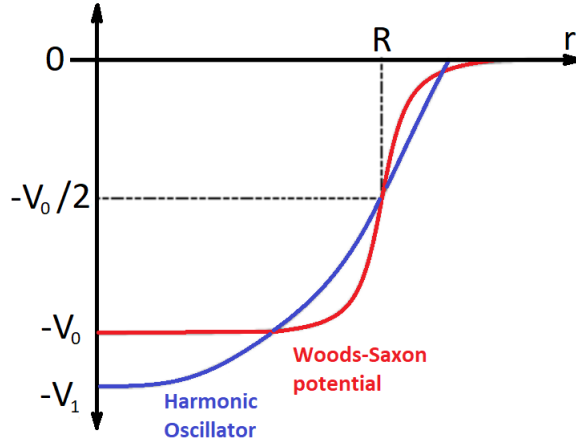


Figure 2.1: Harmonic oscillator potential and Woods-Saxon potential

In order to solve the Schrödinger equation and determine the single-particle eigenvalues (E_a), the potential $U(r)$ needs to be specified. Assuming a simple harmonic oscillator potential (Fig.2.1)

$$U(r) = \frac{1}{2}M\omega^2r^2, \quad (2.7)$$

only the lowest magic numbers are reproduced (Fig. 2.2). Here M denotes the mass of the particle, ω is the angular frequency and r is the distance between the nucleon and the origin of the coordinate system.

A more realistic potential is the Woods-Saxon potential (Fig. 2.1):

$$U(r) = \frac{-U_0}{1 + e^{(r-R)/a}}, \quad (2.8)$$

where $U_0 \approx 50$ MeV is the well depth, $R = 1.2 A^{1/3}$ fm is the mean radius of the nucleus and $a \approx 0.7$ fm is the diffuseness, which describes the skin thickness as the distance over which the potential changes from $0.9V_0$ to $0.1V_0$ [48, 49]. Fig. 2.2 shows the result of using this potential. Even though the effect of the degeneracy over the angular momentum (l) is removed, still only the lowest magic numbers are reproduced, similarly to the case of using the harmonic oscillator potential.

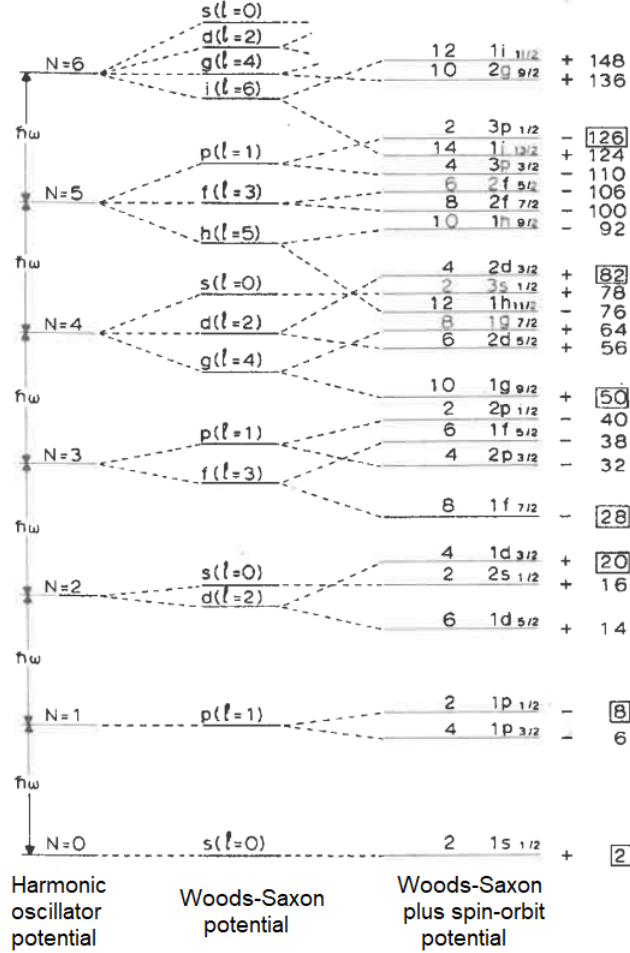


Figure 2.2: Schematic representation of the single-particle energies of Harmonic Oscillator (HO), Woods-Saxon and Woods-Saxon + spin-orbit potentials (Figure taken from Ref.[49]). Only the lowest magic numbers are recreated with the HO and Woods-Saxon interactions. On the other hand, the splitting due to the the spin-orbit term allows for all experimentally determined magic numbers to be reproduced.

In order to fully reproduce the magic numbers an additional term for the spin-orbit force has to be added to the Woods-Saxon potential. To label the states the total angular momentum j is used, which can be expressed in terms of the angular momentum (l) and the spin (s) in the following way: $j = l + s$. Using

this connection, the contribution of the spin-orbital term can be evaluated [48]:

$$l.s = \begin{cases} +\frac{\hbar^2}{2}l & \text{for } j = l + \frac{1}{2} \\ -\frac{\hbar^2}{2}(l+1) & \text{for } j = l - \frac{1}{2} \end{cases} \quad (2.9)$$

and Eq.2.8 can be expanded to

$$U(r) = \frac{-U_0}{1 + e^{(r-R)/a}} + f(r) l.s, \quad (2.10)$$

where the function $f(r)$ defines the strength of the spin-orbit interaction, which depends on the radial coordinate r . Solving the Schrödinger equation using this potential leads to the splitting of the $j = l \pm \frac{1}{2}$ degenerate levels.

It is important to note that for all potentials used in this section, only the neutron shells were considered. In order to determine the single-particle states of the proton shells, an addition of Coulomb potential has to be considered due to the repulsive force between protons.

2.1.2 Many-body system. Residual interaction.

As previously explained, the independent particle model is only a first order approximation of the shell model. To account for the fact that the nucleons in the atomic nucleus do not move entirely independently, the complete Schrödinger equation

$$H | \Psi \rangle = E | \Psi \rangle, \quad (2.11)$$

with the many-body Hamiltonian represented by Eq.2.3 needs to be solved.

In terms of the perturbation theory, the many-body Hamiltonian is considered a sum of the unperturbed (independent-particle) Hamiltonian H_0 and the small perturbation H_{res} . The wave function Ψ_p for a particular state can be expanded to

$$| \Psi_p \rangle = \sum_a c_{ap} | \Phi_a^{(0)} \rangle, \quad (2.12)$$

using the $\Phi_a^{(0)}$ unperturbed basis, each function being a product of single-particle wave functions $\Phi_a^{(0)} = \phi_{a_1} \dots \phi_{a_A}$. With the restriction of the many-nucleon configuration to two-body interactions, the total energy of the state can be obtained by solving the equation

$$\begin{aligned} E_p c_{bp} &= \sum_a \langle \Phi_b^{(0)} | H | \Phi_a^{(0)} \rangle c_{ap} \\ &= \sum_a \langle \Phi_b^{(0)} | H_0 + H_{res} | \Phi_a^{(0)} \rangle c_{ap}. \end{aligned} \quad (2.13)$$

Here $\Phi_a^{(0)}$ are the eigenfunctions of the unperturbed (independent-particle) Hamiltonian H_0 with corresponding eigenenergies E_a according to Eq.2.6 (see Section 2.1.1). This allows for the total energy to be expressed as a sum of single-particle energies and the contribution of the residual interaction via the matrix equation

$$E_p c_{bp} = \sum_a H_{ba} c_{ap} \quad (2.14)$$

$$H_{ba} = E_a^{(0)} \delta_{ab} + \langle \Phi_b^{(0)} | H_{res} | \Phi_a^{(0)} \rangle \quad (2.15)$$

The terms in the brackets represent the Hamiltonian matrix. The second term is known as the two-body matrix element (TBME) and is used as means to evaluate the effects of the residual interaction. In some cases there could also be a need to consider three-body matrix elements.

The main task of shell model calculations is to determine the interaction energy (E) by diagonalizing the Hamiltonian matrix. However, as the number of nucleons increases the number of orbitals that need to be taken into account also grows, which in turn leads to the dimension of the matrix to rise. The diagonalization of the matrix for nuclei with large masses for the full configuration space is usually very difficult (and/or impossible) due to limitations in computational power. Therefore, the nucleus is considered as combination of a completely filled shell of non-interacting particles (closed shell or inert core) and a partially filled shell of orbitals containing the valence nucleons (valence space). The assumption of an inert core allows for the matrix dimension and in turn the model space to be reduced. The nucleons in the valence space interact via the residual interaction. Due to the restriction of the model space, the general Hamiltonian (Eq.2.2) needs to be adapted to an effective one, i.e. the effective interaction is the residual interaction affecting the valence nucleons (outside of the core).

In reality a fully inert core does not exist. The addition of nucleons to closed shells causes distortions in the form of a polarization effects, which can induce excitations to higher shells. In order to take these polarization effects of the core into account, the concept of effective charge for protons and neutrons is introduced. The effective charge is dependent on the occupied orbitals and thus the model space. These effective charges renormalized by the core polarization can be determined either empirically from experimental data or theoretically using the reaction matrix derived from the nuclear force.

As already discussed, the model space consist of information on the shell model orbitals and their occupancy. For different regions in the nuclear chart, different model spaces and effective interactions are employed. There are three approaches to derive the effective residual interaction and evaluate the TBME:

empirical, schematic and realistic.

- Empirical interactions are extracted from experimental data using information on the binding energies of closed shell nuclei and their one- and two-particle/hole neighbours. For not too large model spaces the SPE and TBME (only diagonal) can be determined by utilizing the χ^2 -fitting (least-squares) method applied to a data set of experimental binding and excitation energies.
- It is possible to explain some of the basic nuclear properties using a simple schematic nucleon-nucleon interactions. Some example of such interactions are the Yukawa, Gaussian, delta and surface delta types [49, 50].
- Realistic interactions are derived using the nucleon-nucleon (NN) potential obtained from experimental NN scattering data. An important characteristic of any realistic NN potential is the strong, short-range repulsive core, which however is not suitable for treatment in terms of the perturbation theory. In order to remove the repulsion effect from the NN interaction, the G-matrix [10] is produced according to the Brückner theory [51]. A mass (A) dependence is introduced when calculating the TBME, due to the need to account for the valence space of occupied and empty (scattering) orbitals defined for a particular reference doubly-magic core. However, the SPE cannot be extracted in this way and are usually taken from experimental data.

2.2 Isotopic spin

If the effects of the Coulomb force on nuclear properties are neglected, the characteristics and behaviour of the proton and neutron are identical in most aspects. In addition to having similar masses, the charge symmetry and charge independence of the nuclear force allow for the treatment of the proton and neutron as two separate states of the same particle, the nucleon. A new quantum number is defined, called isotopic spin (or isospin), which differentiates between the two types of nucleons. The isospin (t) of a single nucleon is defined, analogously to the intrinsic spin, as

$$t = \frac{1}{2} \tag{2.16}$$

with a third projection of

$$t_z = \begin{cases} +\frac{1}{2} & \text{for neutrons} \\ -\frac{1}{2} & \text{for protons} \end{cases} . \tag{2.17}$$

The isospin follows identical coupling rules to the ordinary angular momentum vectors. For a many-particle system with A number of nucleons, the total isospin T is defined as

$$T = \sum_{i=1}^A t_i, \quad (2.18)$$

and its third projection is given by

$$T_z = \sum_{i=1}^A t_{z,i}, \quad -T \leq T_z \leq +T. \quad (2.19)$$

Then for each value T a multiplet with $2T+1$ members exists, which is characterized by T_z . For example, a two-nucleon system can have a total spin of $T = 0$ or 1 with four possible components of the third projection: $T_z = -1$ for two protons, $T_z = +1$ for two neutrons and two combinations with $T_z = 0$ for one proton and one neutron (see Fig. 2.3). Taking the charge independence of the nuclear force into account, the interactions in $T = 1$ ($T_z = -1, 0, 1$) states should be the same, therefore the states should have the same energy forming a triplet. However, the interaction and energy of the $T=0$ singlet can be different.

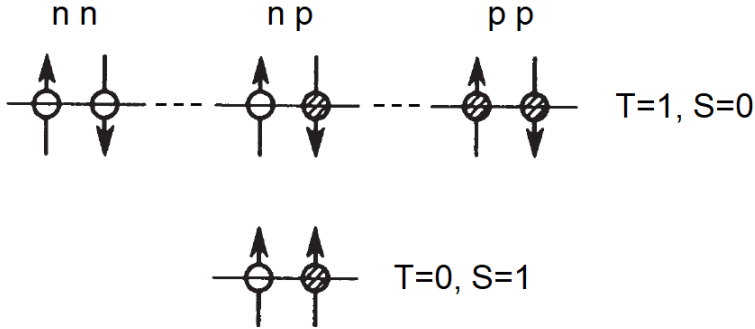


Figure 2.3: Schematic illustration of the possible two-nucleons configurations: the $T=1$ isospin triplet on the top and the $T=0$ singlet on the bottom. Here S is the intrinsic spin.

The importance of the isospin concept is expressed by the conservation law, which requires the preservation of isospin for transitions/decays caused by the influence of the strong interaction.

2.3 Electromagnetic transition rates and Weisskopf estimates

For an electromagnetic decay from an initial state with angular momentum I_i and parity π_i to a final state with angular momentum I_f and parity π_f , the following

selection rules are defined:

$$|I_i - I_f| < I < I_i + I_f, \quad (2.20)$$

where I is the angular momentum carried by the emitted photon, and

$$\Delta\pi = \pi_i\pi_f = \begin{cases} (-1)^I & \text{for electric transitions} \\ (-1)^{I+1} & \text{for magnetic transitions} \end{cases} \quad (2.21)$$

where $\Delta\pi$ is the parity of the radiation and determines the type of the transition.

The full transition probability (in units transitions per second) for a γ -decay of a specific type σ (electric or magnetic) and angular momentum I in terms of multipole matrix elements is given by:

$$P_{fi}(\sigma, Im) = \frac{8\pi(I+1)}{\hbar I[(2I+1)!!]^2} \left(\frac{E_\gamma[\text{MeV}]}{\hbar c} \right)^{2I+1} |\langle I_f m_f | \hat{M}(\sigma, Im) | I_i m_i \rangle|^2, \quad (2.22)$$

where m , m_f , m_i are the third projections of the angular momentum I , I_f , I_i respectively and $\hat{M}(\sigma, Im)$ is the multipole matrix element [49]. This equation can be expressed in terms of the reduced transition probability $B(\sigma, I, I_i \rightarrow I_f)$ via the reduced matrix elements $|\langle f || \hat{M}(\lambda, I) || i \rangle|^2$ as:

$$P_{fi}(\sigma, I) = \frac{8\pi(I+1)}{\hbar I[(2I+1)!!]^2} \left(\frac{E_\gamma[\text{MeV}]}{\hbar c} \right)^{2I+1} B(\sigma, I, I_i \rightarrow I_f), \quad (2.23)$$

where

$$B(\sigma, I, I_i \rightarrow I_f) = \frac{1}{(2I_i+1)} |\langle f || \hat{M}(\lambda, I) || i \rangle|^2. \quad (2.24)$$

Taking into account that the full transition probability is essentially the decay constant (λ) and using the relation

$$T_{1/2}[\text{s}] = \frac{\ln 2}{\lambda} = \frac{\ln 2}{P_{fi}(\sigma, I)}, \quad (2.25)$$

where $T_{1/2}$ is the half-life of the initial state, the reduced transition probability can be written as:

$$B(\sigma, I, I_i \rightarrow I_f) = \frac{\hbar I[(2I+1)!!]^2}{8\pi(I+1)} \left(\frac{\hbar c}{E_\gamma[\text{MeV}]} \right)^{2I+1} \frac{\ln 2}{T_{1/2}[\text{s}]}. \quad (2.26)$$

Here $B(\sigma, I, I_i \rightarrow I_f)$ is expressed in units of $e^2 f m^{2I}$ for electric and in $\mu_N^2 f m^{2I-2}$ for magnetic transitions, where e is the electron charge and μ_N is the nuclear magneton.

Internal conversion (IC) is a type of electromagnetic process that competes

with γ decay. It is a process during which the excited nucleus interacts with the atomic electrons, causing one of them to be emitted, if the excitation energy is larger than the electron binding energy. The probability for internal conversion is inversely proportional to the energy difference between the initial and final states, i.e. the process is favoured for low energy transitions. The competition between IC and γ decay can be quantified via the internal conversion coefficient (α), which is defined as the ratio between emitted conversion electrons and photons: $\alpha = \text{number of IC}/\text{number of } \gamma \text{ decays}$. In order to take the effect of internal conversion into account, the reduced transition probability is modified to

$$B(\sigma, I, I_i \rightarrow I_f) = \frac{\hbar I[(2I+1)!!]^2}{8\pi(I+1)} \left(\frac{\hbar c}{E_\gamma[\text{MeV}]} \right)^{2I+1} \frac{\ln 2}{T_{1/2}[\text{s}] (1+\alpha)}. \quad (2.27)$$

Another factor that should be taken into account is the branching ratio. Branching ratio is a measure of the probability of a nuclear state to take a certain decay mode instead of all other possible modes. It can be defined in terms of decay rates (λ) as the ratio between the decay rate for the specific decay mode and the total decay rate for all decay modes from the initial state: $BR = \lambda_i/\lambda_{total}$. Then the reduced transition probability is:

$$B(\sigma, I, I_i \rightarrow I_f) = \frac{\hbar I[(2I+1)!!]^2}{8\pi(I+1)} \left(\frac{\hbar c}{E_\gamma[\text{MeV}]} \right)^{2I+1} \frac{\ln 2}{T_{1/2}[\text{s}] (1+\alpha)(1+BR)}. \quad (2.28)$$

According to Eq.2.26 and Eq.2.27 the reduced transition probability is strongly dependent on the transition energy. In order to remove this dependence the Weisskopf estimate is used [49]. The Weisskopf estimate by definition assumes a single (valence) proton configuration and is therefore a one-body operator. The estimates for electric and magnetic transitions are given by:

$$B_W(EI) = \frac{1}{4\pi} \left(\frac{3}{3+I} \right)^2 1.2^{2I} A^{2I/3} [e^2 fm^{2I}] \quad (2.29)$$

$$B_W(MI) = \frac{10}{4\pi} \left(\frac{3}{3+I} \right)^2 1.2^{2I-2} A^{(2I-2)/3} [\mu_N^2 fm^{2I-2}], \quad (2.30)$$

where $R = 1.2A^{1/3}$ fm denotes the nuclear radius. Experimentally obtained reduced transition probabilities are converted to Weisskopf units using the following relation

$$B(\sigma I) [W.u.] = \frac{B_{exp}(\sigma I)}{B_W(\sigma I)}, \quad (2.31)$$

where both the experimental reduced transition probability, $B_{exp}(\sigma I)$, and the Weisskopf estimate, $B_W(\sigma I)$, are given in the same units ($e^2 fm^{2I}$ or $\mu_N^2 fm^{2I-2}$). The reduced transition probabilities expressed in Weisskopf units give a rough

estimate of the number of nucleons contributing to a given electromagnetic transition, i.e. they can serve as a measure of collectivity (and nuclear shapes).

2.4 Interaction of photons with matter

Due to their lack of charge, photons interact very differently with matter compared to charged particles. The three dominant mechanisms are photoelectric effect, Compton scattering and pair production.

In photoelectric absorption the incident γ ray is fully absorbed by an atomic electron. Part of the deposited energy is used to overcome the binding energy of the electron and the rest becomes kinetic energy of the emitted photoelectron. The photoelectric effect is a dominant process for photon energies below a few hundred keV.

For γ rays at higher energies up to a few MeV, Compton scattering becomes the dominant process. A γ -ray scatters off an electron, transferring some of its energy to it. The energy of the scattered photon E'_γ can be evaluated using the formula

$$E'_\gamma = \frac{E_\gamma}{1 + \frac{E_\gamma}{m_e c^2} (1 - \cos \theta)}, \quad (2.32)$$

where E_γ is the energy of the incident photon, m_e is the mass of the electron at rest and θ is the scattering angle [48]. As can be seen from the equation, the amount of energy that is transferred to the electron depends on the scattering angle.

The last interaction mechanism is pair production. During this process the incident γ -ray completely disappears, creating an electron-positron pair. This process is possible for γ -rays with energies higher than 1.022 MeV, which corresponds to double the rest mass energy of an electron. The excess energy becomes kinetic energy for the created pair. The positron then annihilates with an electron, producing two 511 keV γ -rays. This process becomes dominant for photon energies above 5 MeV.

2.5 The fast timing technique

The fast-timing method is a technique that enables the direct measurement of nuclear lifetimes in the range from a few microseconds to a few picoseconds. It is based on measuring time differences between events associated with the feeding and decaying transitions of a specific nuclear state. As a (relatively) recent development of the fast-timing methodology, the Generalized Centriod

Difference (GCD) method [52, 53] was designed for analysis of experimental data obtained from fast-timing arrays consisting of a large number of detectors.

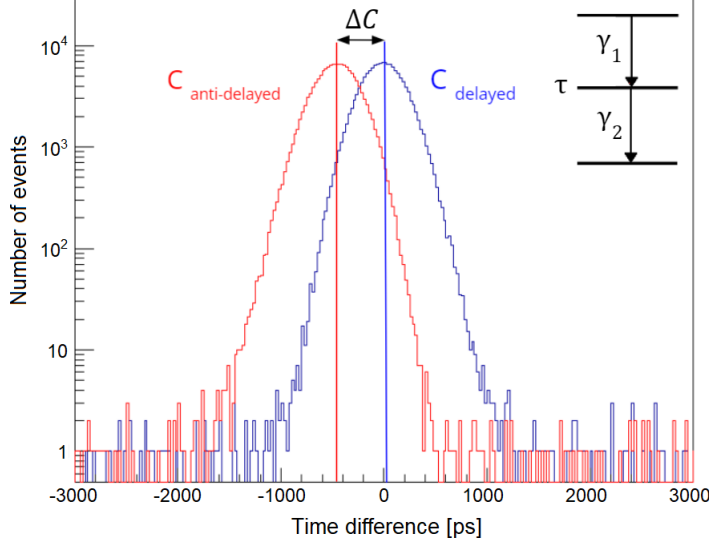


Figure 2.4: Delayed and anti-delayed time distributions for a specific feeder-decay cascade associated with a nuclear state of interest

In order to explain the GCD concept, let us first consider a standard γ - γ fast-timing setup consisting of two detectors, which are denoted as "start" and "stop". Feeding and decaying γ -rays associated with a specific nuclear state are registered in the detector pair. If the feeding γ -ray (γ_1) is detected by the "start" detector and the decaying γ -ray (γ_2) by the "stop" detector, the so called *delayed* time-difference distribution is obtained. If the opposite is true, γ_2 in "start" detector and γ_1 in "stop" detector, the *anti-delayed* time-difference distribution is attained (see Fig. 2.4). The difference between the centroids of the two time distributions (delayed and anti-delayed) is given by:

$$\Delta C(\Delta E_\gamma) = C_{delayed} - C_{anti-delayed} = PRD(\Delta E_\gamma) + 2\tau, \quad (2.33)$$

where $\Delta E_\gamma = E_{feeder} - E_{decay}$ is the energy difference between the feeding and decaying γ -rays and τ is the lifetime of the state of interest. The Prompt Response Difference (PRD) describes the zero-time response of the detector system and serves as a single correction parameter according to Eq.(2.33). The PRD is energy dependent and can be calibrated via a PRD curve using standard calibration sources. This procedure will be explained in detail in Chapter 4.

It is important to note that the centroid difference is mirror symmetric with respect to start-stop inversion. For a prompt cascade this means an inversion of

the feeder-decay cascade and thus

$$\begin{aligned}\Delta C(\Delta E_\gamma)_{decay} &= -\Delta C(-\Delta E_\gamma)_{feeder} \\ PRD(\Delta E_\gamma)_{decay} &= -PRD(-\Delta E_\gamma)_{feeder}.\end{aligned}\tag{2.34}$$

This mirror symmetry allows us to determine the PRD for any energy combination using:

$$PRD = PRD(E_{feeder}) - PRD(E_{decay}).\tag{2.35}$$

For fast-timing arrays consisting of more than two (almost equal) detectors the centroid differences for each unique detector-detector pair need to be determined. This procedure can be simplified by superimposing the time distributions of all unique two-detector combinations. In order to achieve a good time resolution for this final superimposed time distribution, there is a need for precise time alignment of each fast-timing detector pair. This time calibration procedure is explained in detail in Chapter 4.

Nuclear lifetimes, which are long enough to be observed as a slope in the delayed time distribution, are measured by performing a fit of an exponential decay curve

$$f(x) = e^{-t/\tau},\tag{2.36}$$

to the experimental data.

Chapter 3

Experimental setup

DEcay SPECtroscoPy (DESPEC) as a concept aims at studying the nuclear structure of exotic nuclei using radioactive beams delivered by the FRagment Separator (FRS) [54] located at GSI Helmholtzzentrum für Schwerionenforschung GmbH, Germany [55] and in the future Superconducting FRagment Separator (SuperFRS) [56] at the upcoming Facility for Antiproton and Ion Research (FAIR) [57]. For the purpose of this thesis, the focus will be on an experiment performed as part of FAIR Phase-0, using the FRS and the DESPEC setup at the GSI accelerator facility.

The nuclei of interest were produced by the fragmentation of ^{124}Xe primary beam impinging on a 4 g/cm^2 ^9Be target [44], after being accelerated to 982 MeV/u in the UNiversal Linear ACcelerator (UNILAC) [58] and the SIS18 synchrotron [59] accelerator complex. The reaction products were separated and identified on an event-by-event basis in the FRagment Separator (FRS) [54], using the $B\rho\text{-}\Delta E\text{-}B\rho$ and ToF- $B\rho\text{-}\Delta E$ methods [60, 61]. Finally the ions reach the DEcay SPECtroscoPy setup (DESPEC) [62] where they are implanted in an active stopper [63]. Subsequent γ -rays following the decay of populated isomeric states in the nuclei of interest are detected by High-Purity Germanium (HPGe) [64, 65] and $\text{LaBr}_3(\text{Ce})$ detectors [66].

In this chapter detailed information about the experimental setup and methods is provided. In particular the GSI accelerator facility (UNILAC and SIS18), exotic beam production and projectile fragmentation, separation and identification of ions in the FRS, the γ -ray or decay spectroscopy setup.

3.1 The GSI accelerator facility

A schematic of GSI accelerator facility is shown in Fig. 3.1. The GSI ion sources can produce beams of elements anywhere from hydrogen to uranium. After being extracted from the source the primary beam is being bunched and stripped off

electrons, before being injected into the main part of the UNILAC [58]. There the ions are accelerated (up to 11.4 MeV/u) and transported towards the SIS18 synchrotron [59], where they are further boosted and can reach energies from up to 1 GeV (for uranium) to 4.5 GeV (for protons). This primary beam is then extracted and delivered to different experimental areas.

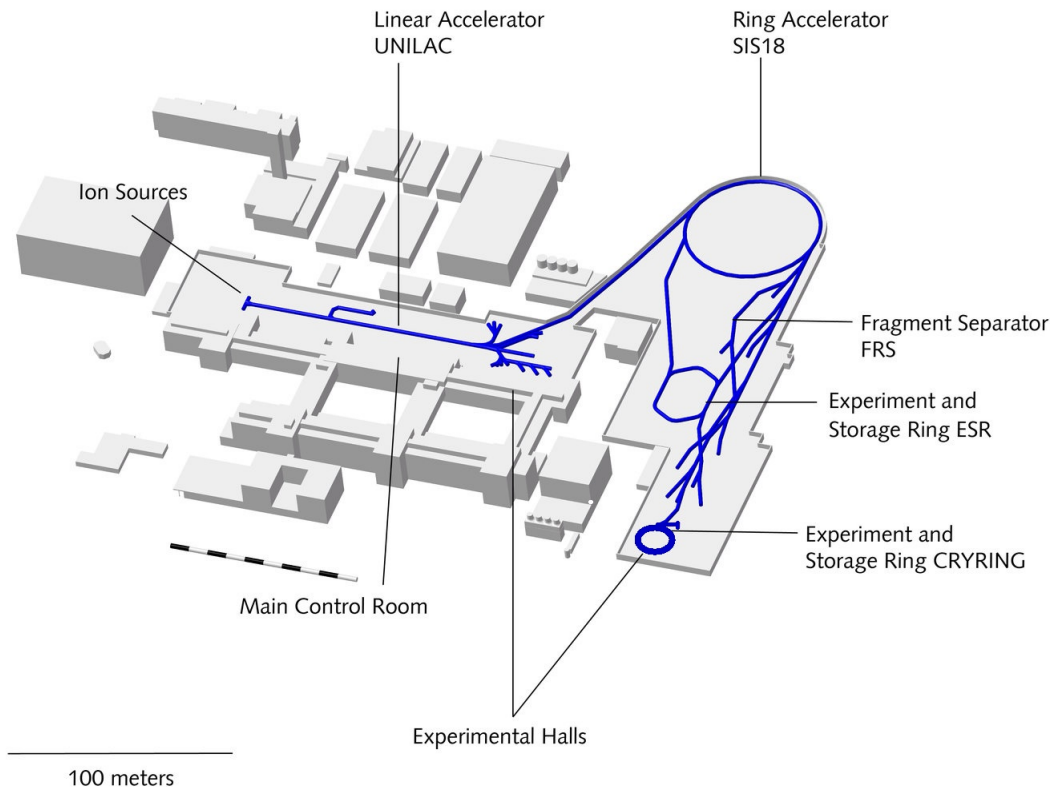


Figure 3.1: Schematic of the GSI accelerator facility [67]. Primary beam ions, extracted from an ion source, are injected into the UNILAC and later delivered to the SIS18 synchrotron. The primary beam, accelerated in the UNILAC and the SIS18, is then sent towards the FRS, where secondary beams can be created using different targets and reaction mechanisms. Experiments are performed using primary and secondary beams, delivered to the experimental halls.

3.2 Production of exotic nuclear beams

The primary beam coming from the SIS18 is focused on a target at the entrance of the FRS. As mentioned in the beginning of this chapter, the ^{94}Pd and other ions of interest were populated by the fragmentation of the ^{124}Xe primary beam on a ^9Be target. Reasonable description of fragmentation reactions is achieved by the abrasion-ablation model [68], which looks at this type of interaction as a two step process. The first step, called abrasion, consists of projectiles im-

pinging on the target removing a number of nucleons. Two types of particles are defined: "participants" located in the geometrical overlap, where projectile and target nucleons interact, and "spectators", which are outside of the overlap zone and continue moving (almost unaffected) with their initial velocity. The "participants" form a highly-excited prefragment, which during the second stage of the fragmentation process (ablation) de-excites via evaporation of particles (protons, neutrons, light particles) and/or γ -ray emission, ultimately forming the final fragment.

3.3 The fragment separator

The secondary fragment beam contains not only one isotope, but a complex mixture of numerous nuclei. The different ion species are spatially separated in the FRS via the $B\rho\text{-}\Delta E\text{-}B\rho$ method [60, 61] using a system of magnets. In addition the projectile fragments are identified on an event-by-event basis in the second part of the FRS. The separation and identification methods will be explained in detail in the next sections. A schematic of the FRS is shown in Fig. 3.2.

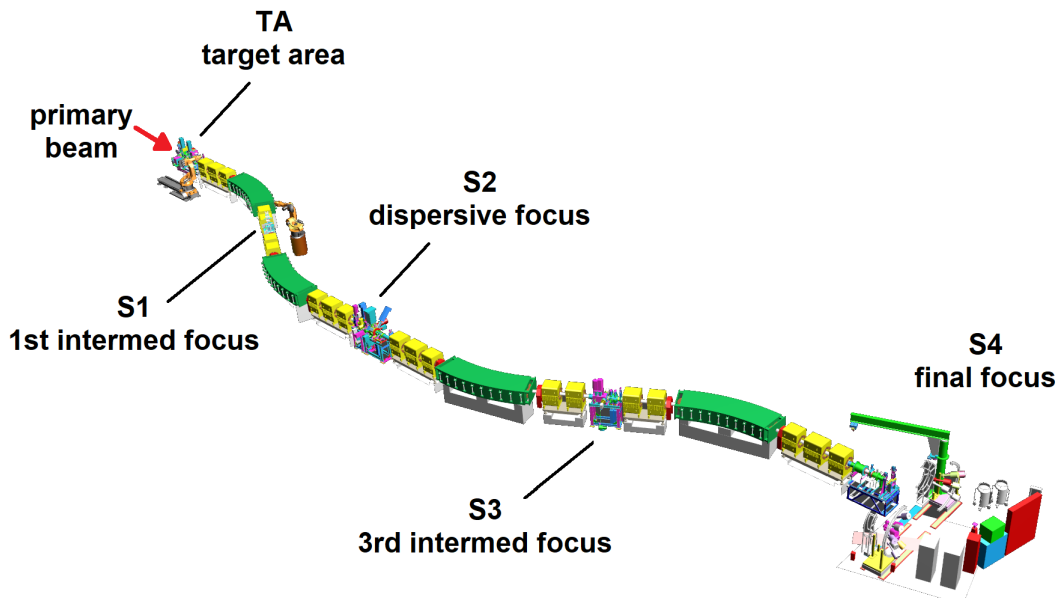


Figure 3.2: Schematic of the FRS fragment separator [69]. The dipole (green) and multipole (yellow) magnets used for separation and focusing of the beam. The different focal planes are marked and labeled - S1, S2, S3, S4.

3.3.1 The $B\rho$ - ΔE - $B\rho$ separation method

A charged particle with charge q and velocity \vec{v} going through a homogeneous magnetic field \vec{B} is affected by a Lorentz force:

$$\vec{F}_L = q(\vec{v} \times \vec{B}). \quad (3.1)$$

In the FRS dipoles the magnetic field is perpendicular to the velocity of the ion causing it to follow a circular path and creating a centrifugal force:

$$F_r = \frac{mv^2}{\rho}, \quad (3.2)$$

where m is the mass of the ion and ρ is the radius of the circular trajectory. Combining Eq.3.1 and Eq.3.2 gives us the magnetic rigidity:

$$B\rho = \frac{mv}{q}. \quad (3.3)$$

The momentum of a relativistic ion can be expressed as $p = \gamma\beta mc$, where $\gamma = \sqrt{1/(1 - \beta^2)}$, $\beta = v/c$ and c is the speed of light. By substituting $m = Au$ and assuming a fully stripped ion ($q = Ze$), the following equation is obtained

$$\frac{A}{Z} = \frac{eB\rho}{\gamma\beta uc}. \quad (3.4)$$

Here A is the mass number, u is the atomic mass unit and e is the electron charge. This gives us a connection between the magnetic rigidity $B\rho$ and the mass-to-charge ratio (A/Z) of a charged particle passing through the dipole magnets.

The $B\rho$ - ΔE - $B\rho$ method is a three step process. In the first stage the fragments are being filtered based on their A/Z ratio in the first two FRS dipoles. Ions with the different magnetic rigidity $B\rho$ reach an aluminum wedge-shaped degrader, placed in the S2 dispersive focal plane, at different positions.

The next step occurs when the fragments interact with the degrader in S2. The energy loss (ΔE) in the material serves as an additional selection criterion for separation. In the current experiment the FRS was operated in the standard achromatic mode [70]. The thickness of the wedge-degrader can be varied creating a gradient. The thickness and angle are chosen such that all ions of a specific species have the same velocity after passing through the degrader. In this so called energy-loss spectrometer mode, nuclei of the same species arrive at the final focal plane (S4) at the same position.

In the third and final step another $B\rho$ selection by the last two dipole magnets is performed.

3.3.2 The ToF- $B\rho$ - ΔE identification method

In order to properly track and identify the different ion species various detectors are placed and used in the fragment separator - Multi-Wire Proportional Counters (MWPC), MUlti Sampling Ionization Chambers (MUSIC), Scintillators.

Multi-Wire Proportional Counters (MWPC) [71] placed along the beam line serve to determine the position of ions passing through the FRS. MWPC detectors consist of two cathodes (X, Y) orthogonal to each other, an anode (A) oriented at 45° with respect to X and Y, and two planar electrodes (T, G) (see Fig. 3.3). The detector is operated with a CO_2/Argon gas mixture.

A charged particle passing through a MWPC interacts with the gas atoms in the gap between the two electrode grids U_G and U_T , creating an avalanche of electrons. The emitted electrons are then accelerated towards the cathode plane and a secondary electron avalanche is generated close to the anode grid U_A . This leads to positive charge being induced in the nearby X and Y wire(s). A schematic of this process is shown in Fig. 3.3.

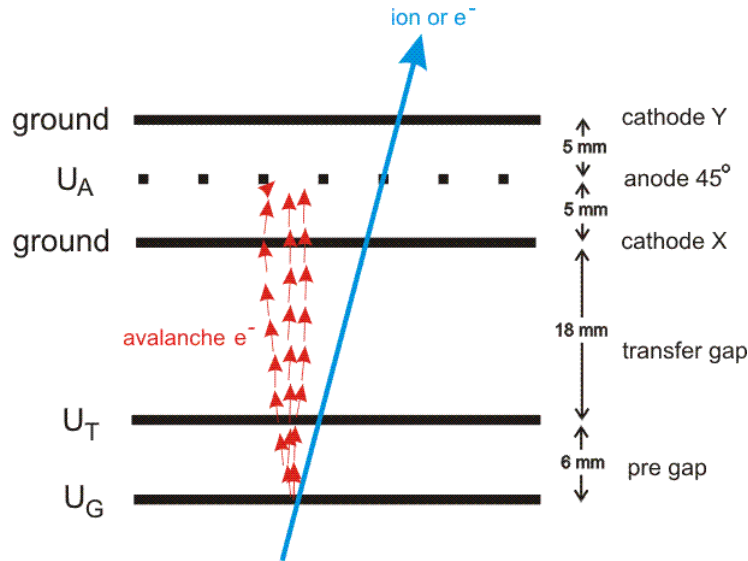


Figure 3.3: Layout of a Multi-Wire Proportional Counter [72]. Charged particle passing through the detector ionizes the gas atoms along its trajectory. The produced ions and electrons are accelerated towards the cathodes, where a secondary electron avalanche near the anode is generated inducing positive charge in the X and Y cathodes.

The X and Y signals are readout via a delay line, where each wire corresponds to a different delay time. The delayed signals are fed to a time-to-digital converter (TDC) with channels - left (X_L), right (X_R), up (Y_U) and down (Y_D). The position of interaction between the beam and the detector can be determined

using the time differences:

$$X[mm] = x_{factor}(X_L - X_R) + x_{offset}, \quad (3.5)$$

$$Y[mm] = y_{factor}(Y_U - Y_D) + y_{offset}, \quad (3.6)$$

where x_{factor} , y_{factor} depend on the delay lines and the TPC, and x_{offset} , y_{offset} are the offsets in mm. An event is considered as "good" if at least one of the sums $X_L + X_R$ or $Y_U + Y_D$ is a constant.

MULTI Sampling Ionization Chamber (MUSIC) [73] located at the final focal plane of the FRS (S4) and are used to determine the atomic number Z of the fragments via an energy-loss measurement. The chamber is operated with pure CF_4 gas at room temperature and contains eight independent anode strips, a cathode and a Frisch grid [74] (see Fig. 3.4).

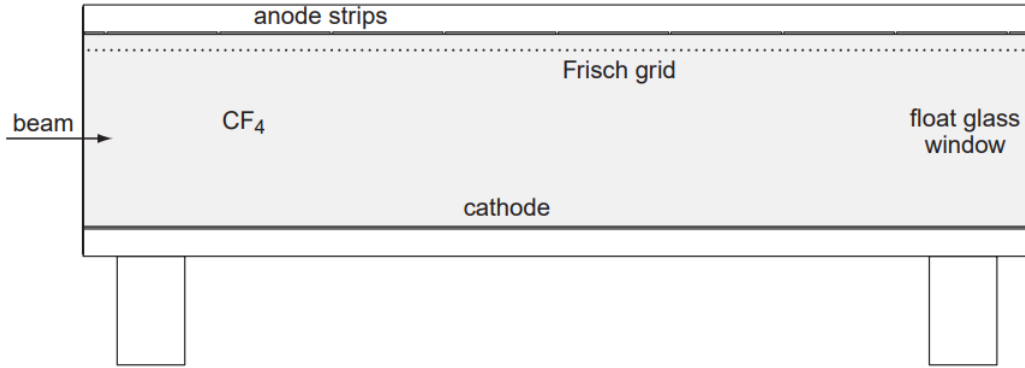


Figure 3.4: Layout of a Multi Sampling Ionization Chamber [73]. An ion passing through the detector generates an electron cloud along its trajectory. The electrons drift towards and are collected by the anode. The number of created electrons is proportional to the energy loss of the ions passing through the detector.

An electron cloud is generated when an ion passes through the detector. The electrons then drift towards the anode, where they are collected by charge sensitive preamplifiers and shapers. The amplitude of the signal is proportional to the energy loss of the ions. By using the Bethe-Bloch formula, which connects the stopping power $-dE/dx$ and the atomic number Z of ions, the following relation is obtained

$$-\frac{dE}{dx} = Z^2 f(\beta), \quad (3.7)$$

where $f(\beta)$ is a function of the ion's velocity.

Plastic Scintillators [75] in the intermediate and final focal planes of the FRS

provide position, energy loss (ΔE) and time-of-flight (ToF) information. An incident ion interacts with scintillation material through fluorescence. Fluorescence is the process of emission of (visible) light, when a material is brought to an excited state. In order to convert the light into an electrical pulse the scintillation material was coupled to two Photo-Multiplier Tubes (PMT) placed on both sides of the plastic.

The obtained ToF information is then used to determine the velocity β of the different fragments. Experimentally the ToF can be obtained using time signals from the Sc21 (in S2) and Sc41 (in S4) scintillators:

$$ToF = T_{Sc41} - T_{Sc21} \quad (3.8)$$

and it is a function of the distance d_0 between the scintillators and the velocity v of the ions

$$ToF = \frac{d_0}{v}. \quad (3.9)$$

However, only ions, which arrive at the final focal plane of the FRS can be studied, therefore the signal from Sc21 is delayed (dT) so that $T_{Sc41} < T_{Sc21} + dT$. The measured time-of-flight ToF_m is:

$$ToF_m = T_{Sc21} + dT - T_{Sc41}. \quad (3.10)$$

The connection between the real and the measured ToF can be deduced from Eq.3.8 and 3.10:

$$ToF = dT - ToF_m. \quad (3.11)$$

By substituting this in Eq.3.9 and using the relation $\beta = v/c$, the velocity of the fragments can be attained [76]

$$\beta = \frac{d_0/c}{dT - ToF_m}. \quad (3.12)$$

Different ion event-by-event arrive at different positions at the S2 and S4 focal planes, thus resulting in different path lengths through the FRS as compared to the central trajectory. In order to properly determine the ToF and in turn the velocity of each species of interest these differences in paths are taken into account and a path correction is applied.

Particle identification

The particle identification is done via the ToF- $B\rho$ - ΔE method. How to obtain the ToF and the ΔE was already explained above. The magnetic rigidity, $B\rho$,

can be determined using the equation:

$$B\rho = B\rho_0 \left(1 - \frac{X_4 - M_{S2-S4}X_2}{D_{S2-S4}} \right), \quad (3.13)$$

where $B\rho_0$ is the magnetic rigidity of a centered beam. X_2 and X_4 are the horizontal positions measured by the MWPC or the scintillator detectors in S2 and S4 respectively. D_{S2-S4} and M_{S2-S4} are the dispersion and the magnification between the middle and final focal planes of the fragment separator. Using the last relation Eq.3.4 can be expanded to:

$$\frac{A}{Z} = \frac{eB\rho}{\gamma\beta uc} = \frac{eB\rho_0}{\gamma\beta uc} \left(1 - \frac{X_4 - M_{S2-S4}X_2}{D_{S2-S4}} \right). \quad (3.14)$$

According to this equation, the A/Z of a fragment is calculated using the $B\rho_0$ of a centered beam, the velocity β of the particle and their positions X_2 and X_4 in the corresponding focal plane. The final particle identification is shown in Chapter 4 Fig. 4.8.

3.4 The decay spectroscopy setup

The fragments of interest, selected and transported by the FRS ultimately arrive at its final focal (S4), where the DESPEC setup [62] is located. Some of the ions are procured in an isomeric or a β decaying state. If the lifetime of this state is long enough to survive the ~ 300 ns flight through the FRS, the fragments are implanted precisely in the AIDA active stopper. Electrons and photons associated with the decays of these stopped ions will then be registered in the β Plastic in case of *beta* decay and in the FAst TIMing Array (FATIMA) [66] and the DEGAS/GALILEO High-Purity Germanium (HPGe) array [64, 65] in case of γ decay. A schematic and a picture of the DESPEC setup are shown in Fig. 3.5.

3.4.1 The implantation setup

The Advanced Implantation Detector Array (AIDA) [63] is a detector array based on Double Sided Silicon Strip Detectors (DSSSD). It is used as an active stopper, providing interaction position, timing and energy information about implanted ions and their subsequent decay radiation. In the currently-discussed experiment, AIDA consisted of three layers of 1 mm thick DSSSDs each with a size of 8 x 8 cm² and 128 x 128 strips (16384 pixels).

A single DSSSD is made up of a core of n-doped silicon plate and p⁺- and n⁺-doped strips with aluminum contacts on opposite sides of the detector. The

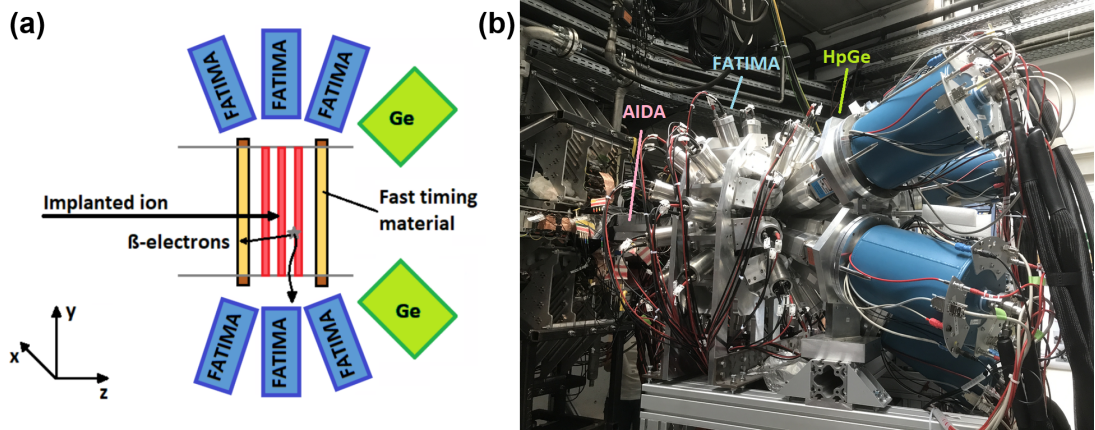


Figure 3.5: (a) Schematic of the DESPEC setup. Ions from the FRS are stopped in the implantation setup, which consists of AIDA (red) and β Plastic (yellow). γ -rays following the decay of the implanted ions are registered in the $\text{LaBr}_3(\text{Ce})$ detectors of the FATIMA array (blue) and in the DEGAS/GALILEO HPGe detectors (green). (b) Picture of the experimental setup, consisting of an array of six DEGAS/GALILEO clusters (with blue dewars), three rings of FATIMA detector array (in gray aluminum housing) and AIDA + β Plastic implantation setup (a section of the AIDA snout can be seen to the left of the FATIMA array).

two sets of strips are orthogonal to each other. Voltage is applied to the detector so that the depletion zone extends throughout the entire silicon plate. When a charged particle passes through (or stops in) the DSSSD, it generates electron-hole pairs, which then drift towards and are collected by the n^+ - and p^+ -doped strips. The charge distribution between different strips provides the X and Y position, while the amplitude of the signal is proportional to the energy loss of the incident ion. A schematic of a DSSSD detector is shown in Fig. 3.6.

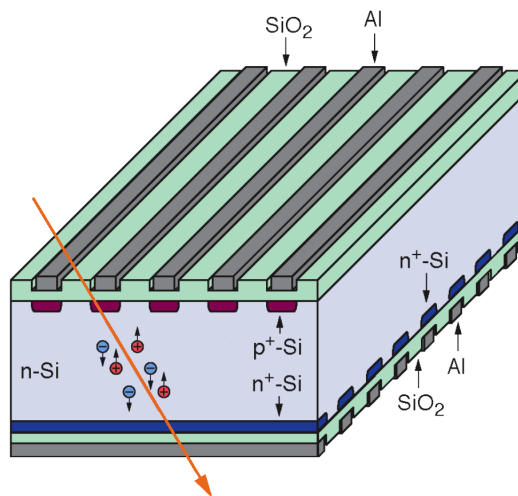


Figure 3.6: Schematic of a DSSSD. A charged particle passing through the detector induces electron-hole pairs which drift towards the X and Y strips on both sides of the detector, where they are collected.

Implanted ions deposit energies of up to a few GeV in the DSSSD. The emitted particles (β and α particles, protons, neutrons and γ rays) following the de-excitation of the stopped ions have energies in the order of tens of keV to a few MeV. For the purpose of providing a good energy resolution over this broad energy range (from a few keV to a few GeV), an Application Specific Integrated Circuit (ASIC) was developed [77]. It is able to freely switch between two modes of operation measuring particle energies in two energy ranges (high gain and low gain). More details on the ASIC can be found in [77].

A good position resolution is needed in order to correlate the implant and decay events registered in a DSSSD. The high degree of pixelation allows for a precise measurement of the implantation position as well as the position of subsequent decays. In addition, by measuring the time between the implantation and the de-excitation, the half-life of the radioactive decay can be determined. AIDA has a time resolution in the order of 2 microseconds.

β Plastic is a plastic scintillation detector. The DESPEC setup employs two such detectors: one in front and one behind the AIDA stack (Fig. 3.7). Each β Plastic detector is made up of 3 mm thick plastic material coupled to $3 \times 3 \text{ mm}^2$ silicon photomultipliers (SiPMs) along the four sides. The final size of $8 \times 8 \text{ cm}^2$ was chosen to match the size of the AIDA DSSSDs. The signals from the SiPMs are fed to TAMEX-based electronics cards developed in GSI by the Experimental Electronics Department [78].

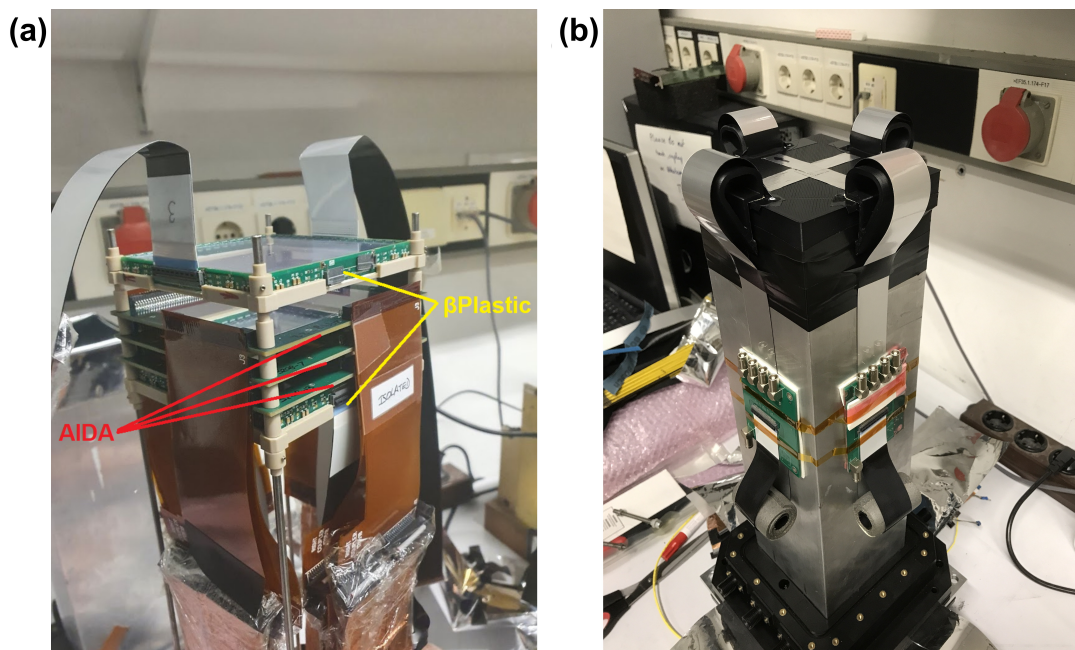


Figure 3.7: (a) Implantation setup, consisting of three AIDA DSSSDs (red) and two β Plastic detectors (yellow) upstream and downstream of the DSSSDs. (b) AIDA 'snout'

The β Plastic detectors exhibit excellent time resolution. Implants in AIDA can be correlated with the β Plastic detectors to achieve fast-timing for short-lived excited nuclear states and β -decay measurements.

All five layers of the implantation setup (three AIDA DSSDs and two β Plastic detectors) are mounted in an aluminum case referred to as the AIDA 'snout' (Fig. 3.7).

3.4.2 The FATIMA detector array

The FASt TIMing Array (FATIMA) [66] is a scintillation detector array, which can be used to determine lifetimes of both long-lived isomeric states as well as short lifetimes in the order of tens of picoseconds. FATIMA consists of 36 $\text{LaBr}_3(\text{Ce})$ crystals, each with a diameter of 1.5" and length of 2". The scintillator crystals are coupled to fast PMTs and are enclosed in 4 mm thick lead casings (Fig. 3.8(a)). The 36 detectors are mounted in 3 rings (12 detectors each) surrounding the implantation setup (Fig. 3.8(b)).

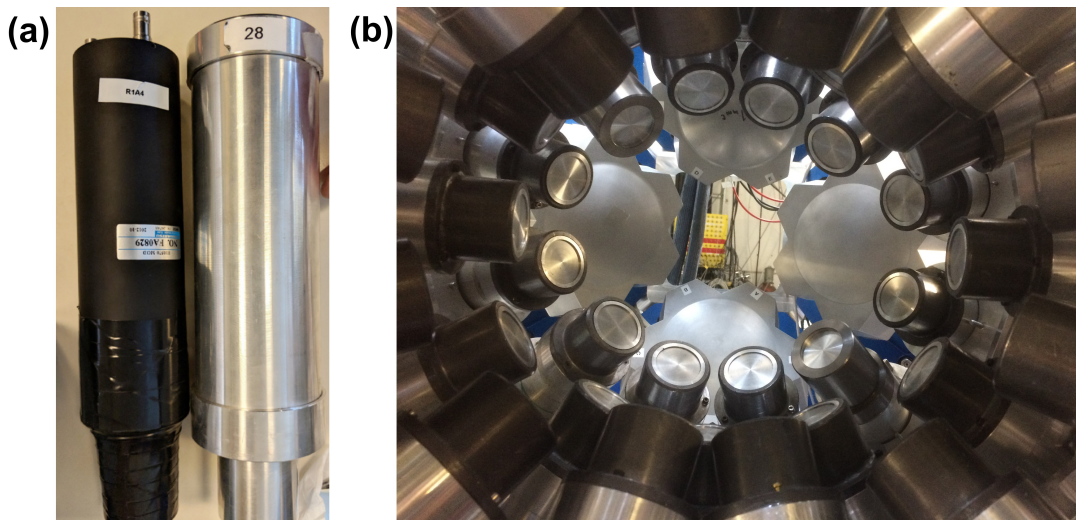


Figure 3.8: (a) FATIMA detector parts [66]. $\text{LaBr}_3(\text{Ce})$ crystal taped to a PMT on the left and the casing on the right. (b) FATIMA array, consisting of 3 rings each holding 12 detectors.

The signals from the detectors were read out via two independent electronics systems VME and TAMEX. For the VME system, the energy was determined by sending the signals to charge-to-digital converters (QDCs), while for the timing the signals were sent to time-to-digital converters (TDCs) through constant fraction discriminators (CFDs). For the 36 $\text{LaBr}_3(\text{Ce})$ detectors, two CFD and two TDC cards were used. The TDCs were synchronized via a 40 MHz common external clock and each TDC has a time resolution of 25 ps (least significant bit). The FATIMA VME data from the experiment was analyzed and the results were

presented in the next chapters. In the context of this thesis the TAMEX data will not be discussed.

Photons associated implants in AIDA are registered by the FATIMA detectors. The obtained energy and timing information is used to measure time differences between γ -rays in a decay cascade. Using analysis techniques such as the GCD method, which was described in Chapter 2 Section 2.5, allows for measuring lifetimes as low as ~ 10 ps.

3.4.3 The high-purity germanium cluster detectors

In this experiment six GALILEO triple HPGe cluster detectors [64, 65] were employed at forward angles of the DESPEC setup (Fig. 3.5(b) and Fig. 3.9(b)). Each cluster detector comprises three encapsulated HPGe crystals in a common cryostat (Fig. 3.9(a)), with a total of 18 crystals. The signals from the detectors are readout via FEBEX digitizers developed at GSI. The energy is determined by applying a trapezoidal filter algorithm, while the timing information is obtained from an on-board CFD.

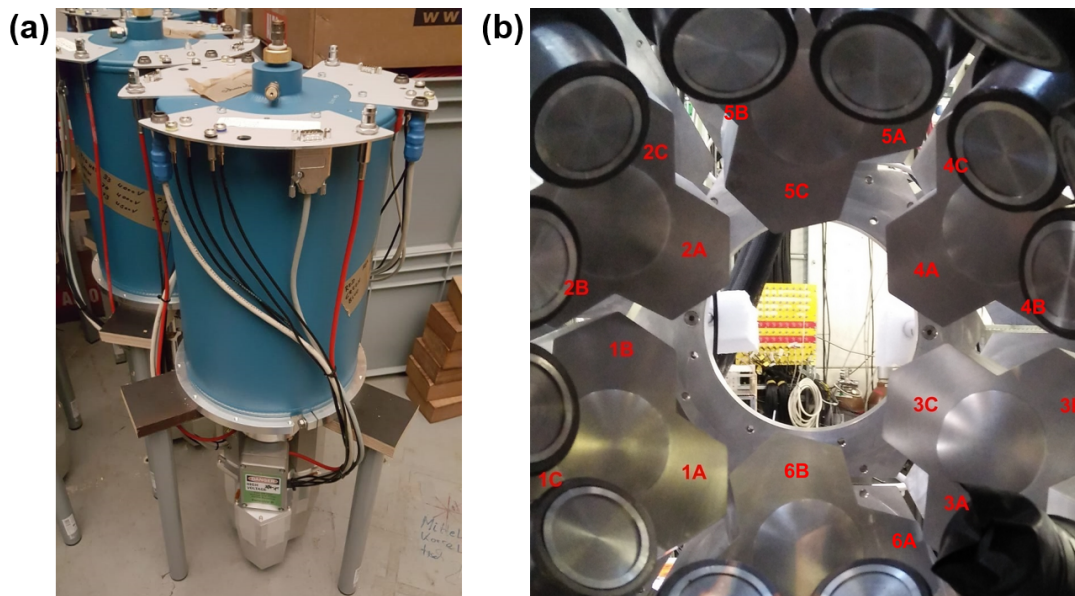


Figure 3.9: (a) Picture of a GALILEO triple cluster HPGe detector with its Dewar. (b) Picture of the six GALILEO detectors used during the experiment.

The GALILEO array was operated in add-back mode. This mode allows for the reconstruction of the energy of a γ ray, that was scattered to neighboring crystals of a single HPGe detector via Compton scattering. When a photon interacts with one of the Ge crystals it deposits a fraction of its energy and can then scatter to an adjacent crystal, where it will either scatter again or be fully absorbed. Assuming the latter, and by adding the two signals, the initial energy of the γ ray can be recovered.

The main focus of the DESPEC setup in this experiment was fast-timing measurements of nuclear lifetimes. In this context, the HPGe detectors with their superior energy resolution (compared to the LaBr₃(Ce) detectors) allow for precise identification of the detected γ rays.

3.4.4 Data acquisition

The DESPEC setup consists of independent subsystems, each using its own Multi Branch System (MBS) [79] data acquisition (DAQ) developed at GSI. AIDA is operated in triggerless mode, wherein the signals are processed by a specially-designed ASIC circuit. Data collected by the different DAQs were timestamped using the White Rabbit (WR) timing system [80] and then merged via a time sorter, which arranges data items into chronological order. The WR timing is driven by a 125 MHz clock with an absolute start time (epoch) at midnight 1st of January 1970. It is delivered to all subsystems and depending on the receiving board it can have a timestamp precision of down to ~ 1 ns.

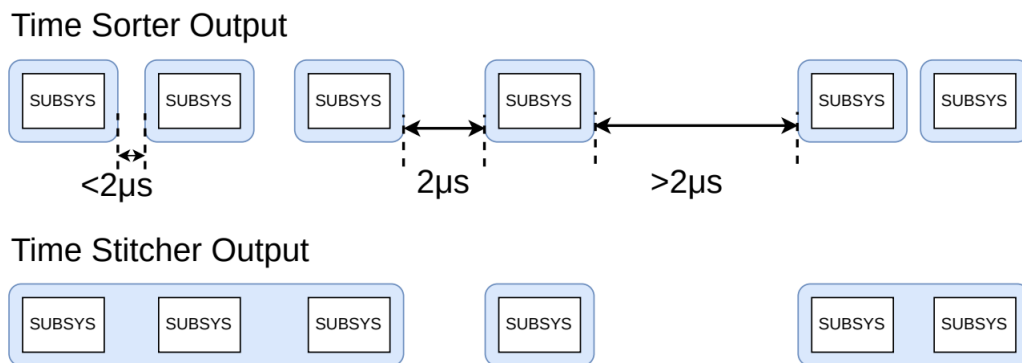


Figure 3.10: Schematic of the time-stitching process [62]. In case of a gap of less than $2\mu\text{s}$ between events from different subsystems, these are combined into a single event.

An additional step is needed in order to correlate events via the WR global time. This process is called time-stitching and is achieved via a general purpose unpacker called unpack and check every single bit (ucesb) [81]. ucesb is used to build events in such a way that the data from different subsystems can be accessed at once with the Go4 offline data-analysis framework. It combines events from different subsystems in a single event by grouping them together until a $2\mu\text{s}$ gap is observed (Fig. 3.10). An additional requirement is that only one FRS event is observed per combined event. If a second event, associated with the FRS is observed before a $2\mu\text{s}$ gap occurs, the current event is "closed" and a new one is started.

Chapter 4

Data Analysis

A number of calibrations and corrections need to be implemented and applied to the raw data obtained directly from the different detectors, in order to acquire meaningful information. In addition, the collected data contains γ rays not only from the nuclei of interest, but also from a number of different sources: side products of the fragmentation reaction, background sources, self-activity (for example from the $\text{LaBr}_3(\text{Ce})$ material), etc. To clean the observed spectra a variety of conditions are applied to the data such as Z and A/Q gates to select the ions of interest, prompt flash cut to reduce the level of the background, background subtraction depending on the method of analysis. In this chapter all required calibrations, corrections and cleaning conditions will be discussed in detail.

4.1 Calibration of the FRS detectors

In order to calibrate the MUSIC detectors and the ToF, data is collected for different FRS settings using primary beams with well defined energies and by placing well calibrated targets and degraders in the path of the beam. For the currently discussed experiment three FRS settings using primary ^{124}Xe beam were utilized:

- Setting 1: Minimum matter primary beam setting, where the beam is centered and only the necessary detectors for beam tracking are left in the way of the beam.
- Setting 2: A well calibrated wedge-shaped disk degrader is inserted onto the beamline at the S2 focal plane.
- Setting 3: In addition to the disk degrader, a 4 mg/cm^2 Be target is inserted at the Target Area (TA).

Additional calibrations such as Z and A/Q drift corrections, angle correction, etc. using the in-beam data are necessary to guarantee the optimal condition of

the data. After all detectors are calibrated the particle identification plot (PID) can be obtained and further used to select the ions of interest.

4.1.1 Time-of-flight calibration

As discussed in Chapter 3, the ToF can be determined from the difference in time between Sc21 and Sc41, taking the delay of the Sc21 signal into account (Eq.3.10). The velocity β of an ion, expressed as a function of the distance between the scintillators and the measured Time-of-Flight ToF_m , is given by Eq.3.12. In terms of the ToF_m this equation can be rewritten as

$$\beta ToF_m = dT\beta - \frac{d_0}{c} = a\beta + b. \quad (4.1)$$

Using the obtained data from the different FRS settings, βToF_m can be plotted as a function of the velocity of the primary beam as shown in Fig. 4.1. Then the calibration coefficients a and b are determined by fitting the data points with a linear function.

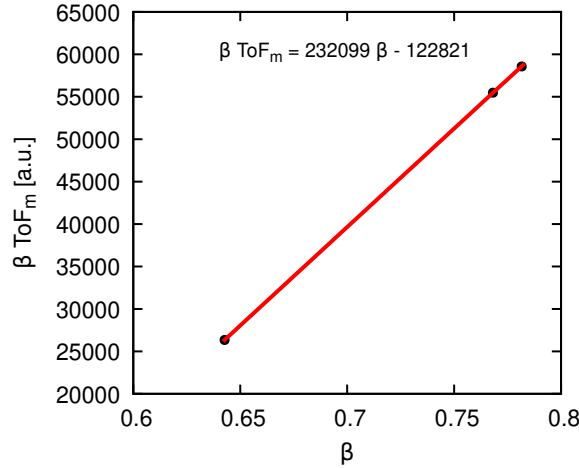


Figure 4.1: Time-of-flight calibration

4.1.2 MUSIC velocity calibration

It was explained in Chapter 3 that the energy loss of an ion in matter is a function of the atomic number Z and its velocity β (see Eq.3.7). Thus the response of the MUSIC detectors needs to be calibrated for different values of the velocity. The energy loss ΔE in the two MUSIC detectors (MUSIC41 and MUSIC42) is plotted as a function of the velocity of the primary beam β as shown in Fig. 4.2. The data is then fitted with a second order polynomial function according to the equation

$$\Delta E = a\beta^2 + b\beta + c \quad (4.2)$$

and the calibration parameters a , b and c are extracted.

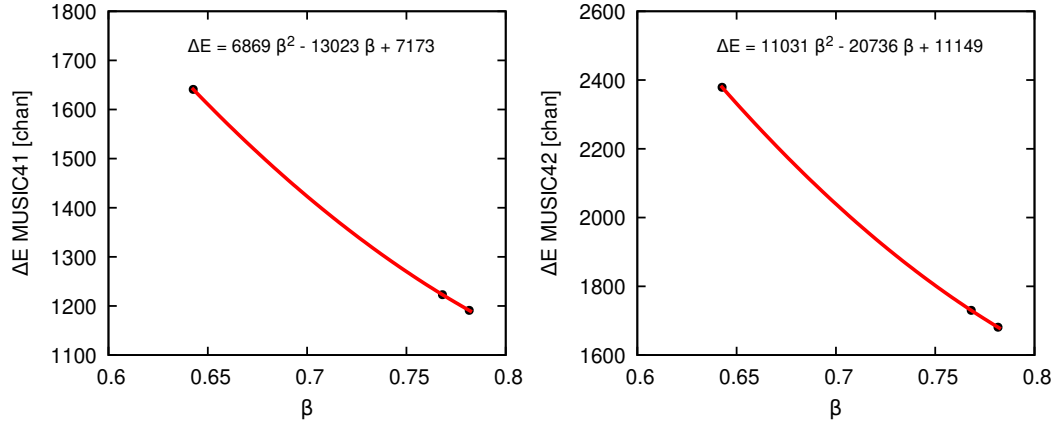


Figure 4.2: Velocity calibration of the MUSIC detectors

The energy loss of fragments in the MUSIC detectors can be related to the energy loss of the primary beam through the following equation

$$-\frac{dE_f}{dx} = -\frac{Z_f^2}{Z_p^2} \frac{dE_p}{dx}(\beta), \quad (4.3)$$

where the indexes f and p denote fragments and/or primary beam respectively. Then the atomic number of a fragment Z_f can be obtained from the relation

$$Z_f = Z_p \sqrt{\frac{\Delta E_f}{\Delta E}} = Z_p \sqrt{\frac{\Delta E_f}{a\beta^2 + b\beta + c}} \quad (4.4)$$

after the calibration of the MUSIC detectors (see Fig. 4.3).

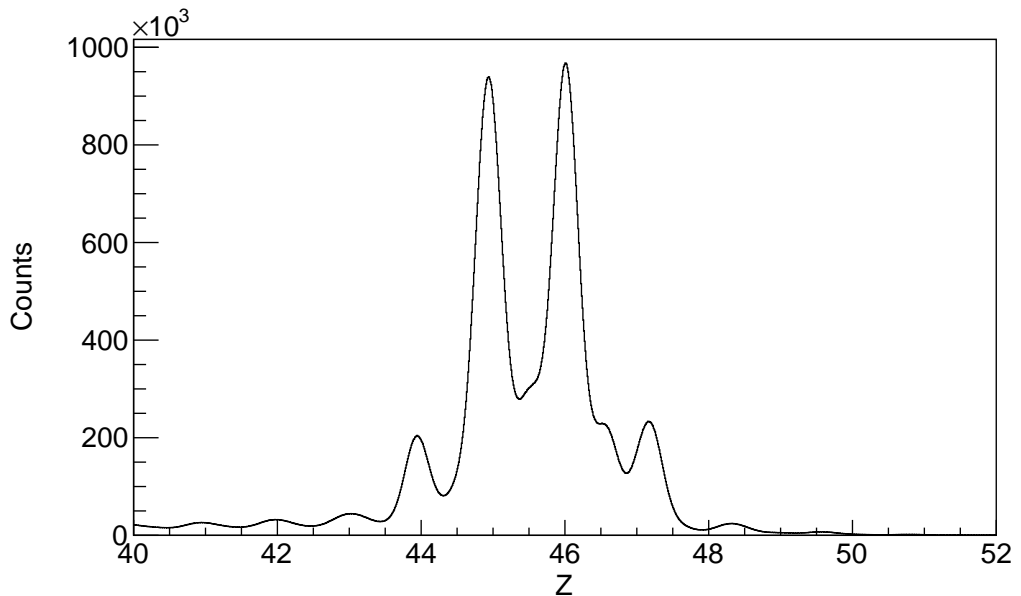


Figure 4.3: Z values obtained after the calibration of the MUSIC detectors

4.1.3 Z calibration and drift correction

How to determine the atomic number Z of fragments passing through the FRS was already discussed in detail in Chapter 3. The atomic number Z is to be used to construct the particle identification plot, which is later utilized to select ions of interest for further analysis. However, when looking into the in-beam data, it was discovered that Z was not stable throughout the experiment (see Fig. 4.4(a)). This so-called drift can be a result of many factors (temperature changes of the

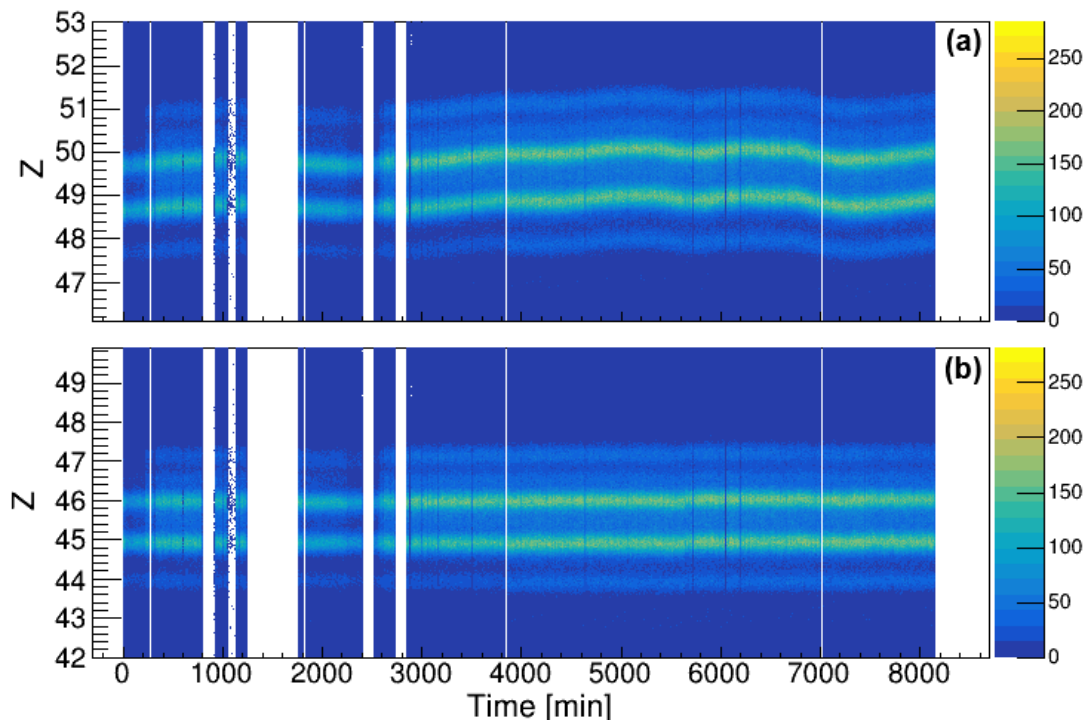


Figure 4.4: Atomic number (Z) versus time of the experiment (a) before and (b) after the drift correction

electronics and/or detectors, effects of the charge collection, etc) and needs to be corrected in order to be able to set gates and conditions as cleanly as possible.

As mentioned, Fig. 4.4(a) shows how the raw (uncorrected) atomic number Z changes during the experiment. The white strips in the histogram represent times, when there was no data collection due to starting a new file, problems with the beam, accelerator or DAQ, etc. The drift was corrected by taking projections on the Y axis (Z) in a certain time ranges of 60 minutes and aligning them to a reference spectrum via an offset (see Fig. 4.5). In the current analysis the reference was the projection in the time range 0-60 minutes. After applying the drift correction the atomic number was calibrated. Fig. 4.4(b) shows final atomic number Z in time plot. The final corrected and calibrated atomic number was used to produce the PID plot.

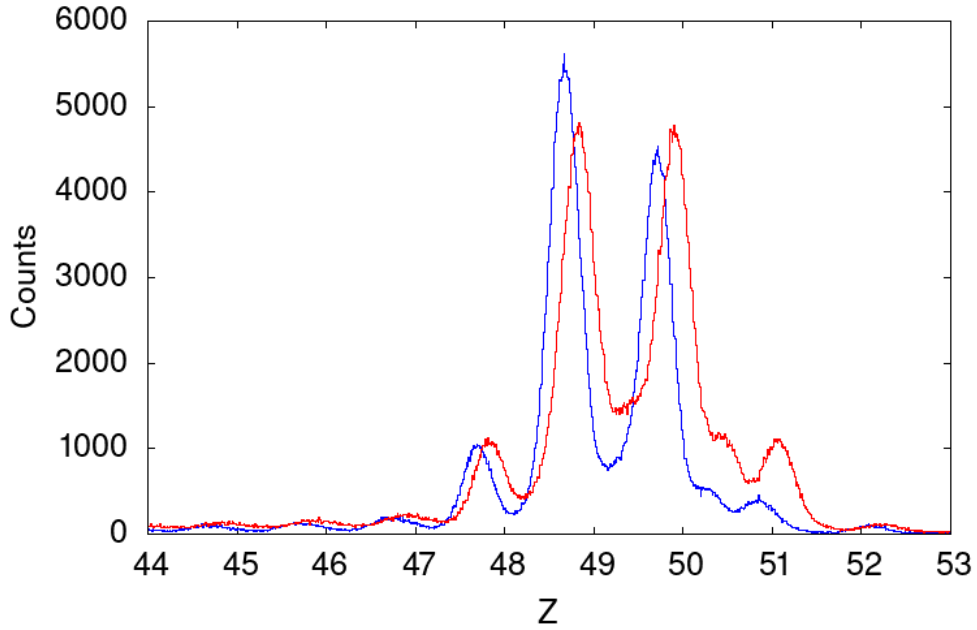


Figure 4.5: Projections on the Z axis for time range 0-60 minutes in blue serving as a reference and the range 6000-6060 minutes in red, which is aligned to the reference via an offset.

4.1.4 Angle correction

Using the different FRS tracking detectors, the arrival positions and angles of different fragments at the different focal planes can be determined. Fig. 4.6(a)

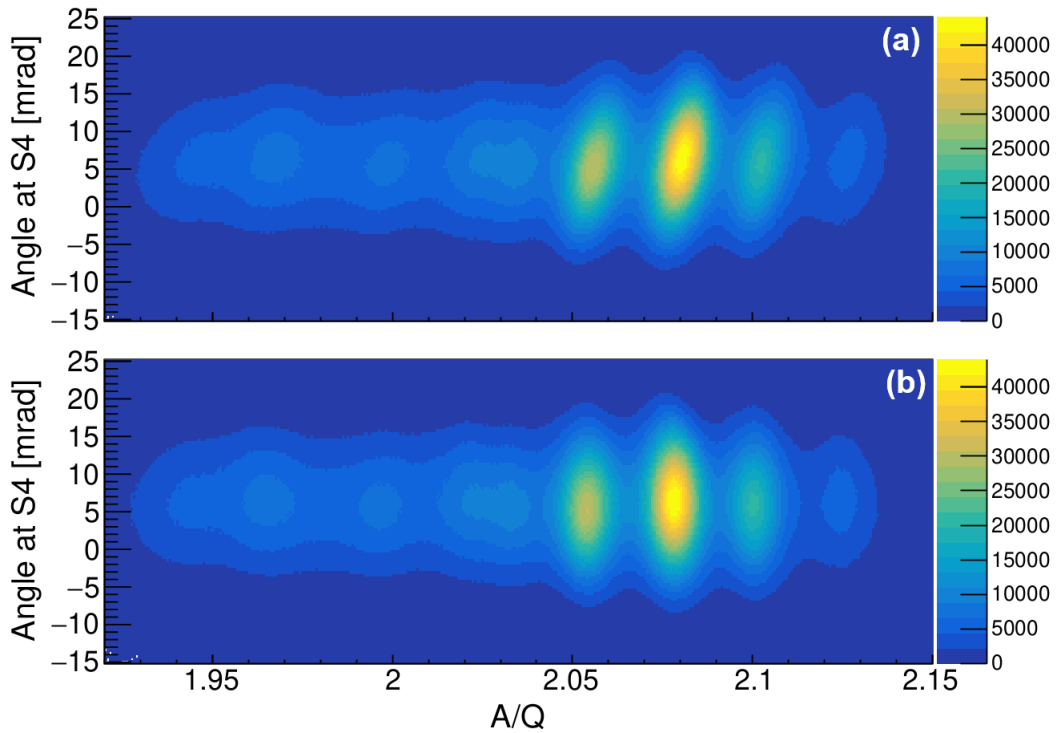


Figure 4.6: Angle in S4 versus mass over charge ratio A/Q (a) before and (b) after the angle correction.

shows the angles at which different isotopes, characterized and identified by their A/Q ratio, arrive at the S4 focal plane. A slight tilt (shift) can be seen for each elliptical region. In order to achieve good separation between different isotopes in the final PID, these shifts need to be corrected.

The procedure for correcting the shifts is similar to the drift correction performed for the atomic number Z . Projections on the X axis (A/Q) over a range of angles are produced and aligned to a reference spectrum via an offset (see Fig. 4.7). In the current analysis the reference was the projection in the range of 0-1 mrad. Finally, Fig. 4.6(b) shows the angle corrected spectrum.

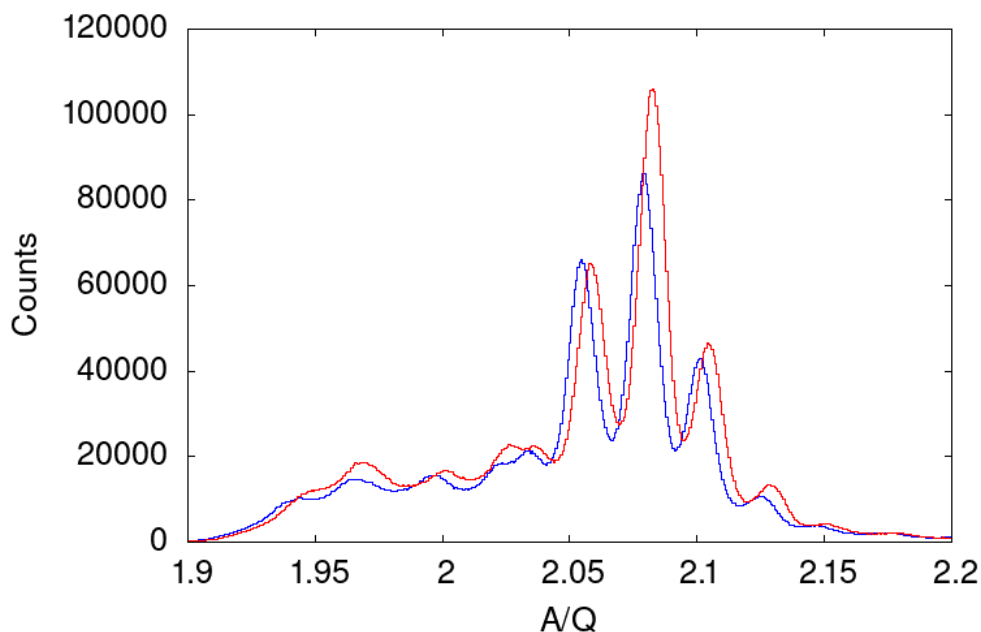


Figure 4.7: Projections on the A/Q axis for angle range 0-1 mrad in blue serving as a reference and the range 10-11 mrad in red, which is aligned to the reference via an offset.

4.1.5 Selecting the ions of interest

Using the calibrated FRS data the particle identification plot (PID) was produced. Fig. 4.8 shows the PID, where different nuclei are identified based on their atomic number Z and mass over charge ratio A/Q . Well known γ -ray transitions from ^{96}Pd were identified and correlated to a specific region in the PID, in order to make sure that the identification is correct. Using this the position of ^{94}Pd and other isotopes can be easily deduced. By gating on different regions in the PID plot, i.e. different ions, γ rays associated with the de-excitation of isomeric states in these nuclei can be selected, excluding contributions from other fragments.

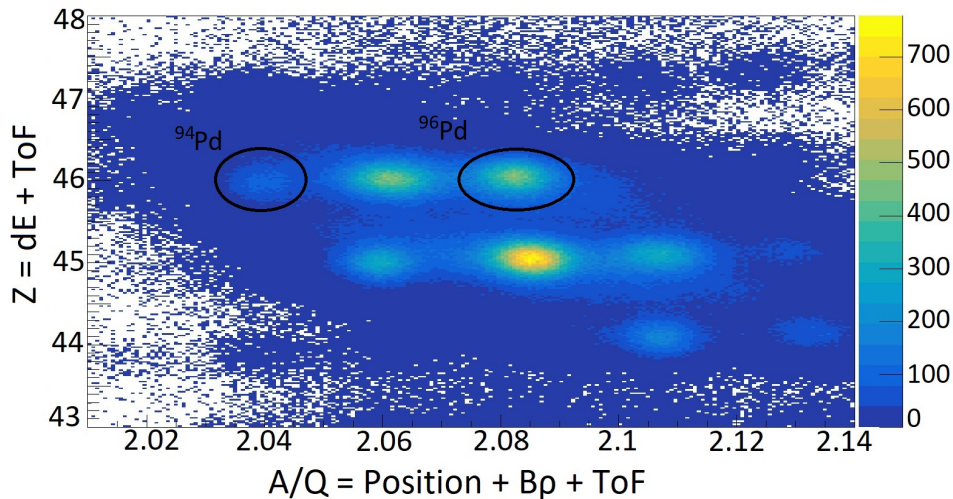


Figure 4.8: Particle identification plot

4.2 Calibration of the FATIMA detectors

The individual $\text{LaBr}_3(\text{Ce})$ detectors were calibrated using standard calibration sources. Aside from the basic calibrations such as energy and time, a number of additional corrections were needed in order to clean the data as much as possible. In the following subsections all applied calibrations and corrections will be discussed in detail.

4.2.1 Energy calibration

Three procedures were employed in order to calibrate all individual $\text{LaBr}_3(\text{Ce})$ detectors and finally obtain a superimposed energy calibrated γ spectrum, unaffected by "outside" factors (such as temperature fluctuations). Standard ^{152}Eu calibration source was used to obtain data for gain-matching and energy calibration, while the experimental data was used for an additional in-beam correction.

Gain-matching

Temperature fluctuations due to the day-night cycle affect the detectors and the electronics. This can cause changes to the gains of the detectors (see Fig. 4.9(a)), which if left uncorrected broadens the γ peaks observed in the energy spectrum, worsening the energy resolution.

A python based script developed by M. Rudigier was used to correct the gain drift of the raw not calibrated energy of each individual detector, before any energy calibration was implemented. The code uses an iterative minimization procedure, which evaluates how close a histogram is to a reference histogram by calculating a bin-wise square difference. With each iteration a linear correction

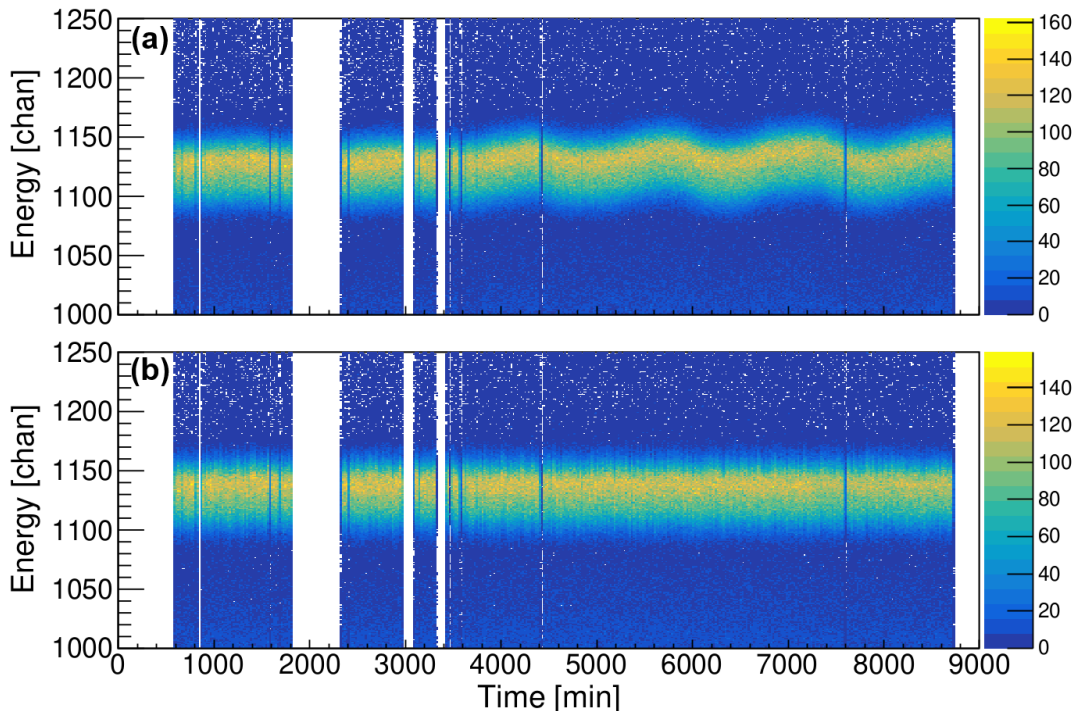


Figure 4.9: Raw energy vs time of the experiment before (a) and after (b) gain matching for a particular γ peak

is applied to the first histogram until the best gain-matching factor with the smallest square difference is found.

To achieve this the script uses an energy vs time of the experiment 2D histogram for a single detector as input (as shown in Fig. 4.9(a)) and requires one to choose a time window (dT) and the starting time of the reference window (T) in minutes. The reference 1D histogram is usually chosen to be in the beginning or in the end of the experiment, depending on when the source data needed for energy calibration was collected. This spectrum is produced by gating in the time range from T to $T+dT$ and projecting the data on the Y-axis (energy axis). The additional spectra that will be compared and aligned to the reference are created using the same procedure covering the full range of the experiment time in increments of dT .

As output the code creates a text file, containing the gain-matching factors for each time range. The entire gain-matching process is then repeated for the rest of the detectors.

For this experiment the detectors were gain-matched to last 20 minutes of the data. The 20 minute window was chosen as the minimum amount of time with sufficient statistics in the raw energy spectrum. Fig. 4.9(b) shows the gain-matched spectrum for one of the $\text{LaBr}_3(\text{Ce})$ detectors.

Energy calibration

To calibrate the gain-matched data a standard ^{152}Eu calibration source was used, covering the range from 121 keV to 1408 keV. The data was taken after the end of the experiment. A cubic polynomial function, $E = ax^3 + bx^2 + cx + d$, was used to convert the scale from channels to energy for every individual $\text{LaBr}_3(\text{Ce})$ detector.

In-beam correction

The energy calibration was verified using the in-beam data. Fig. 4.10(a) shows the in-beam energy spectrum for a single detector, where the lines 511 keV, 1460 keV from ^{40}K and the 1468 keV ^{138}La sum peak were identified. As shown in Fig. 4.10(b),(c) even after gain-matching and energy calibration the detectors are not fully aligned. Therefore, an additional linear in-beam correction was

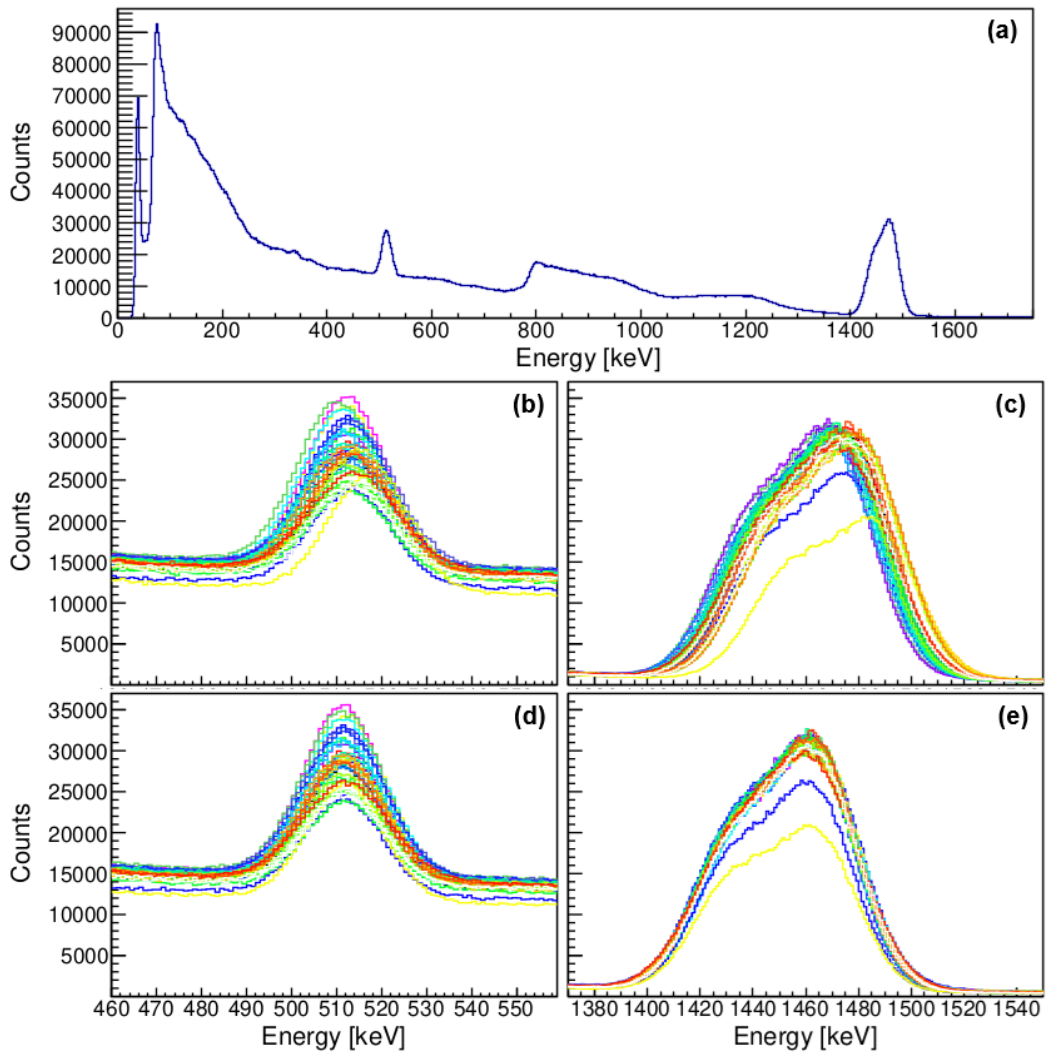


Figure 4.10: (a) Energy calibrated spectrum extracted from the experimental data. In-beam energy calibrated spectra (b,c) before and (d,e) after the in-beam correction for 511 keV, 1460 keV and 1468 keV peaks

implemented using the three known γ -ray lines. Fig. 4.10(d),(e) show the energy spectrum for all detectors after the new correction was applied.

4.2.2 Time calibration

The final goal of the experiment was to measure short nuclear lifetimes. As previously mentioned in Chapter 2 Section 2.5, the analysis procedure can be simplified by superimposing the time distributions of all detector-detector combinations. In this sense, the time alignment and pair correction are two of the most important steps of the data analysis. In addition time-drift correction was carried out using the experimental data.

Let us denote the 36 FATIMA $\text{LaBr}_3(\text{Ce})$ detectors with a number from 0 to 35. In terms of the GCD method, for each pair of detectors a start and a stop detector is chosen. The time difference between two detectors are defined as

$$\begin{aligned} \Delta T &= T_j - T_i \\ i, j &= 0 \text{ to } 35 \quad (i < j), \end{aligned} \tag{4.5}$$

where T_i and T_j are the time signals of the start and stop detectors respectively. The condition $i < j$ is set in order to avoid double counting.

It is important to remember that the centroid difference is mirror symmetric. This allows us to determine the time alignment and pair correction parameters for all detector-detector pairs by using only the delayed time difference distributions. This procedure will be explained in detail in the following sections.

Time alignment

The time alignment was performed by selecting a reference detector and aligning all time differences between the reference and the rest of the detectors to each other. To do this the 344 keV - 778 keV cascade from the ^{152}Eu calibration data was used, where 344 keV is the feeding and 778 keV is the decaying transition of a nuclear state with a lifetime of 46.7(2.5) ps. Detector №0 was chosen as a reference, according to Eq.4.5:

$$\Delta T = T_j - T_0 \quad (j > 0). \tag{4.6}$$

With regard to the GCD method, delayed time difference distributions are obtained for a 344 keV γ -ray detected in the reference detector (start) and a 778 keV registered in another detector (stop). The centroid for each of these detector-detector combinations was determined and served as an offset to the time signal of the stop detectors. All time distributions obtained in this way were aligned to zero (see Fig. 4.11(a),(b)).

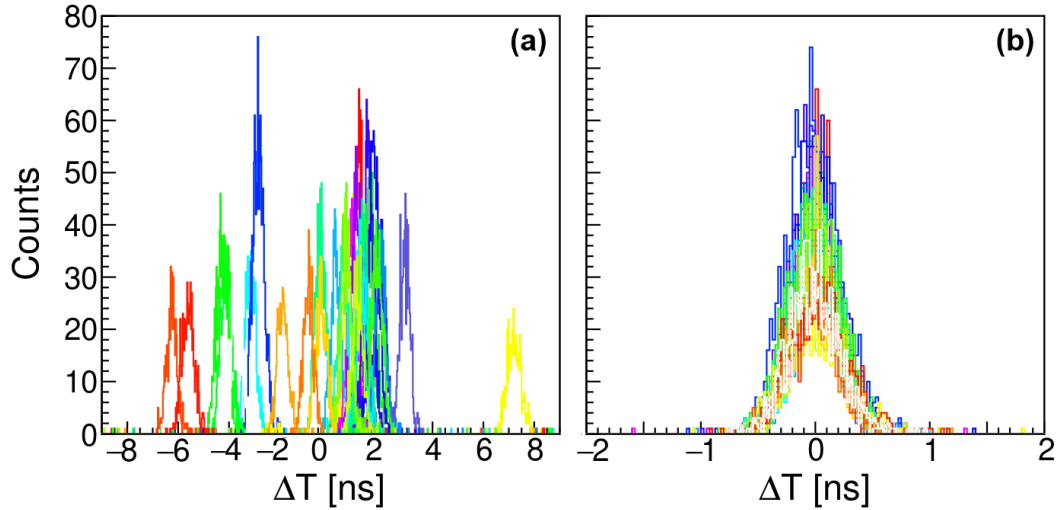


Figure 4.11: Delayed time difference distributions for all detector 0 - detector j , $j=1$ to 35, (a) before and (b) after time alignment.

As explained in Chapter 2 Section 2.5, anti-delayed time difference distributions are obtained by inverting the feeder-decay cascade. This means that a 778 keV photon is registered in the start detector (reference detector 0) and a 344 keV γ -ray is detected in the stop detector(s). Since the anti-delayed time differences follow Eq.4.5 as well, the offset obtained for the delayed time distributions is applicable also here.

Pair correction

The time difference distributions for all detector-detector combinations (excluding detector 0) were crosschecked in order to validate the time alignment. In Fig. 4.12(a) delayed time differences between detector №1 (start) and the rest

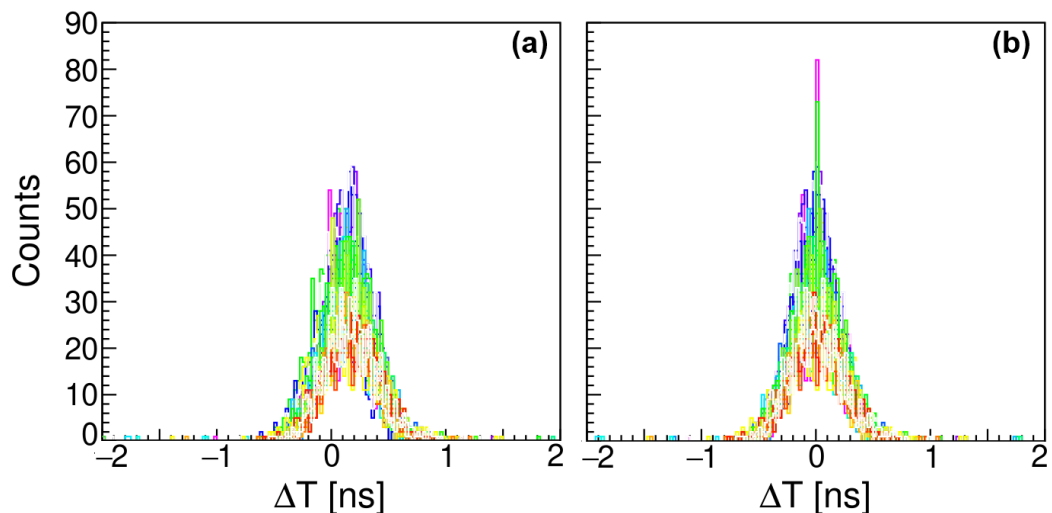


Figure 4.12: Delayed time difference distributions for all detector 1 - detector j , $j=2$ to 35, (a) before and (b) after pair correction.

of the detectors j (stop), $j > 1$, are shown. As can be seen even though aligned the time distributions are not at zero. Since our goal is to superimpose all time distributions, this "shift" has to be corrected for.

Using the same procedure of determining the centroids of the corresponding time difference distributions, an additional offset correction is obtained for each possible detector-detector pair. The pair corrected delayed time distributions for combinations with detector №1 are shown in Fig. 4.12(b).

Time-drift correction

The time alignment and pair correction were verified using 511 keV - 511 keV coincidences from electron-positron annihilation, observed in the in-beam data. The two γ -rays are emitted in opposite directions at an angle of 180° , therefore only coincidences between opposite detector pairs can be observed.

During the validation process it was discovered that combinations of opposite detectors that are read out via different TDCs show a behavior similar to the one seen for the raw energy signals (see Fig. 4.9(a) and Fig. 4.13(a)). This lead us to believe that cause fluctuations is the same, namely the day-night temperature changes. A procedure analogous to gain-matching was performed and the results can be seen in Fig. 4.13(b).

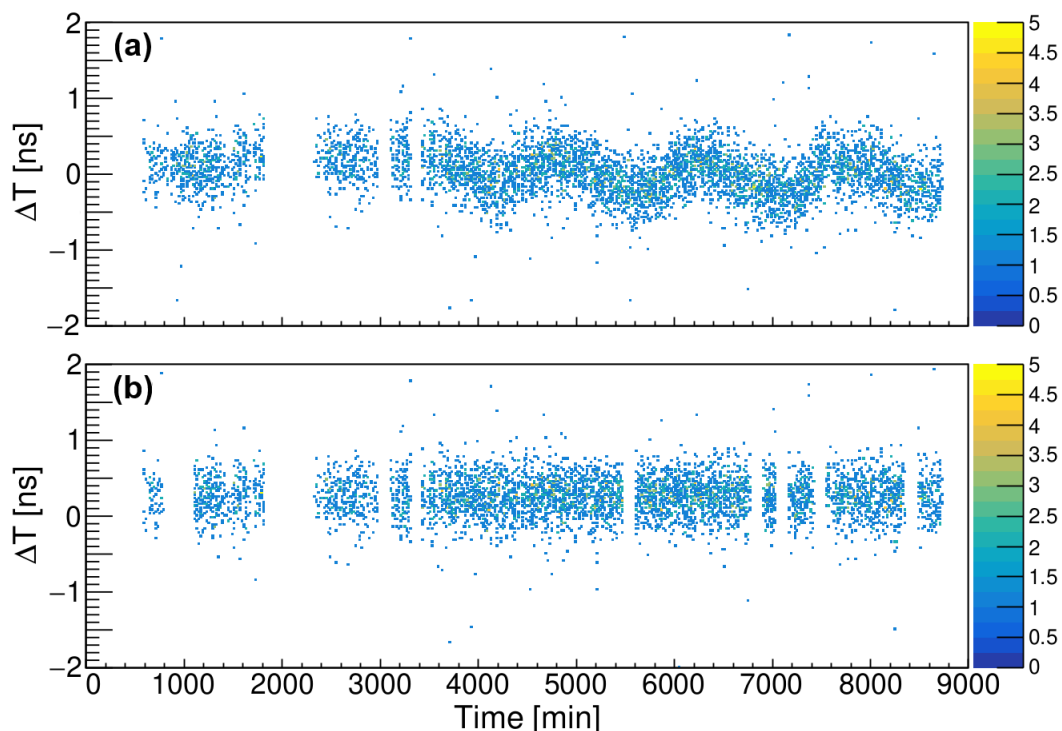


Figure 4.13: Time differences for coincidences between 511- and 511-keV transitions vs time of the experiment (a) before and (b) after the time drift correction.

4.3 Prompt Response Difference and PRD curve

The prompt response difference provides a link between the centroid difference and the lifetime of a nuclear state, as explained in Chapter 2 Section 2.5. In this context, one of the most important steps in the data analysis is the calibration of the PRD. To do this a E_γ - E_γ - ΔT 3D matrix was constructed using the ^{152}Eu calibration data. The X axis represents the energy of the start detector, the Y axis the energy of the stop detector and the Z axis is the time difference between the start and stop detectors (ΔT) according to Eq.4.5.

Various coincidence transitions for nuclear states with known lifetimes (in the order from a few to tens of ps) were used to determine the prompt response difference values, which were adjusted to the 344 keV reference energy. The calibration was done by fitting the data points with a PRD curve according to the function [52]:

$$PRD(E_\gamma) = \frac{a}{\sqrt{E_\gamma + b}} + cE_\gamma + d, \quad (4.7)$$

where a, b, c, d are the parameters for the fit presented in Fig. 4.14(a). Using the fit residuals shown in Fig. 4.14(b), the accuracy of the PRD can be evaluated and a limit for the shortest measurable lifetimes can be established. For the current setup lifetimes below 14 ps could not be determined.

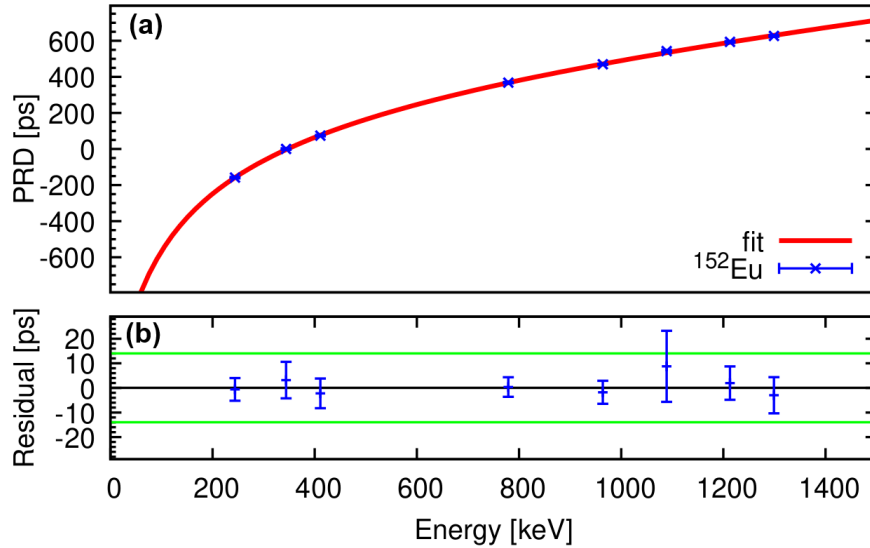


Figure 4.14: (a) PRD calibration points and fit (b) Fit residuals for the PRD

Later in this Chapter the experimentally observed spectra associated with implanted ^{96}Pd and ^{94}Pd ions will be shown and discussed. The observed 106 keV and 94 keV lines de-exciting the $I^\pi = 8^+$ and 14^+ isomers in ^{96}Pd and ^{94}Pd respectively, lead to the need for low energy reference points (below 200 keV) to be included, when determining the PRD curve. Such low energy transition in

^{152}Eu is the 121 keV line. The lifetime of the state fed by 1408 keV and decaying via 121 keV has a lifetime of 2.02(2) ns. However, in addition to the lack of other low energy reference points, the large lifetime and error bar of this state in comparison with the lifetimes of the states used to construct the PRD shown in Fig. 4.14, leads to the rather poor agreement between the PRD curve and the 121 keV reference point. This results in a large residual and in turn to the increase of the shortest measurable lifetime to 110 ps, when including the 121 keV reference point to the PRD (see Fig. 4.15).

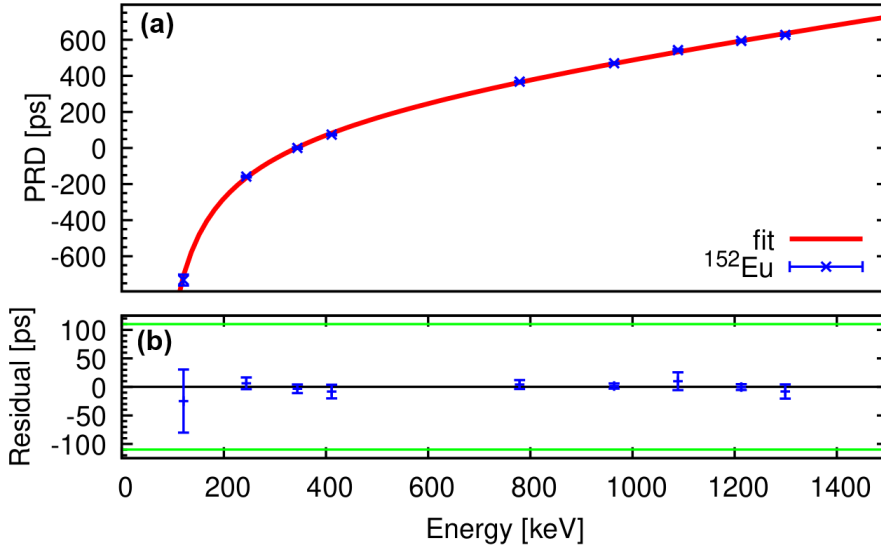


Figure 4.15: (a) PRD calibration points and fit (b) Fit residuals for the PRD

As mentioned previously, the expected lifetimes of the $I^\pi = 6^+$ and 8^+ states in ^{94}Pd , which are the main focus of this thesis, are >10 ps and ~ 1 ns, respectively. The increased shortest measurable lifetime should not affect the measurement of the 8^+ lifetime, however it will make the PRD insensitive to the 6^+ lifetime. For this reason both versions of the PRD were used in determining the lifetimes of the two states of interest.

4.4 Cleaning conditions

The next step in the data analysis before constructing coincidence matrices is to build the energy vs time spectra for γ -rays associated with an implantation in AIDA. In this 2D matrix two structures should be present: prompt flash and the γ -rays following the decay of an isomeric state.

- The prompt flash is associated with the stopping of the beam in matter and indicates the time of implantation. The dominant process is bremsstrahlung due to slowing down of knocked out electrons.

- The observed γ -rays are related to the decays of the intermediate states populated by higher lying isomer. Identical intensity of the γ -rays is an indication that the lifetime of the isomeric state is much longer than the collection window.

However during the analysis a second prompt flash structure was observed, which was 25 ns shifted from the first. Further analysis lead to the assumption that the shifted peak was the result of a bad synchronization between the two TDC electronics modules used to readout the FATIMA signals, leading to a 25 ns "jitter" between them. How these events were recovered and how the influence of the prompt flash was reduced will be explained in detail in the following sections.

Trigger selection

The energy vs time spectrum associated with implanted ^{96}Pd ions, selected in the PID, is shown in Fig. 4.16(a). The time difference ΔT here is the difference between any $\text{LaBr}_3(\text{Ce})$ detector and Scintillator 41, located at the start of the S4 focal plane. The two prompt flash structures mentioned above can be clearly seen in the figure. In order to recover the shifted events the trigger conditions for all implanted ions (not only ^{96}Pd) were investigated.

It was discovered that the first structure consists of events triggered by detectors read out by the first TDC, while in the second the trigger was a detector from the second TDC. Using this knowledge the events were reconstructed and recovered. The spectrum containing the corrected and recovered events for ^{96}Pd can be seen in in Fig. 4.16(b).

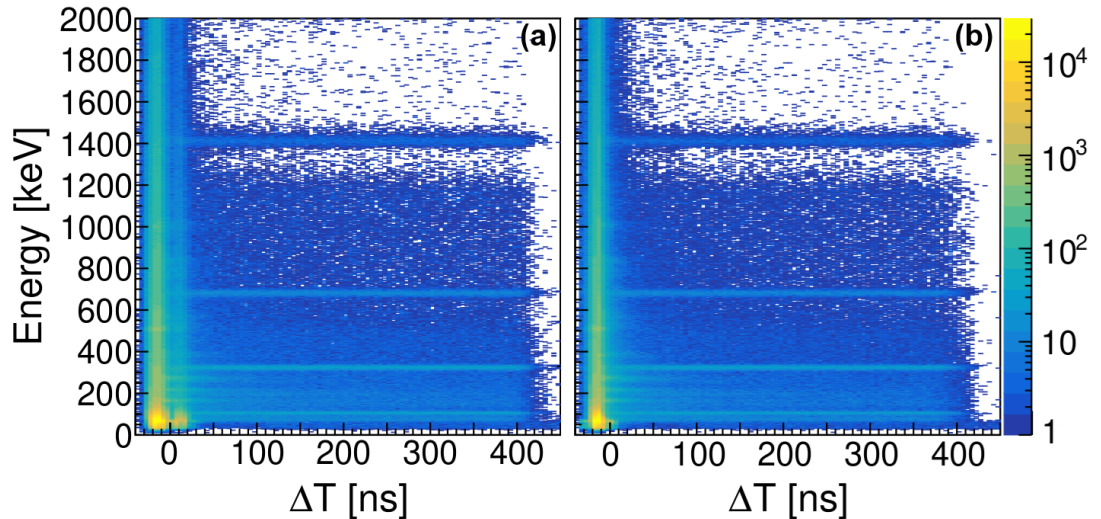


Figure 4.16: Energy vs time spectrum for γ -rays obtained from FATIMA correlated to implantation of ^{96}Pd (a) before and (b) after the procedure for recovering the shifted events.

Prompt flash cut

For a short time after the implantation the prompt flash prevents the acquisition of any reliable information from the detectors. Therefore a "cleaning" condition is applied to the spectrum in order to remove the influence of the prompt flash. These so called prompt flash cuts are shown with red for ^{96}Pd and ^{94}Pd in Fig. 4.17(a),(b) respectively. These conditions reduce the contributions from background events and in this way clean γ -spectra can be obtained.

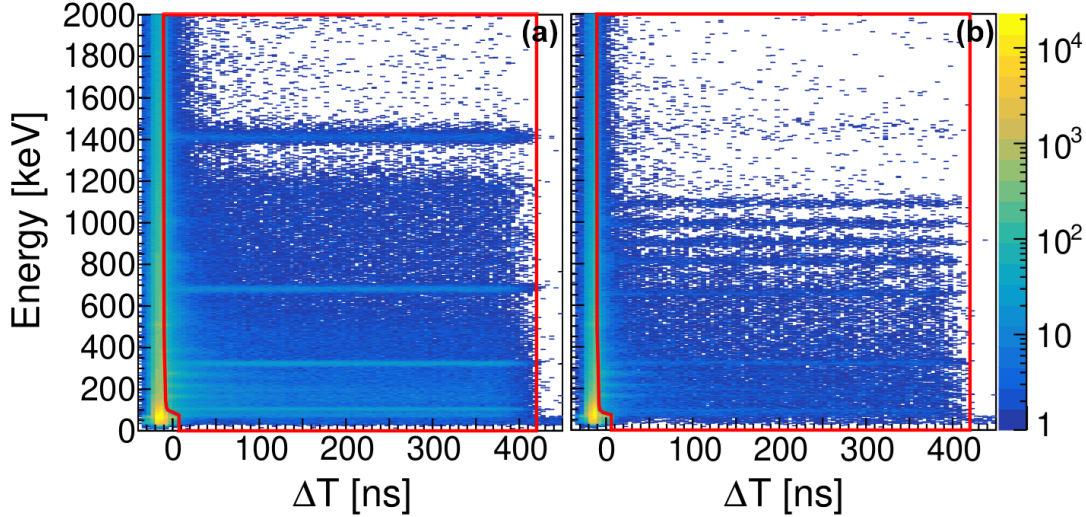


Figure 4.17: Energy vs time spectra for γ -rays obtained from FATIMA correlated to implantation of (a) ^{96}Pd and (b) ^{94}Pd ions. In addition the cleaning conditions to exclude the prompt flash (prompt flash cut) are shown in red.

4.5 E_γ - E_γ - ΔT matrices

The construction of the E_γ - E_γ - ΔT matrices was performed in the same way as for the PRD. As a reminder, the X axis represents the energy of the start detector, the Y axis - the energy of the stop detector and the Z axis is the time difference between the start and stop detectors (ΔT) according to Eq.4.5. Fig. 4.18 shows the E_γ - E_γ matrices obtained for ^{96}Pd and ^{94}Pd obtained by projecting the 3D cube on the XY 2D plane.

In an attempt to further clean the data correlated with ^{94}Pd ions, an additional condition was applied to the time difference axis, which allows for only γ rays detected within a certain time window to be taken into account. Multiple E_γ - E_γ - ΔT matrices were produced using different time windows: ± 5 ns, ± 10 ns, ± 20 ns, ± 40 ns and without a time gate. Fig. 4.18(b) and all following figures (until the end of this Chapter) were produced using the non-time-gated 3D cube.

Employing the background treatment procedures explained in the following

section, the final delayed and anti-delayed time distributions were produced for each 3D cube. The results will be discussed in Chapter 5.

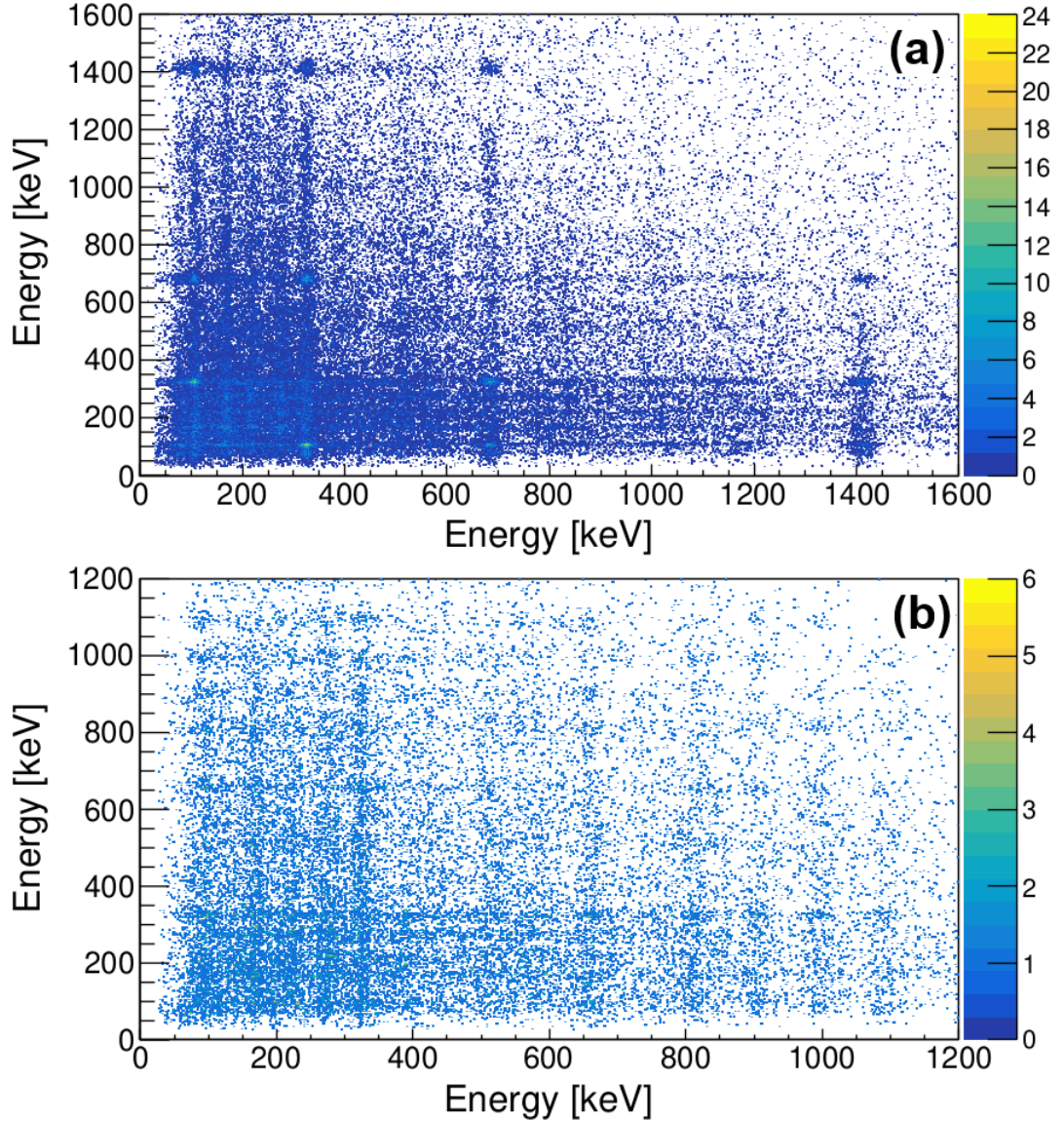


Figure 4.18: E_γ - E_γ matrices for (a) ^{96}Pd and (b) ^{94}Pd ions selected in the PID

4.6 Background treatment

Noting that the final goal is a precise measurement of nuclear lifetimes, background subtraction is a necessary procedure to eliminate the influence of lifetimes by background sources. In the following sections the background treatment for the two analysis methods, namely exponential fit and the GCD method, will be explained in detail. As an example, the procedure will be applied to 2^+ state in ^{96}Pd , fed by 684 keV γ ray and decaying by emitting 1408 keV γ ray.

4.6.1 Background treatment for exponential fit method

To treat the background for spectra, on which the exponential fit method will be applied, first the E_γ - E_γ - ΔT matrix is projected on its X axis. As shown in Fig. 4.19(a) this projection gives essentially the ^{96}Pd energy spectrum. The observed γ -ray peaks were identified and labeled in three colours: in black peaks associated with decays of excited states in ^{96}Pd , in blue - the 511 keV annihilation peak and in pink - neutron lines from $^{79,81}\text{Br}$ and ^{139}La isotopes.

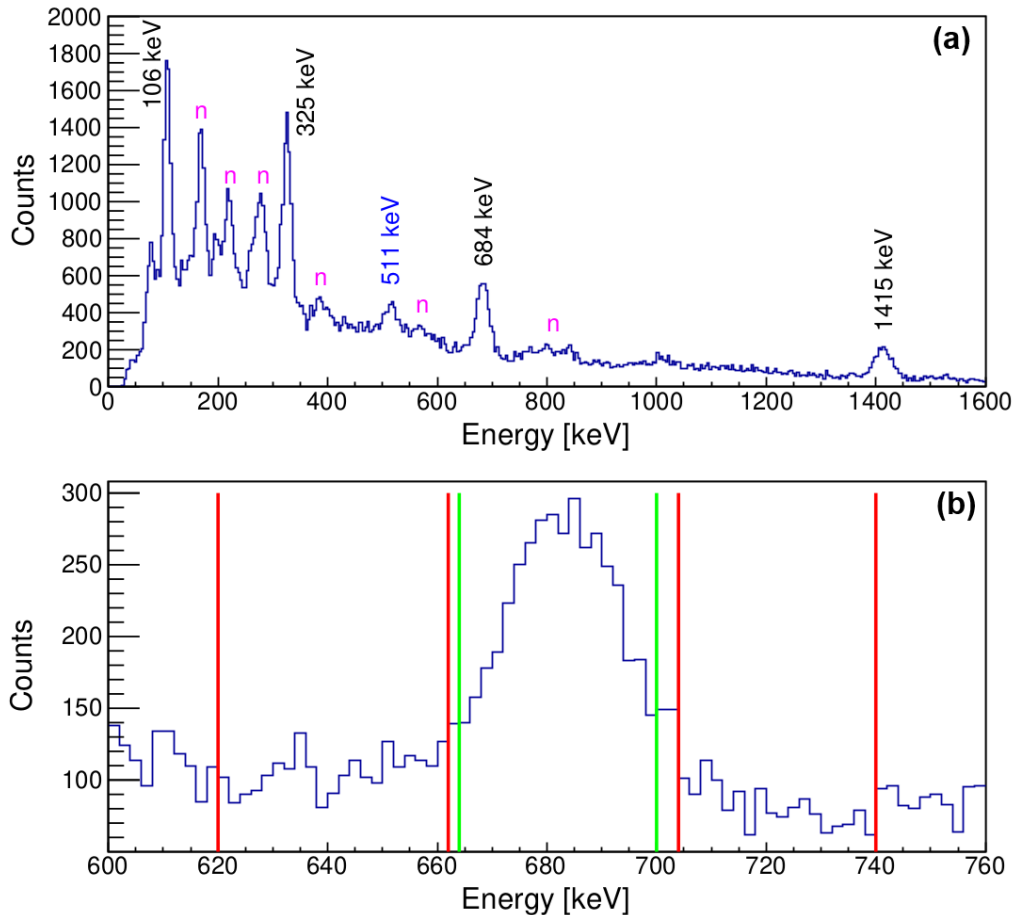


Figure 4.19: (a) ^{96}Pd energy spectrum, obtained by projecting the E_γ - E_γ - ΔT matrix on the X axis. (b) Gates set on peak (green) and background (red) events for the 684 keV line.

A total of three gates are set: a gate containing events within the 684 keV peak and two background gates on both side of it (see Fig. 4.19(b)). These gates are applied to the E_γ - E_γ - ΔT matrix, meaning that the events in the cube restricted by the X gates are projected on the YZ plane. However, before the XY 2D matrix is projected the events from the two background gates are summed and subtracted from the events within the gate containing the peak with a certain normalization factor. The normalization factor is based on the number of channels used for the peak and background gates. This procedure gives a background subtracted 2D

matrix.

The next step is to gate on the 1408 keV using the background subtracted 2D matrix. The XY matrix is projected on the Y axis obtaining the background subtracted energy spectrum as shown in Fig. 4.20(a). Here only γ -ray peaks in

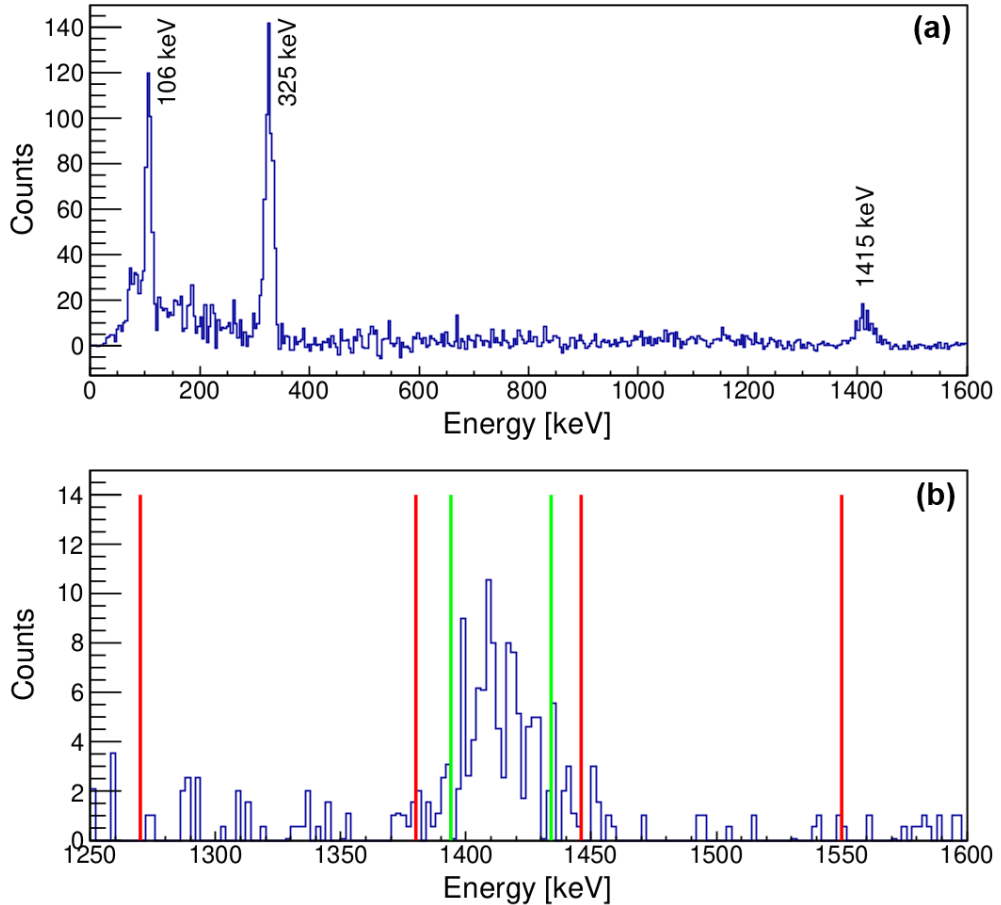


Figure 4.20: (a) Background subtracted ^{96}Pd coincidence spectrum for a gate on 684 keV. (b) Gates set on the coincidence energy spectrum, containing events within the peak (green) and background (red) events for the 1415 keV line.

coincidence with 684 keV are present. Similarly to the previous step three gates are set this time around the 1408 keV peak (see Fig. 4.20(b)). The events within the gates are projected on the Z axis, which corresponds to the time difference ΔT . The events within the background gates are once again summed and with a certain weight subtracted from the events within the peak gate. This results in a time distribution spectrum for the considered state. For the current case, the time distribution of feeding and decaying γ rays from the 2^+ state in ^{96}Pd , the spectrum is shown in Fig. 4.21.

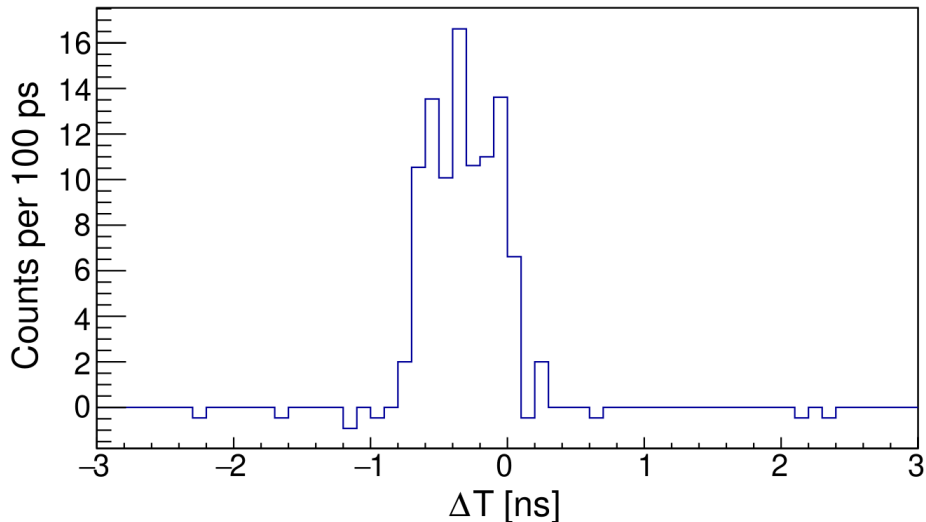


Figure 4.21: Background corrected time distribution for the 684 keV - 1415 keV cascade feeding and de-exciting the 2^+ state in ^{96}Pd .

4.6.2 Background treatment for the GCD method

The background treatment for the GCD method aims to correct for the contribution of the time-correlated Compton background underneath the full energy peaks. Unlike the background treatment employed for the exponential fit method, where spectra are subtracted from each other, the background treatment for the GCD method applies corrections directly to the experimental centroid differences.

First the E_γ - E_γ - ΔT matrix is projected on its X axis, obtaining the ^{96}Pd energy spectrum already shown in Fig. 4.19(a). As can be seen in Fig. 4.22(a), a total of two gates are applied: a gate containing events within the 684 keV peak (labeled as p1) and a background gate on the right side of the peak (labeled as bg1). Taking into account only the events within the gate on the 684 keV peak, the restricted YZ plane is projected on its Y axis (see Fig. 4.22(b)). Then two gates are set for the 1415 keV peak (see Fig. 4.22(c)): containing events within the peak (labeled as p2) and background events to the right (labeled as bg2). The next step is to produce three time distribution spectra by taking different combinations of the gates mentioned above. Employing the gates on the 684 and 1415 keV peaks the delayed peak-to-peak (p1p2) time distribution spectrum is obtained. In a similar fashion, the peak-to-background (p1bg2) and background-to-peak (bg1p2) delayed time distributions are produced. The three spectra are shown in blue in Fig. 4.23.

The same procedure is repeated once again for the anti-delayed time distributions by reversing the order in which the gates are applied (first gating on the 1415 keV line and then on 684 keV). The two sets of gates and the projection on the Y axis with restriction on events only within the 1415 keV peak gate, are

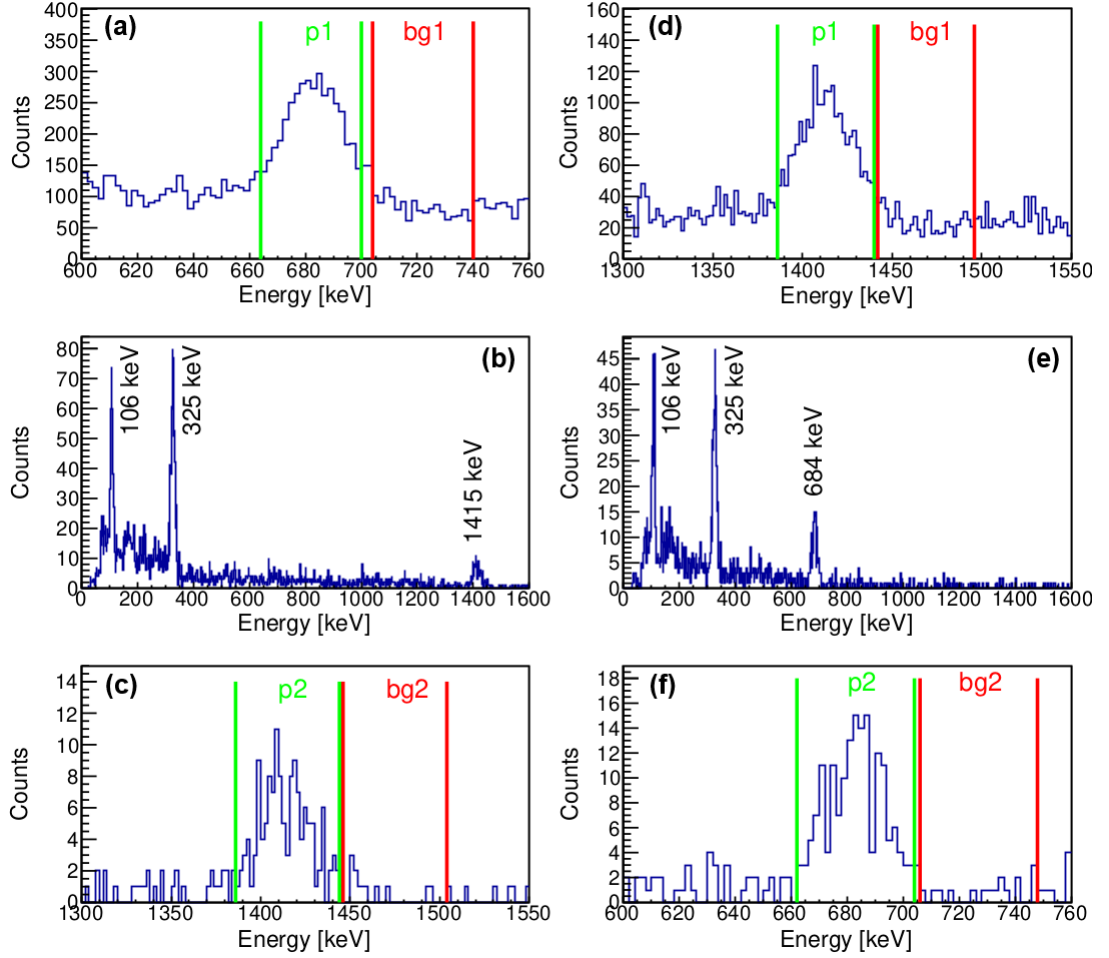


Figure 4.22: (a) Gates set on peak (green) and background (red) events for the 684 keV line. (b) ^{96}Pd coincidence spectrum, indicating γ rays in coincidence with the 684 keV transition. (c) Gates set on the coincidence energy spectrum, containing events within the peak (green) and background (red) for the 1415 keV line. (d) Gates set on peak (green) and background (red) events for the 1415 keV line. (e) ^{96}Pd coincidence spectrum, indicating γ rays in coincidence with the 1415 keV transition. (f) Gates set on the coincidence energy spectrum, containing events within the peak (green) and background (red) for the 684 keV line.

shown in Fig. 4.22(d),(e) and (f). This results in an additional three time distribution spectra: peak-to-peak, peak-to-background and background-to-peak, but for the anti-delayed case (shown in red in Fig. 4.23).

The centroids of all six time distributions are determined and three centroid differences are calculated:

$$\Delta C_{exp} = C_{delayed}(p1p2) - C_{anti-delayed}(p1p2) \quad (4.8)$$

$$\Delta C_{bg(feeder)} = C_{delayed}(p1bg2) - C_{anti-delayed}(bg1p2) \quad (4.9)$$

$$\Delta C_{bg(decay)} = C_{delayed}(bg1p2) - C_{anti-delayed}(p1bg2). \quad (4.10)$$

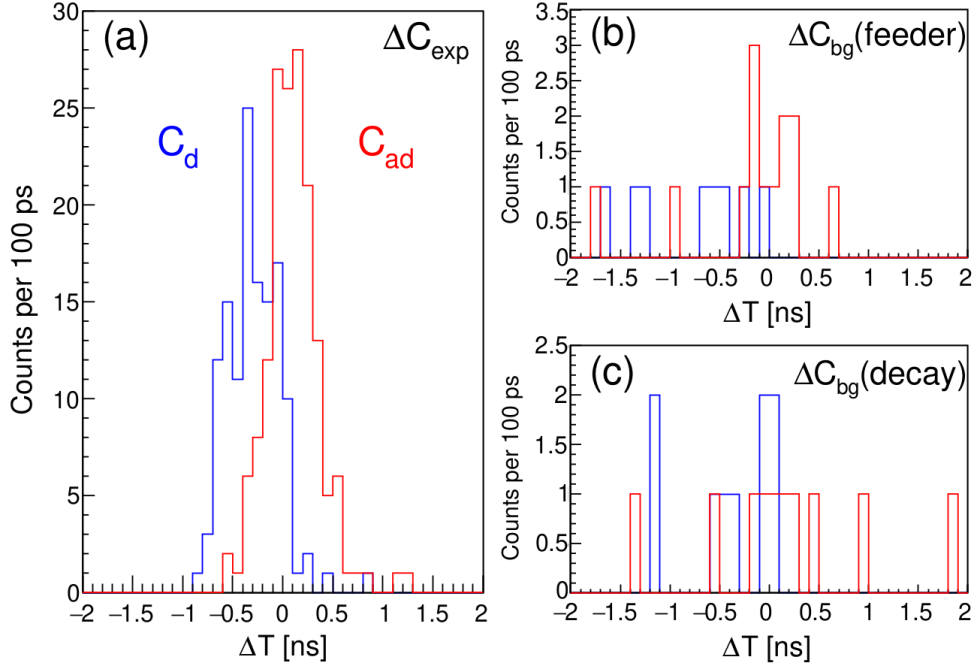


Figure 4.23: (a) Delayed (blue) and anti-delayed (red) time distributions produced employing the peak-to-peak gates. (b), (c) Delayed (blue) and anti-delayed (red) time distributions produced using peak-to-background and background-to-peak gates.

Two time corrections are obtained as follows:

$$t_{corr} = \frac{\Delta C_{exp} - \Delta C_{bg}}{P/B}, \quad (4.11)$$

where P/B represents the peak-to-background ratio. Finally, the corrected centroid difference ΔC_{FEP} is calculated using [82]:

$$\Delta C_{FEP} = \Delta C_{exp} + \frac{t_{corr}(decay) + t_{corr}(feeder)}{2}, \quad (4.12)$$

where $t_{corr}(decay)$ and $t_{corr}(feeder)$ are the two corrections. The centroid difference ΔC_{FEP} will be used to determine the lifetime of the state of interest, in this case the lifetime of the 2^+ state in ^{96}Pd . A table of the gates used during the data analysis is given in the following table.

Table 4.1: Energy gates, within which events were taken into account during background subtraction and lifetime measurement.

⁹⁶ Pd		⁹⁴ Pd	
E _γ [keV]	Gate [keV]	E _γ [keV]	Gate [keV]
106	96 - 120	96	88 - 106
325	312 - 340	324	312 - 338
684	664 - 700	660	640 - 676
1415	1386 - 1440	814	800 - 834
		905	882 - 922
		994	978 - 1018
		1092	1062 - 1108

Chapter 5

Results

Employing the calibrations and background treatment procedures explained in the previous chapter, time distribution spectra were produced for both direct feeder-decay coincidences and indirect ones. In this work, direct refers to coincidences between the transitions directly populating and depopulating a particular state. Then indirect coincidences are those, in which either one or both the feeder and decay transitions are indirectly (through another state(s)) feeding or de-exciting the state of interest. The obtained time distributions were analysed using the exponential fit and the GCD method and lifetimes of excited states in ^{96}Pd and ^{94}Pd were extracted.

The known lifetimes of the $I^\pi = 2^+, 4^+$ and 6^+ states in ^{96}Pd were re-measured in this work and used as to validate the setup and analysis procedure. The lifetimes of $I^\pi = 6^+$ and 8^+ states in ^{94}Pd were measured for the first time. In this chapter the results of the analysis will be presented.

5.1 ^{96}Pd benchmark case

The lifetimes of the excited states in ^{96}Pd are well known [18]. A partial level scheme of the excited states below the $I^\pi = 8^+$ isomer and basic decay information are shown in Fig. 5.1 [18]. The obtained results for this ion are compared to literature values and used as a way to verify the analysis procedure in the nanosecond lifetime region.

In terms of the GCD method, delayed (anti-delayed) time differences for excited states in ^{96}Pd are produced by assuming that the feeder (decay) of a certain state gives the start (stop) signal. The centroid difference is defined as the difference between the centroids of the delayed and anti-delayed time distributions. A deviation from the prompt distribution is an indication of a lifetime for the measured state. The centroids of the delayed and anti-delayed distributions are determined from the experimental spectrum and the centroid difference

$\Delta C = C_d - C_{ad}$ is calculated. After background treatment the lifetime can be determined using the relation: $\Delta C_{FEP} = PRD + 2\tau$, where the value PRD for a specific feeder-decay cascade can be obtained from the PRD calibration curve (see Fig. 4.14 and Fig. 4.15 in Chapter 4 Section 4.3).

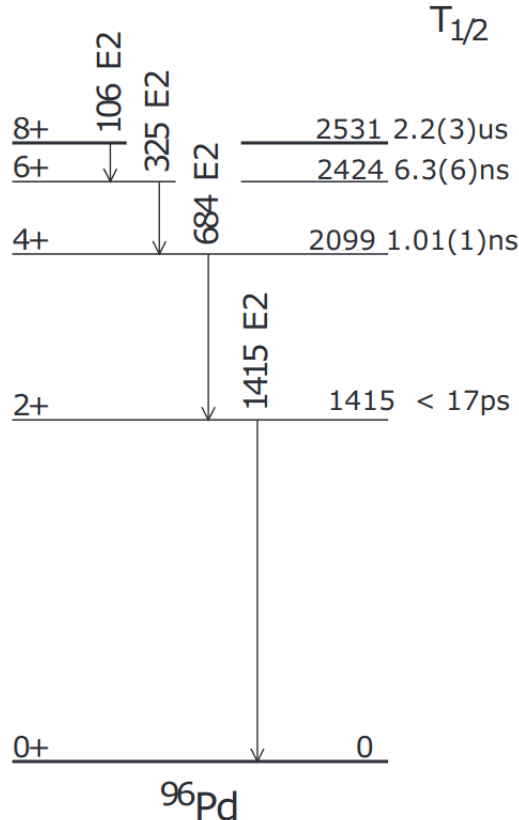


Figure 5.1: Partial level scheme of excited states below the 8^+ isomer in ^{96}Pd , including the spin, parity, energy and half-lives of the excited states as well as the type, multipolarity and γ -ray energies of the transitions. (Figure adapted from Ref. [18])

The time distributions analyzed using the exponential fit method are essentially delayed time distributions. After background subtraction, according to the procedure explained in Chapter 4 Section 4.6.1, an exponential function is fitted to the data. The slope of the exponent gives the decay constant λ and the mean lifetime (or half-life) of the studied state can be determined using the relation $\lambda = 1/\tau$ (or $\lambda = \ln(2)/T_{1/2}$).

The time distributions for the 2^+ state were produced using coincidences between the 684- and 1415-keV transitions. The spectrum in Fig. 5.2(a) was obtained after background subtraction according to the procedure employed for exponential fit analysis. It shows that this time distribution is symmetric and thus the lifetime of this state could not be measured by fitting an exponential function to the data. It was possible however to obtain the upper limit of $T_{1/2}(2^+) \leq 14$ ps using the GCD method. The used delayed and anti-delayed time distributions

before background correction are shown in Fig. 5.2(d). The determined limit represents the limitation of the current setup as explained in Chapter 4 Section 4.3.

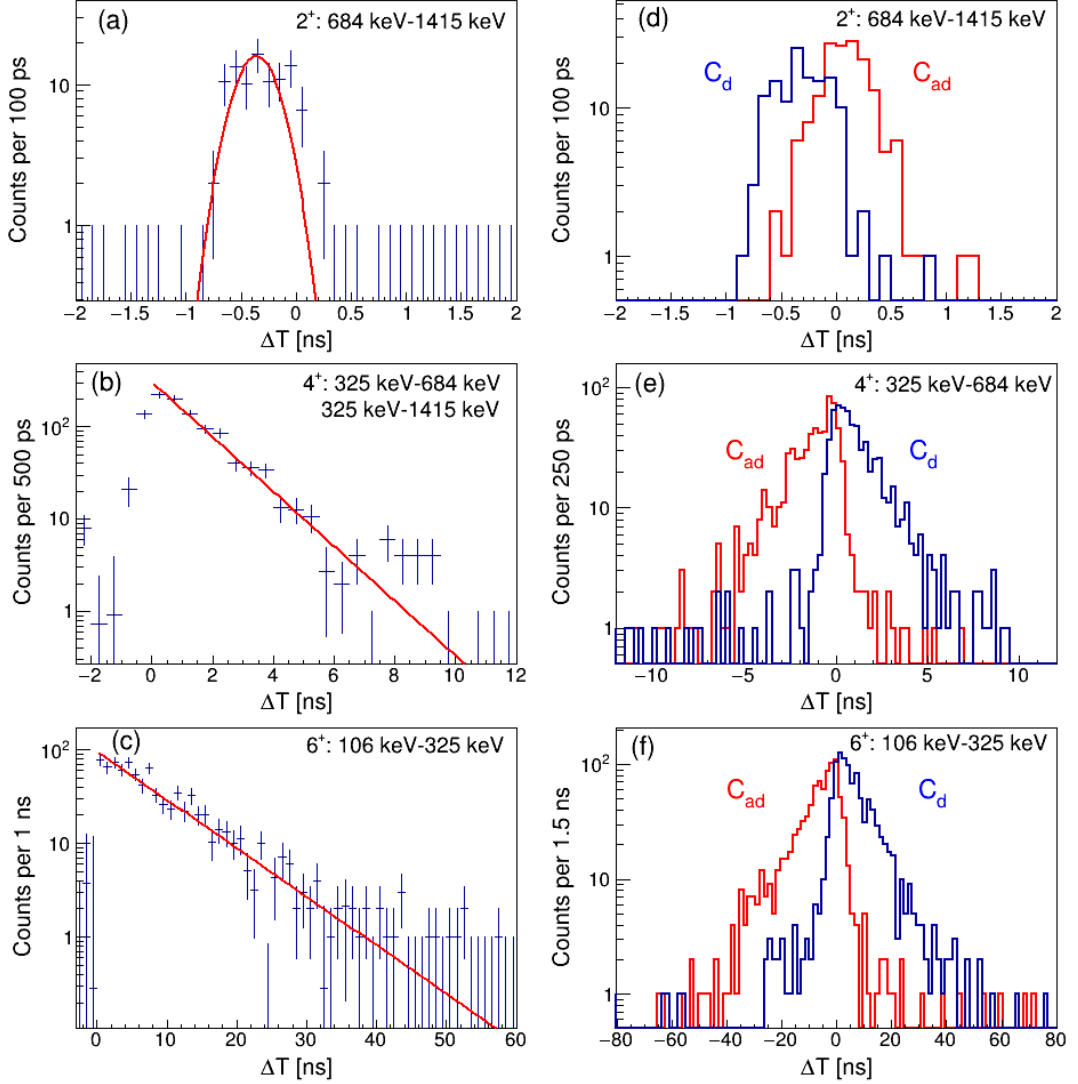


Figure 5.2: (a) Time distribution for the direct feeder and decay transitions of the 2^+ state in ^{96}Pd fitted with a Gaussian function. (b) Summed time distribution for the 4^+ state in ^{96}Pd containing events for coincidences between the 325- and 684-keV, and the 325- and 1415-keV transitions. The spectrum is fitted with an exponential function. (c) Time distribution for the direct feeder and decay transitions of the 6^+ state in ^{96}Pd fitted with an exponential function. (d) Delayed (blue) and anti-delayed (red) time distributions, obtained using the direct feeder-decay cascade for the 2^+ state in ^{96}Pd . (e) Delayed (blue) and anti-delayed (red) time distributions, obtained using the direct feeder-decay cascade for the 4^+ state in ^{96}Pd . (f) Delayed (blue) and anti-delayed (red) time distributions, obtained using the direct feeder-decay cascade for the 6^+ state in ^{96}Pd .

Taking into account the small lifetime of the 2^+ state, the 4^+ experimental decay was determined using not only the direct feeder-decay cascade 325 keV - 684 keV, but also the indirect 325 keV - 1415 keV. The background corrected

time distributions for these coincidences were added together, an exponential decay fit was applied to the summed spectrum (see Fig. 5.2(b)) and the half-life of $T_{1/2}(4^+) = 1.00(5)$ ns was obtained. In the case of GCD analysis, delayed and anti-delayed time distributions obtained from the direct and indirect coincidences are examined separately. The centroids of each time distribution were determined and the centroid difference was calculated for each coincidence. The time distributions for the direct coincidences are shown in Fig. 5.2(e). After background treatment and correcting for the PRD shift, the half-lives presented in Table 5.1 were obtained. After taking a weighted average of these values, the half-life of $1.00(5)$ ns was obtained.

Table 5.1: Centroid differences after background treatment, PRD values and half-lives for the coincidences used in the lifetime measurement of the 2^+ , 4^+ and 6^+ states in ^{94}Pd employing the GCD method.

I^π	coincidence	ΔC_{FEP} [ps]	PRD [ps]	$T_{1/2}$ [ps]
2^+	684 keV - 1415 keV	-381(34)	-374(10)	-2(12)
4^+	325 keV - 684 keV	2716(98)	-335(10)	1057(34)
	325 keV - 1415 keV	2038(130)	-709(10)	952(45)
6^+	106 keV - 325 keV	15460(467)	-865(59)	5658(163)

Indirect coincidences could not be employed when determining the lifetime of the 6^+ state due to the relatively long lived 4^+ state. Therefore, only the time distribution obtained for the direct feeder-decay cascade 106 keV - 325 keV was used for the lifetime measurement. By fitting an exponential function to the spectrum shown in Fig. 5.2(c), the half-life of $T_{1/2}(4^+) = 5.7(4)$ ns was obtained. The delayed and anti-delayed time distributions presented in Fig. 5.2(f) were analyzed using the GCD method and the half-life of $5.7(2)$ ns was determined.

The obtained limits and half-lives are consistent with the literature values of ≤ 17 ps, $1.0(1)$ ns and $6.3(5)$ ns for the 2^+ , 4^+ and 6^+ states respectively, published by H.Mach et al. [18]. Furthermore, the accuracy of the measured lifetimes for the 2^+ and 4^+ states was improved. A report on the obtained results is available in Ref. [83].

5.2 ^{94}Pd case

As the lifetimes of the states in ^{96}Pd were reproduced in good agreement with the published values, the analysis method was applied to excited states in ^{94}Pd . A level scheme of the known excited states in ^{94}Pd is presented in Fig. 5.3 [30, 31, 42–44]. Their lifetimes unknown, however predictions indicate half-lives in the order

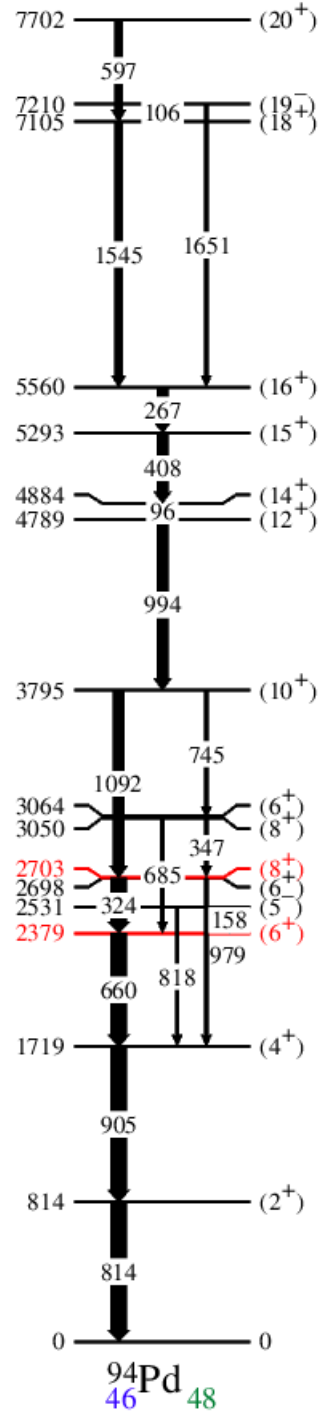


Figure 5.3: Level scheme of excited states in ^{94}Pd . The states of interest, namely 6^+ and 8^+ , measured in this work are marked in red.

of tens of picoseconds for the 6^+ state and ~ 1 ns for the 8^+ state [84]. Under the assumption that the 2^+ , 4^+ , 10^+ and 12^+ states decay promptly in comparison to the states of interest, both direct and indirect coincidences were used in the lifetime measurement of the 6^+ and 8^+ intermediate states.

As previously explained in Chapter 4 Section 4.5, multiple E_γ - E_γ - ΔT matrices were produced employing different time windows: ± 5 ns, ± 10 ns, ± 20 ns,

± 40 ns and without a time gate. Delayed and anti-delayed time difference distributions were produced for both direct and indirect coincidences, and for all matrices. Employing the background treatment procedures explained in the previous chapter, the half-life values of the 6^+ and 8^+ states were determined using the GCD method. The results from the different matrices were compared based on their error to value ratios. It was established that despite the reduction in statistics within the time distributions (due to the narrow gate), the results from the matrix with a ± 5 ns gate had the best ratio. In the following paragraphs the results from two of the time gated matrices will be compared and discussed.

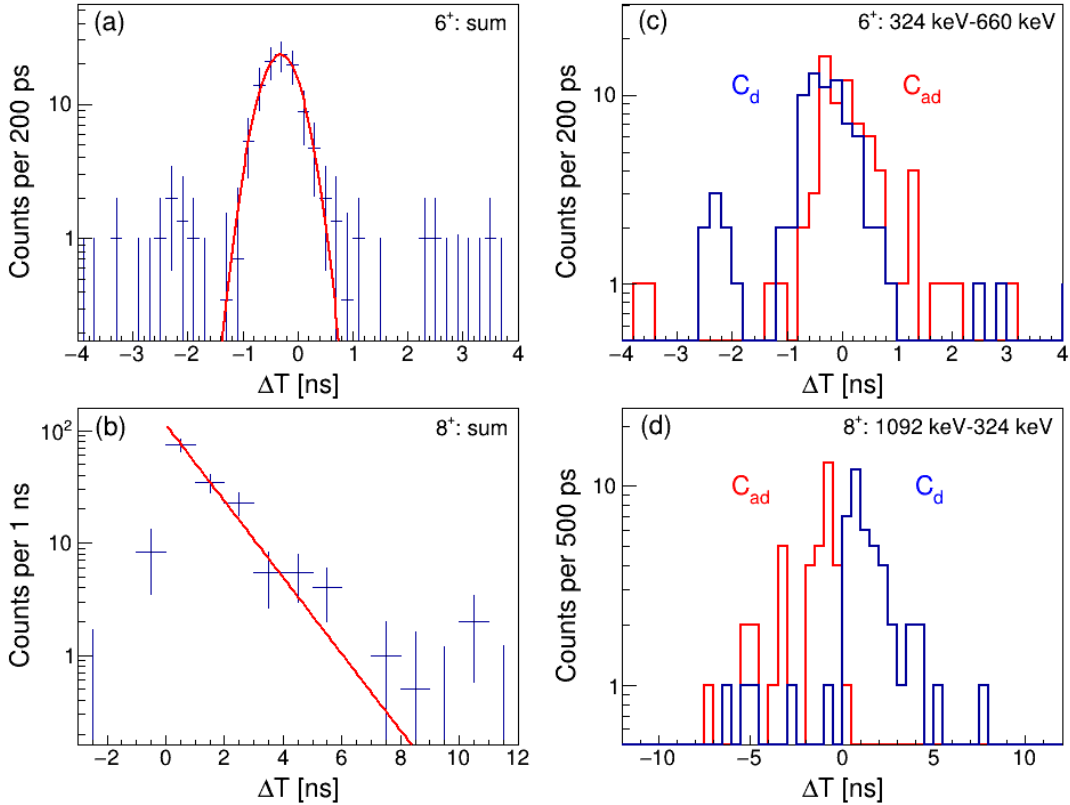


Figure 5.4: (a) Summed time distribution for the 6^+ state in ^{94}Pd containing events from three coincidences (see text for more details). The spectrum is fitted with a Gaussian function. (b) Summed time distribution for the 8^+ state in ^{94}Pd containing events for eight coincidences (see text for more details). The spectrum is fitted with an exponential function. (c) Delayed (blue) and anti-delayed (red) time distributions, obtained using the direct feeder-decay cascade for the 6^+ state in ^{94}Pd . (d) Delayed (blue) and anti-delayed (red) time distributions, obtained using the direct feeder-decay cascade for the 8^+ state in ^{94}Pd .

To measure the half-life of the 6^+ state the direct coincidence between the 324- and 660-keV transitions, as well as the two indirect coincidences between 324 and 905 keV, and 324 and 814 keV were examined. In the first instance, the 8^+ state was studied using the direct coincidence between the 1092- and 324-keV transitions. In view of its long lifetime the indirect coincidences between

the 96-, 994-, 1092-keV feeding and the 324-, 660-, 905-, 814-keV de-exciting transitions were also studied. Delayed and anti-delayed time difference distributions were produced for each coincidence and their centroids were determined. Fig. 5.4(a)-(d) shows the time distributions for direct coincidences for both matrices and both states of interest. A lifetime value for each cascade was obtained after background treatment and PRD correction. A summary of the PRD values, background-corrected centroid differences and half-live values measured using the non-gated E_γ - E_γ - ΔT matrix and the matrix with a time window of ± 5 ns are presented in Table 5.2. The few missing values in the table are due to empty coin-

Table 5.2: Summary of the values used for the measurement of the half-lives of the 6^+ and 8^+ states in ^{94}Pd employing the GCD method using matrices with different restrictions on the time between two registered γ rays.

I^π	coincidence	PRD [ps]	no time gate		± 5 ns gate	
			ΔC_{FEP} [ps]	$T_{1/2}$ [ps]	ΔC_{FEP} [ps]	$T_{1/2}$ [ps]
6^+	324 keV - 660 keV	-320(10)	-359(298)	-14(73)	-705(149)	-133(52)
	324 keV - 905 keV	-470(10)	-808(308)	-117(70)	-438(170)	11(59)
	324 keV - 814 keV	-418(10)	-135(402)	98(89)	-355(216)	22(75)
8^+	1092 keV - 324 keV	558(59)	2860(660)	798(161)	2738(300)	755(106)
	1092 keV - 660 keV	246(59)	2185(1002)	672(279)	2601(387)	816(136)
	1092 keV - 905 keV	98(59)	2063(823)	681(156)		
	1092 keV - 814 keV	150(59)	2017(1361)	647(320)		
	994 keV - 324 keV	508(59)	3075(751)	890(146)	3375(236)	994(84)
	994 keV - 660 keV	196(59)	2329(1273)	739(299)	2179(487)	687(170)
	994 keV - 905 keV	48(59)	2707(1341)	921(253)	2935(626)	1001(218)
	994 keV - 814 keV	100(59)	1693(1458)	552(281)		
	96 keV - 324 keV	-1043(59)	1076(506)	735(125)	1226(269)	786(95)
	96 keV - 660 keV	-1355(59)	1256(723)	905(163)	711(316)	716(112)
96 keV - 905 keV	-1503(59)	259(790)	611(217)	1148(414)	919(145)	
96 keV - 814 keV	-1451(59)	764(998)	768(224)	782(460)	774(161)	

cidence spectra, which leads to the inability to perform the background treatment procedure.

Table 5.3 presents limits and half-life values for the states of interest, obtained from a weighted average (w.a.) of the individually determined excited-state half-lives (see Table 5.2) over the number of events within the time-distribution spectra. In particular, for the 6^+ state both direct and indirect coincidences were used, while for the 8^+ state a weighted average is determined using only indirect coincidences.

As previously mentioned, the results obtained using the 3D matrix with a ± 5 ns gate have a better value to error ratio. In addition, a comparison between the half-lives of the 8^+ state for direct and indirect coincidences (Table 5.3) show that the results obtained from the matrix without a time gate are indistinguishable within their error bars. However, the same can not be stated for the half-lives determined using the matrix with a ± 5 ns gate. Taking this into account, the value of $T_{1/2}(8^+) = 755(106)$ ps and the limit of $T_{1/2}(6^+) \leq 40$ ps are taken as final and used to determine the reduced transition strengths $B(E2)$. These experimental results will be discussed and compared to different theoretical calculations in the next chapter.

Table 5.3: Summary of the values used for the measurement of the half-lives of the 6^+ and 8^+ states in ^{94}Pd employing the GCD method using matrices with different restrictions on the time between two registered γ rays.

I^π	measurement	$T_{1/2}$ [ps]	
		no time gate	± 5 ns gate
6^+	w.a.	≤ 50	≤ 40
8^+	direct coinc.	798(161)	755(106)
	w.a. w/o direct coinc.	760(63)	825(48)

Chapter 6

Discussion

In this chapter the experimental results obtained for the $I^\pi = 6^+$ and 8^+ yrast states in ^{94}Pd will be discussed within the shell-model framework. The main goal is to gain insight into the interplay between the isoscalar ($T = 0$) and isovector ($T = 1$) coupling of proton-neutron pairs. In addition, potential energy surface plots for states in $^{92,94,96}\text{Pd}$ will be introduced.

Using the experimentally measured lifetimes $T_{1/2}(8^+) = 755(106)$ ps, $T_{1/2}(6^+) \leq 40$ ps and the lifetime of the 14^+ isomeric state taken from Ref. [34], the reduced transition probability strengths $B(E2)$ were calculated. These are summarized and compared to two shell-model approaches (JUN45, GDS) in Table 6.1 and Fig. 6.1. A comparison between the experimentally-established level energies together with the known γ rays and the results from the two shell-model calculations in the full diagonalization of the nuclear Hamiltonian is shown in Fig. 6.2.

The first shell-model calculation uses the JUN45 interaction [11] in the full $\pi\nu(f_{5/2}pg_{9/2})$ model space with effective charges of $e_\pi = 1.5e$ and $e_\nu = 1.1e$, according to Ref. [11]. This well-known phenomenologically-tuned realistic interaction is based on the Bonn-C potential and has been used to reproduce many

Table 6.1: Experimental half-lives expressed in ns and $B(E2)$ strengths in $e^2 fm^4$ for excited states in ^{94}Pd compared to various shell-model approaches. The experimental half-life value for the yrast $I^\pi = 14^+$ state is taken from Ref. [34].

Quantity [$\text{ns}/e^2 fm^4$]	$I_i^\pi - I_f^\pi$		
	$14^+ \rightarrow 12^+$	$8^+ \rightarrow 6^+$	$6^+ \rightarrow 4^+$
$T_{1/2}$	515(1)	0.755(106)	≤ 0.04
$B_{exp}(E2)$	52.1(1)	205_{-25}^{+34}	≥ 113
$B_{JUN45}(E2)$	101	252	453
$B_{GDS}(E2)$	49	192	548
$B_{g_{9/2}}(E2)$	112	144	398

nuclear properties from the $N = 3$ harmonic oscillator shell and the region of ^{56}Ni approaching ^{100}Sn . While Fig. 6.2 shows that the experimental yrast level energies are well reproduced in this calculation, Fig. 6.1 indicates that the calculated $B(E2)$ values for the excited states in ^{94}Pd are largely overestimated compared to the experimental data. This is most probably due to the strong mixing of the upper fp shell with the $g_{9/2}$ orbital, which is characteristic for this interaction and is required for lighter nuclei in order to substitute the missing $f_{7/2}$ orbital in the corresponding model space.

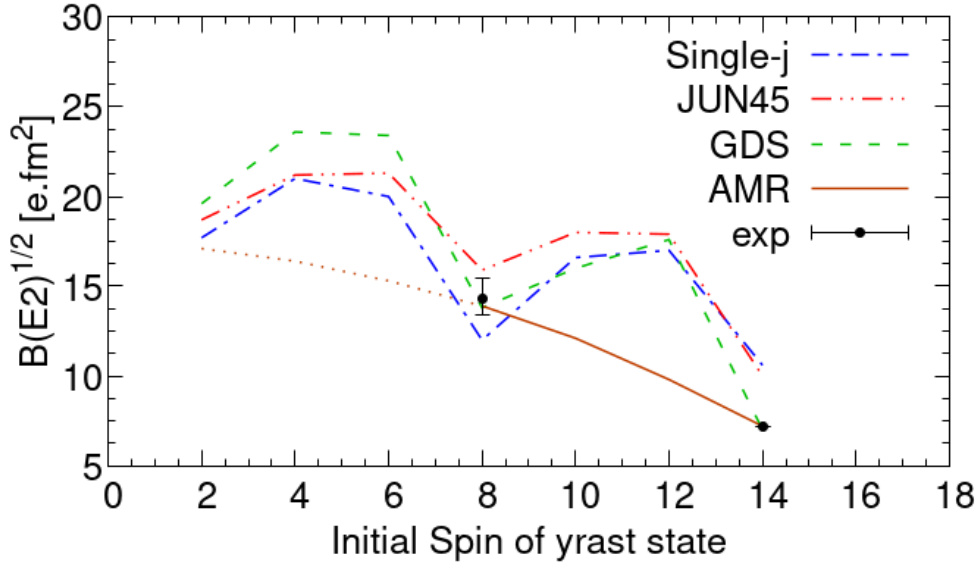


Figure 6.1: Experimental and shell-model calculated $B(E2)^{1/2}$ values, using different effective interactions and model spaces (see text), for states in ^{94}Pd .

The second calculation is a Large Scale Shell Model (LSSM) calculation employing the GDS interaction [12], which is derived from the CD-Bonn interaction. The inclusion of core excitations (up to $5p5h$) in the $\pi\nu(gds)$ model space, with effective charges of $e_\pi = 1.1e$ and $e_\nu = 0.84e$ [85], displays a good agreement between the experimental and calculated high spin states (see Fig. 6.2) as well as an almost exact reproduction of the reduced transition rates (see Fig. 6.1).

Due to the good agreement between the experimental versus shell-model calculated energy levels and more importantly $B(E2)$ values for the GDS approach, the potential energy surface (PES) of $^{92,94,96}\text{Pd}$ were produced in order to access the structure of the involved states, and the associated nuclear deformation. The calculations were performed following the example of Ref. [86, 87], using the $\pi\nu(gds)$ valence space and effective GDS Hamiltonian. The PES of the $I^\pi = 0^+$ ground states of the three nuclei displayed in Fig 6.3 clearly predict an evolution of the (β, γ) distributions in the wave functions, from sphericity in ^{96}Pd towards a more axially-deformed prolate shape in the $N = Z$ ^{92}Pd nucleus. The $T_z = +1$

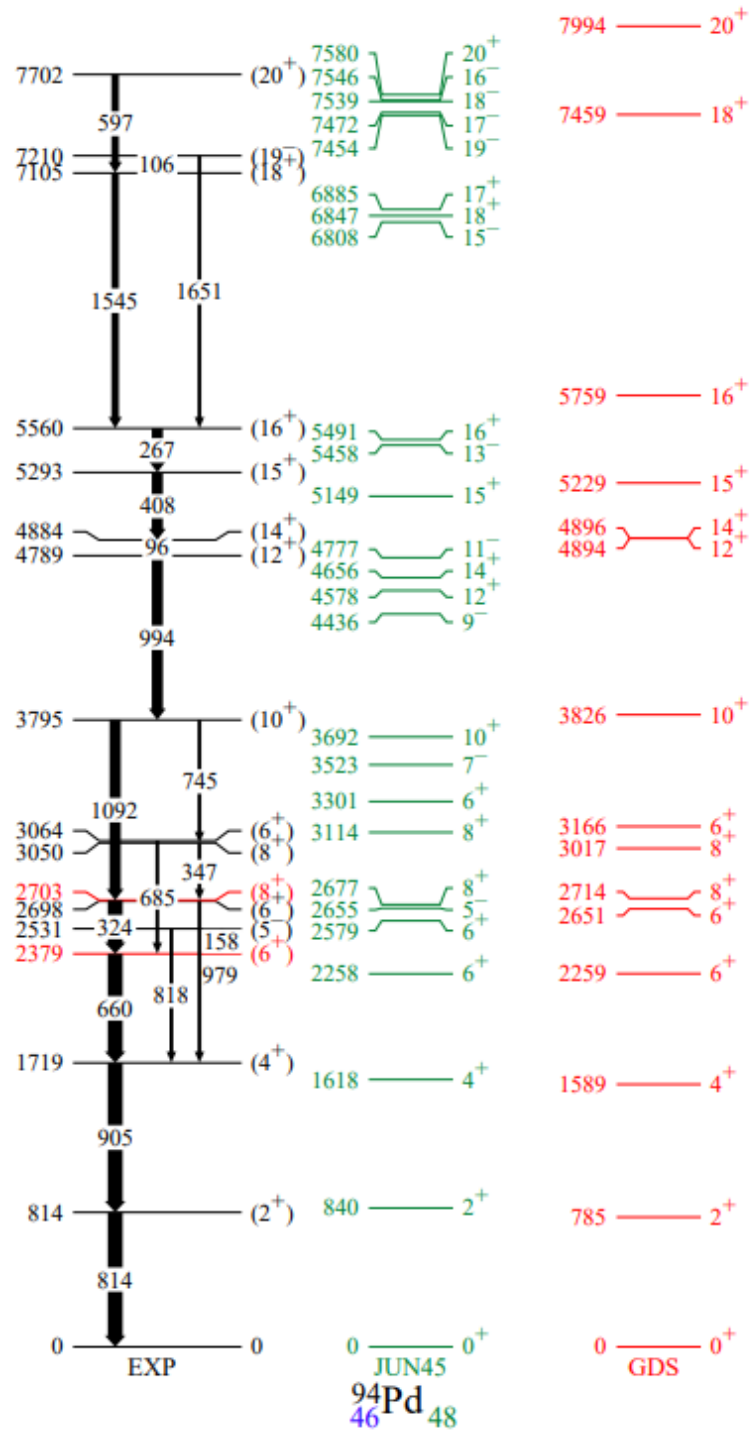


Figure 6.2: Experimental [30, 31, 42–44] and shell-model calculated level schemes of excited states in ^{94}Pd . The latter employ the JUN45 [11] and GDS [12] interactions.

^{94}Pd nucleus, as the transitional case between the two extremes, displays a shallow prolate minimum, where the ground-state wave function is dominated by contributions around $\beta \sim 0.1 - 0.2$. While the spherical shape is maintained for the $I^\pi = 8^+$ state in ^{96}Pd , the deformation pattern of the other two nuclei shifts towards sphericity and remains as such up to higher spins, in particular for the 14^+ state in ^{94}Pd . It should be noted that within the configuration space, no other coexisting minima are observed for either ^{92}Pd or ^{94}Pd . This is at variance with the claim made in Ref. [46], which links the $T = 0$ pn -pairing component to the emergence of prolate deformation and shape coexistence in ^{94}Pd

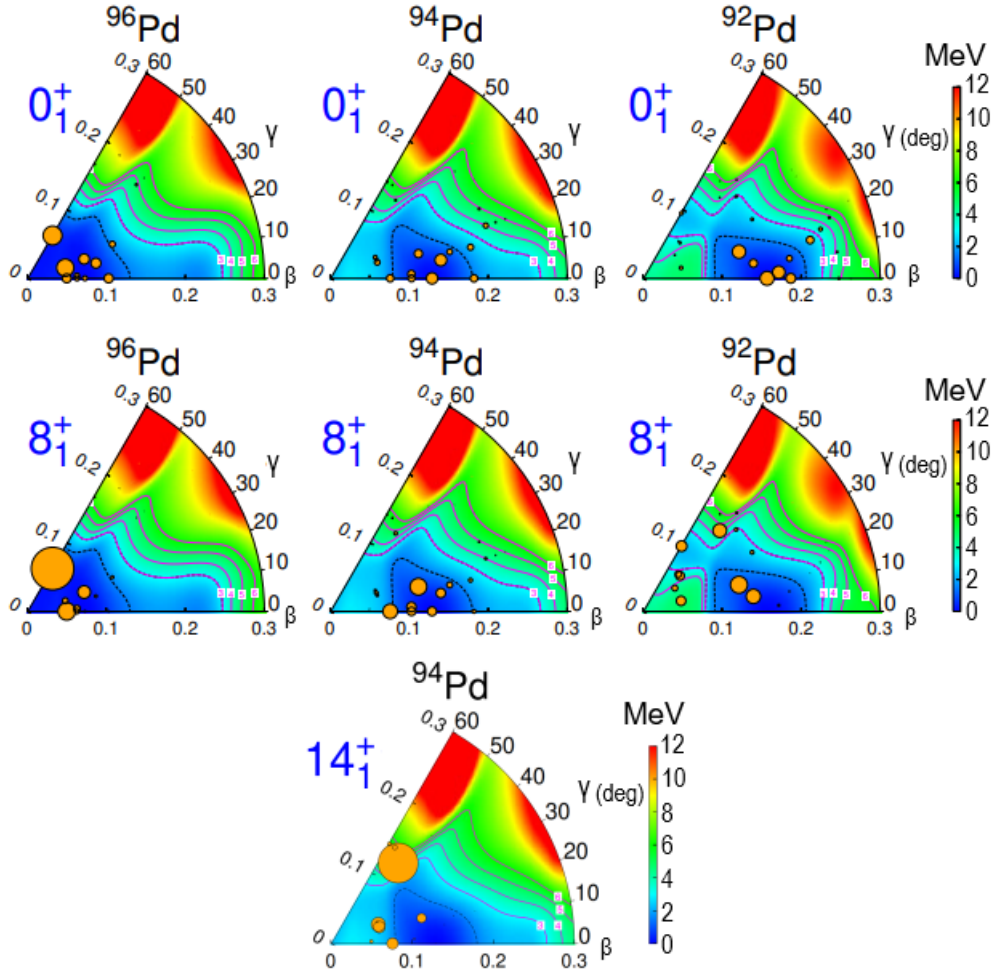


Figure 6.3: Potential energy surface (PES) plots for the ground states as well as for the first $I^\pi = 8^+$ states in $^{96,94,92}\text{Pd}$ nuclei. Additionally, the PES for the $I^\pi = 14^+$ isomeric yrast state in ^{94}Pd .

In addition to the two shell-model calculations explained above, the excited-state lifetimes were also analysed within the single- $0g_{9/2}$ model. This study aims at disentangling and quantifying the contributions of the isoscalar ($T = 0$) versus isovector ($T = 1$) components of the pn shell-model interaction to the structure of ^{94}Pd . The previous discussion indicates that in order to describe the nuclear

qualities of this nucleus a multi-orbital model space, which includes cross shell $N, Z = 50$ excitations, is needed. However, the isoscalar and isovector components are not orthogonal, i.e. they can overlap. Using this reasoning and the prominent role, which the $0g_{9/2}$ orbital plays in the low-lying states of nuclei around $N, Z = 50$ [12, 26, 37–39], the use of this simplified single-j model can be justified for the spherical or slightly-deformed nature of Pd nuclei. Using the LSSM approach it was calculated that the wave-function overlap of all ^{94}Pd states with the $(\pi 0g_{9/2})^4 \otimes (\nu 0g_{9/2})^2$ configuration exceeds 95%. Thus for the single $0g_{9/2}$ calculation an effective two-body interaction was used, based on the high-precision CD-Bonn NN potential [88]. Employing the effective charges of $e_\pi = 1.5e$ and $e_\nu = 1.1e$, the energies and $B(E2)$ values of the states in ^{94}Pd were calculated (further details of the calculations can be found in Ref. [89]). In addition, results were obtained separately by removing the $T = 0$ and $T = 1$ pn matrix elements. It is important to note, that the seniority coupling, which involves only isovector $T = 1$ proton-proton (pp) and neutron-neutron (nn) interactions, is always taken into account and only components of the pn interaction are excluded in the discussed cases.

In Fig.6.4 the calculated energy levels for the full interaction (labeled as SM) are compared to experimental data. The remaining two level schemes are obtained for the pure $T = 0$ case by removing the $T = 1$ part of the pn interaction and for pure $T = 1$ by removing the $T = 0$ part. The energies of the yrast levels of ^{94}Pd are reasonably-well reproduced using any of the discussed interactions. The excited states in all three cases however expand over a different energy interval. In Ref. [89] a similar study is conducted for the $N = Z$ system ^{92}Pd , where the experimental energy levels are very well reproduced by the calculations using the full interaction. The same structure is obtained when considering only the pure $T = 0$ pn component. In contrast, when only the $T = 1$ component is taken into account the excited states are compressed in a smaller energy interval, resembling a seniority type spectrum. These findings are supported by Ref. [3, 26] and suggest that the evolution from seniority in ^{96}Pd to a vibrational-type spectrum in ^{92}Pd , with ^{94}Pd exhibiting an intermediate character, could be associated with influence of the $T = 0$ pn interaction.

Using the same three cases for the interaction as discussed above, the $B(E2)$ transition strengths were calculated for the $I_\pi = 6^+, 8^+$ and 14^+ yrast states in ^{94}Pd . It is important to note that this is the first time this kind of analysis is performed for the $B(E2)$ strengths. In addition, the goal of this investigation is not the reproduction of the experimental values but an attempt to disentangle the relevant isovector versus isoscalar components of the pn interaction. In Fig. 6.1 the results of the full interaction are compared to the experimental $B(E2)$ values

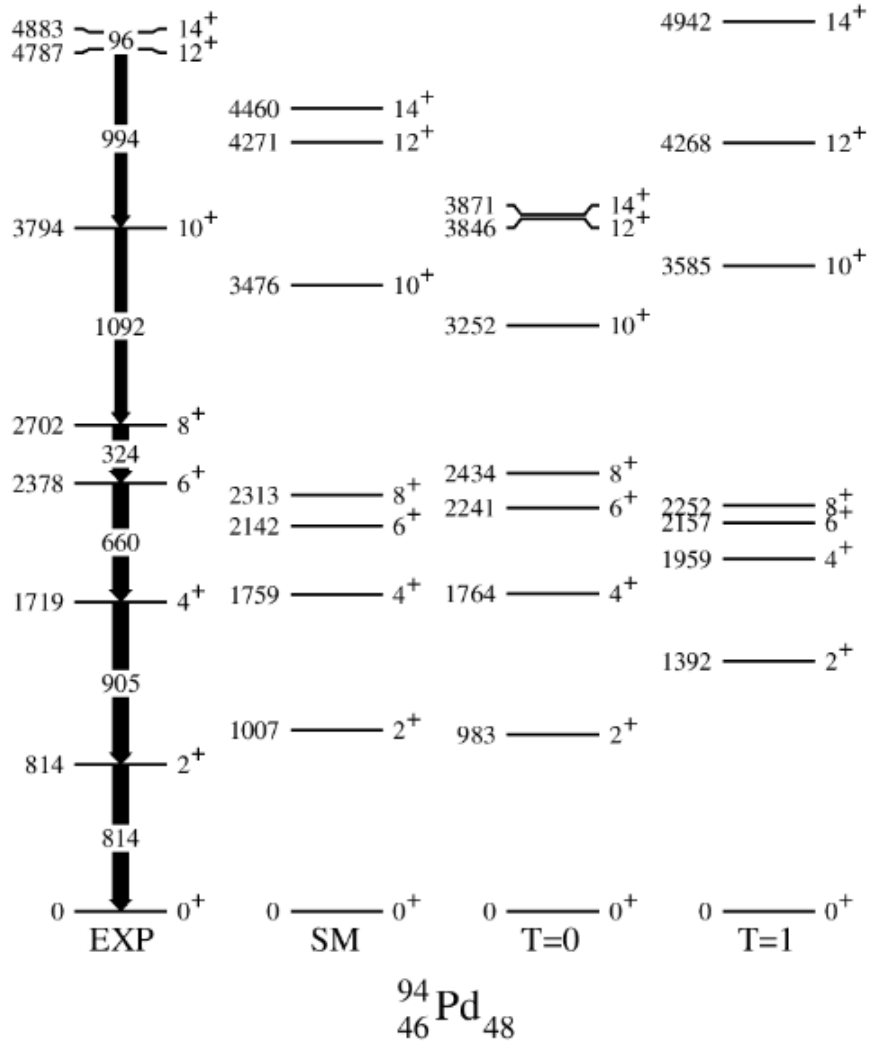


Figure 6.4: Experimental level scheme of excited states in ^{94}Pd compared to shell-model predictions. In addition to the full interaction (SM), results are shown for pure $T = 0$ and pure $T = 1$ pn interactions. The seniority coupling, which involves only isovector $T = 1$ proton-proton (pp) and neutron-neutron (nn) interaction, is always taken into account.

and other shell-model calculations. The predicted behaviour for the single $g_{9/2}$ approach is similar to those obtained for the JUN45 and GDS calculations, however it is evident that GDS provides the best reproduction of the experimental results, highlighting the importance of core excitations. Moreover, the calculations presented in Table 6.2 indicate that excluding the $T = 1$ component from the pn interaction does not cause significant changes to the calculated $B(E2)$ values with respect to the results obtained using the full interaction for the decay of the $I_\pi = 6^+, 8^+$ and 14^+ yrast states. On the other hand, when excluding the $T = 0$ component and thus considering a pure $T = 1$ force, significantly longer

Table 6.2: Experimental $B(E2)$ values in $e^2 fm^4$ for excited states in ^{94}Pd compared to shell-model calculations using different combinations of isoscalar and isovector interactions - full, pure $T = 0$ and pure $T = 1$ pn interactions.

Quantity [$\text{ns}/e^2 fm^4$]	$I_i^\pi - I_f^\pi$		
	$14^+ \rightarrow 12^+$	$8^+ \rightarrow 6^+$	$6^+ \rightarrow 4^+$
$B_{exp}(E2)$	52.1(1)	205_{-25}^{+34}	≥ 113
$B_{g_{9/2}}(E2)$	112	144	398
$B_{g_{9/2}T=0(pn)}(E2)$	82	191	398
$B_{g_{9/2}T=1(pn)}(E2)$	9	11	5

half-lives are predicted. This suggests that the structure of the wave functions resulting from the pure $T = 1$ interaction cannot sufficiently produce fragmentation of the basis states arising from the $(\pi 0g_{9/2})^4 \otimes (\nu 0g_{9/2})^2$ configuration.

Another calculation presented in Fig. 6.1 uses the schematic Anti-Magnetic Rotational (AMR) model [45]. AMR is a modification of the Magnetic Rotational model, which aims to explain regular rotational bands in near-spherical nuclei. Assuming that valence particles and valence holes in a spin-aligned configuration form shears blades, by closing the shear blades the regular rotational sequence can be obtained. For AMR the particles and holes arrange themselves in such a way that the spin increases by a unit of two along the band and there is no magnetic radiation. Ref. [45] demonstrates a good reproduction of the yrast states in ^{92}Pd using this coupling scheme. Based on a similar 4 quasiparticle configuration as for the ground state of ^{92}Pd , the calculation for ^{94}Pd suggests that the shears closing behaviour takes over beyond $I^\pi = 8^+$ state. An explanation for this could be that the $T = 1$ proton-proton and neutron-neutron pairs in the $g_{9/2}$ orbitals rearrange themselves and form two oppositely aligned $T = 0$ proton-neutron shear blades. The closing of the shears generates the high-spin states of ^{94}Pd up to $I^\pi = 16^+$, where the shears blades are maximally aligned. The experimental transition rates measured in the current work are very well reproduced by the AMR calculations shown in Fig. 6.1 (denoted by solid line).

Chapter 7

The HISPEC Slowed-Down Beam concept and test experiment

The two main techniques employed for production and study of exotic radioactive beams are Isotope Separation OnLine (ISOL) and in-flight separation. In simple terms, radioactive ions in ISOL facilities are produced in reaction targets at thermalized energies, ionized, extracted and then reaccelerated [90]. Depending on the chemical properties of the isotopes it may be difficult to extract some of them from the production target, resulting in an insufficient intensity of the secondary beams. Additionally, the lifetimes that can be studied are restricted by the time scale of the extraction and reacceleration processes.

On the other hand, in-flight facilities employ heavy-ion accelerators, a production target and a separation device. It is important to note that the properties and quality of the secondary beam are directly related to those of the primary beam. By using the high velocities of the projectiles and employing thick secondary targets, in-flight facilities can overcome one of the limitations of ISOL facilities and increase reaction yields. Moreover, by slowing down the secondary beams using a thick homogeneous degrader, short lived nuclei with high survival rate after the deceleration can be accessed and studied.

The High resolution In-flight SPECTroscopy (HISPEC) Slowed-Down Beams (SDB) as a concept aims at the production of exotic radioactive beams with energies around 5-10 MeV/u at the Super-FRS [56] located at the upcoming FAIR Facility for Antiproton and Ion Research GmbH, Germany [57, 91]. One of the advantages of these low energy beams comes from the slower interaction time, which allows for multi-step Coulomb excitations, resulting in the population of high spin states [92]. In addition, the use of radioactive beams at Coulomb barrier energies allows for the application of transfer, resonance and fusion evaporation reactions.

The secondary radioactive beams for HISPEC will be produced by in-flight

projectile fragmentation or fusion. At the final focal plane of the Super-FRS they will be slowed down to energies around the Coulomb barrier using a thick degrader before impinging on a thin secondary target, placed at the center of a γ array for multi-step Coulomb excitations of the fragments and detecting the decaying γ rays. However, the slowing-down process of the nuclei through thick matter causes energy and angular straggling, reducing the beam quality. This leads to the need for tracking and energy measurement of the beam particles following the degrader. In addition, Doppler correction for the γ rays emitted in-flight after the Coulomb excitation is essential. In order to reconstruct the kinematics of the reaction the velocity of the fragments needs to be precisely known. This can be achieved via ToF (time-of-flight) measurement between two beam tracking detectors. One should note that to prevent further straggling and deterioration of the beam, the tracking detectors need to be as thin as possible and large enough to cover the full angular distribution of the slowed-down beam. For particle identification a $\Delta E - E$ telescope will be used, placed downstream of the target. A schematic layout of the setup is shown in Fig. 7.1.

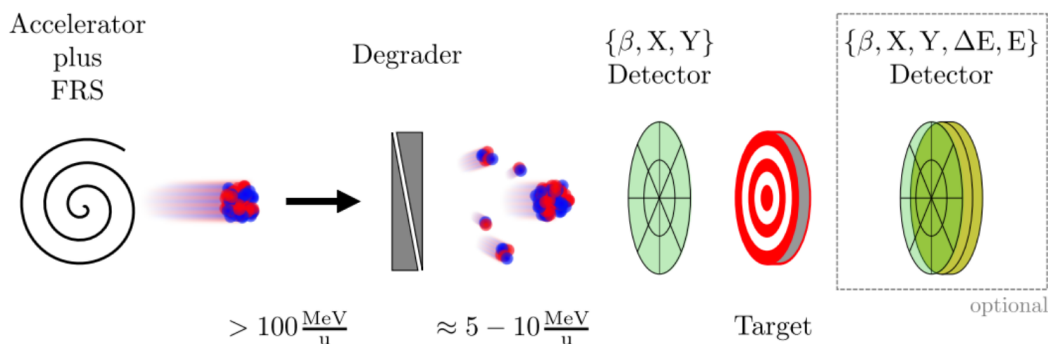


Figure 7.1: Schematic layout of the SDB setup. Taken from [93]

Ref. [94] reports on the results of a previous experiment, aiming to test the feasibility of the slowed down beam setup employing the FRS at GSI. A ^{64}Ni beam at 250 MeV/u was slowed down to 13 MeV/u in a thick aluminum degrader. A MOCADI simulation [95] was performed and showed good agreement with the experimental spread and nuclear reaction yields. Subsequently, another test experiment was scheduled and performed at the FRS in GSI, with the goal of testing prototypes of the beam tracking and identification detectors. In this chapter details on the setup and the execution of the experiment are presented.

7.1 Experimental setup

The experiment was performed during the 2022 experimental campaign at GSI as part of FAIR Phase-0. The main goal was detecting Coulomb excitations of

stable even-even nuclei. In particular ^{64}Ni (or similar) beam was to be requested however, only ^{208}Pb beam was available due to the test being scheduled in parallel (as secondary user) to another DESPEC experiment (as the main user).

After arriving at the experimental area, the primary ^{208}Pb beam at 250 MeV/u interacts with a thick β Plastic detector. To slow down the beam a mechanical structure holding degraders of different thicknesses was used. The structure could be controlled remotely, allowing for the precise selection the thickness by moving the different degraders in and out of the beam line. Micro-Channel Plate (MCP) detectors [96] were used for ion tracking and ToF measurement. After interaction with the thin secondary ^{197}Au target, located downstream of the MCPs, the beam is stopped in a $\Delta E - E$ telescope, consisting of two DSSSD detectors. Centered around the target, two DEGAS HPGe detectors were used for detecting γ rays. It is important to note that the MCP detectors and the $\Delta E - E$ telescope need to be operated under high vacuum with pressure around 10^{-7} mbar. More details on this topic will be discussed when describing the individual detectors. A schematic of the test setup and vacuum chamber as well as a picture are shown in Fig. 7.2.

7.1.1 β Plastic

The β Plastic detector used in this setup is the same as already explained in Chapter 3 when discussing the DESPEC setup. A single layer made of 3 mm thick plastic material coupled to silicon photomultipliers (SiPMs) along the four sides and has the size of 8 x 24 cm^2 , corresponding to the wide configuration of the DESPEC implantation setup. The signal from this detector was used as the trigger for all other detector systems.

7.1.2 Micro-Channel Plates

Three Micro-Channel Plate (MCP) detectors [96] were to be used for the beam tracking and ToF measurement for this experiment. One was provided by the Institute for Nuclear Physics of the University of Cologne and two were from the DESPEC group at GSI. The latter two needed to be refurbished before the experiment because the electrostatic mirrors were damaged during transportation.

As previously mentioned, in order to avoid deterioration of the beam quality causing additional straggling after the degrader, a minimal amount of matter needs to be put in the beam path. Therefore the tracking detectors were placed at a 90° angle and coupled to a thin secondary electron emission foil and an electrostatic mirror (see Fig. 7.3 (a) and (b)). The electrostatic mirrors of the GSI detectors consist of a mechanical structure and a 20 μm thick gold-plated tungsten wire winded around it (see Fig. 7.3 (c)). The beam particles hit the foil

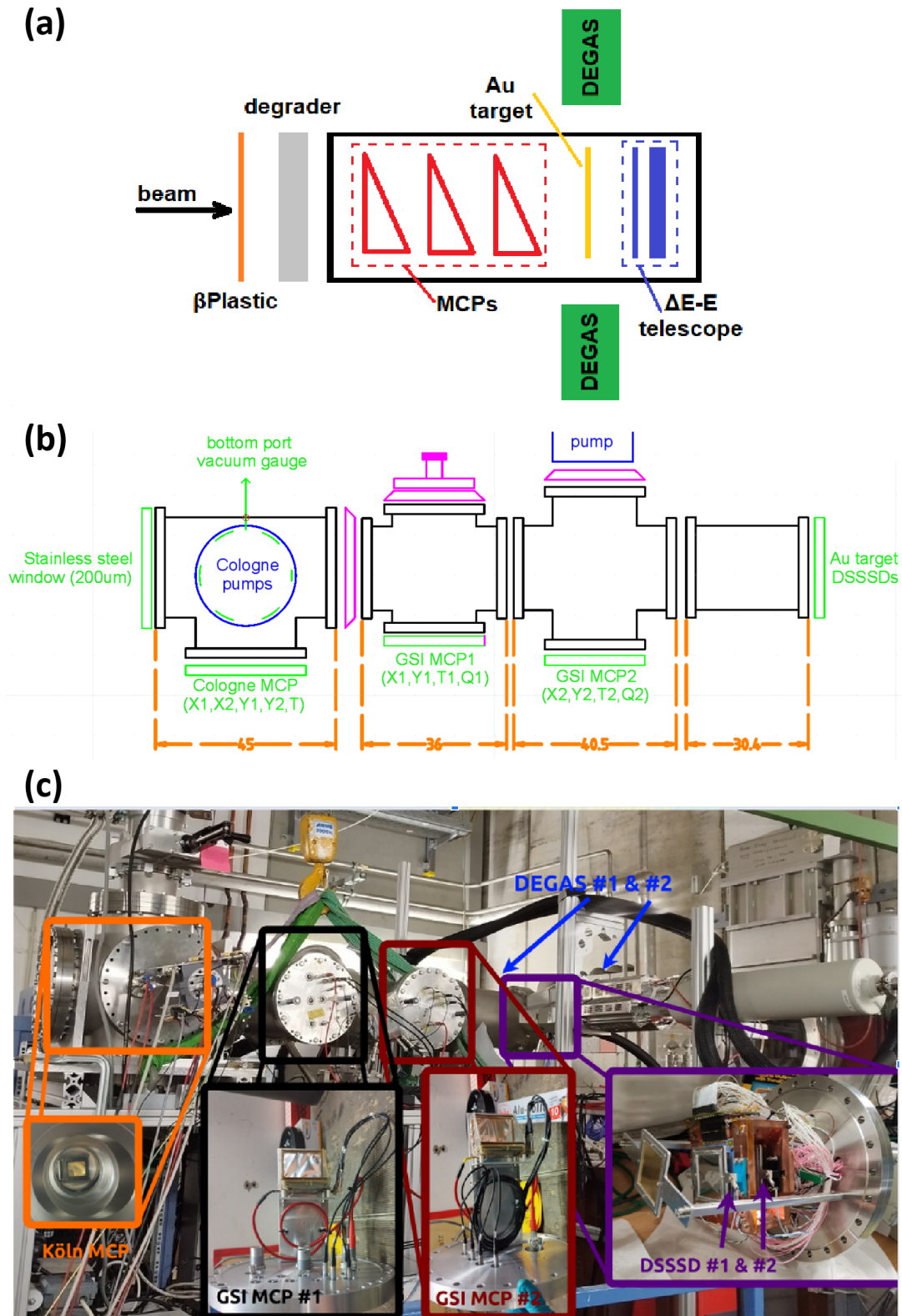


Figure 7.2: (a) Schematic drawing of the SDB setup. (b) Technical drawing of the vacuum chamber, indicating where the detectors will be mounted. (c) Picture of the experimental vacuum chamber and the individual detectors.

and produce electrons, which are accelerated by applying negative voltage to the foil. The accelerated electrons travel freely through the volume restricted by the wires of the electrostatic mirror and are deflected towards the MCP surface. This is achieved by keeping a negative voltage gradient between the triangular grids and the binding wires kept at a 45° angle. The electrons produced in the foil travel an equal distance regardless of the vertical position and arrive at the MCP surface at approximately the same time. Each MCP is made of micro-meter in diameter glass surface and each channel acts as an electron multiplier. Secondary electrons are produced by the collision of the electrons with the walls of the channels and are collected at the ends. The transition time of electrons through the channels is in the order of 0.1 ns, which makes these detectors suitable for fast timing measurements. A cross section of the MCP surface is shown in Fig. 7.3 (d).

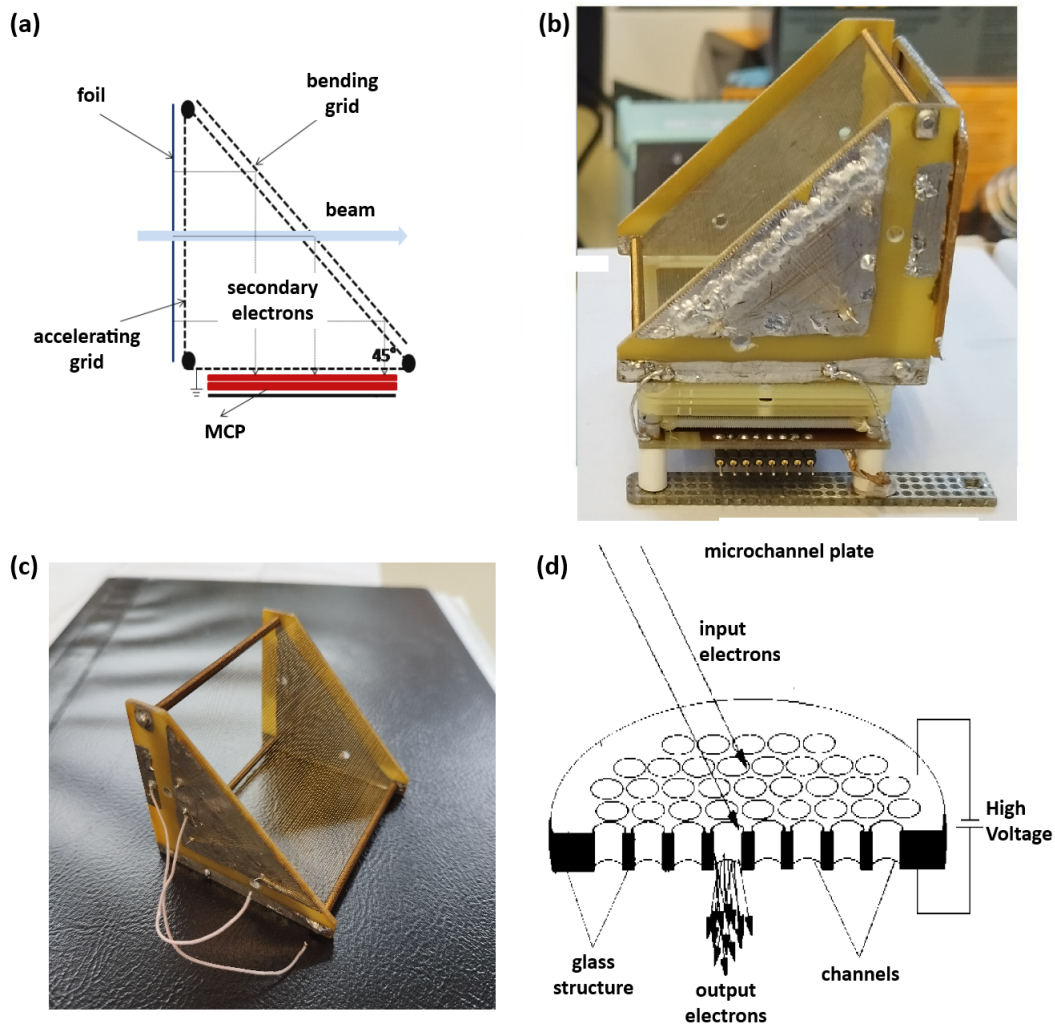


Figure 7.3: (a) Schematic of the secondary electron emission MCP detector with electrostatic mirror [76] (b) Picture of one of the GSI MCP detectors. (c) Picture of the repaired electrostatic mirror. (d) Cross section of the surface of an MCP with the channels acting as secondary electron multipliers [76].

As previously mentioned, MCP detectors need to be operated under vacuum. The electrons must travel from the top to the bottom of the channels without interference from gas molecules in order to ensure accurate detection. Operating MCPs in air poses the risk of ionization of gas molecules within the channels, which can lead to discharges (sparks) between the MCP and adjacent components. Vacuum minimizes gas interactions, ensuring efficient electron multiplication. In addition, high voltage feedthroughs and other components are sensitive to mechanical shock, which emphasizes the need for a vacuum environment even more.

The position of interaction on the MCP was obtained using a delay line readout. The electrons exiting the MCP are accelerated to a specific energy (usually around 500 eV). They travel a distance before reaching a grid, where the charge is collected by the set of conducting wires perpendicular to each other, corresponding to the X and Y directions. The electric signal induced by the charge hitting the wires travels along each delay line. The time it takes for the signals to reach the ends of the delay lines is measured and the difference in arrival times is directly proportional to the position where the charge hit the anode. The exact interaction position (X,Y) can be determined by analyzing the time differences for both X and Y delay lines. Additionally, the time of interaction can be determined by summing the arrival times at both ends of the delay line.

The interaction positions obtained from the MCP detectors can be used to reconstruct the trajectory of the particles after the slowing down process in the degrader. Additionally, the timing information is to be used for a ToF measurement, which will help determine velocity of the ions. Knowing the velocity before and after the secondary Au target can help with the determination of the reaction kinematics.

7.1.3 ΔE -E telescope

The ΔE -E telescope, intended to be used as an active stopper, is located downstream of the secondary Au target and consists of two DSSSDs, each with 16 x 16 strips. Both are equipped with secondary electron shields in order to prevent the influence of the electrons, coming from the target and the upstream DSSSD (see Fig. 7.4). The upstream detector (first after the target) has a thicknesses of 20 μm , while the downstream one is much thicker than with 300 μm . This difference in thickness between the two layers allows for energy loss ΔE to be measured in the first DSSSD and the total kinetic energy E to be determined in the second, where the ions of interest are stopped. Details on the working principle of DSSSDs can be found in Chapter 3 Section 3.4.1, when discussing

the AIDA active stopper.

The ΔE -E telescope is intended to be used for ion identification and tracking. However, in order to unambiguously identify a given nucleus, its charge (Z) and mass (m) need to be known. In Chapter 3 (when introducing MUSIC detectors) it was established that the Bethe-Bloch formula provides a connection between the stopping power (or energy loss in a material) and the atomic number Z . Following this, by measuring the energy loss ΔE one essentially gains information on the charge of the nucleus of interest. Similarly, the mass of an ion can be determined by measuring its velocity (using the ToF from the MCP detectors) and total kinetic energy E deposited in the second DSSSD.

Due to the angle straggling, coming from both the slowing-down process and the interaction of the beam with the target, Doppler correction is required for the γ rays emitted in flight after Coulomb excitation. Therefore, using the position sensitivity of the DSSSD detectors to track the ions emerging from the secondary target, their trajectory can be determined. The velocity information can once again be provided via a ToF measurement by the MCP detectors located upstream of the target and the dE -E telescope.

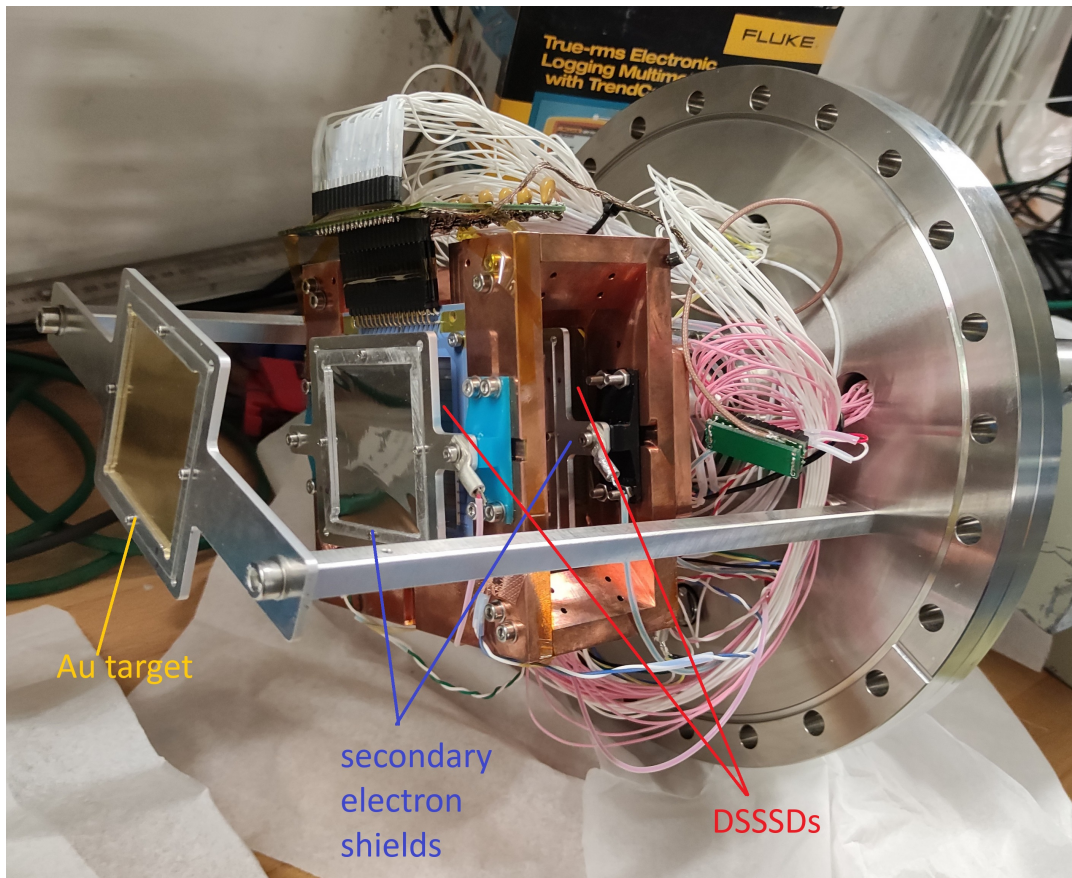


Figure 7.4: Picture of the ΔE -E telescope, consisting of two DSSSDs and covered by secondary electron shields.

In order to reduce noise and improve the detector resolution, the DSSSDs were mounted on a copper frame (see Fig. 7.4) and cooled down to around -25°C using an electric Ortec-X-Cooler.

7.1.4 DEGAS

For detecting γ rays, arising from the decay of populated excited states during the test experiment, two three-fold DEspec Germanium Array Spectrometer (DEGAS) detectors [97, 98] were employed. Each cluster detector comprises three encapsulated high-purity germanium crystals in a common cryostat (see Fig. 7.5). It is well known that HPGe spectrometers have a relatively high cross section for Compton scattering. Therefore, in an attempt to filter out the Compton continuum different techniques have been developed such as using anti-Compton-shielding detectors or γ -ray tracking in segmented HPGe detectors [99].

To shield the back side of the DEGAS detectors Bismuth Germanium Oxide (BGO) scintillation detectors are employed (see Fig. 7.5). Due to its higher density and attenuation coefficient for photoelectric absorption in comparison to germanium, BGO has better γ -ray detection efficiency, making it an ideal material for absorbing γ rays, scattering out of a HPGe detector. Additionally, by using BGO data as a veto (in anti-coincidence with a HPGe detector) many incomplete events can be rejected, which would otherwise form the Compton continuum [100]. Due to the fact that the BGOs are in the process of being assembled and tested, only one HPGe detector was equipped with back-catchers at the time of the experiment.

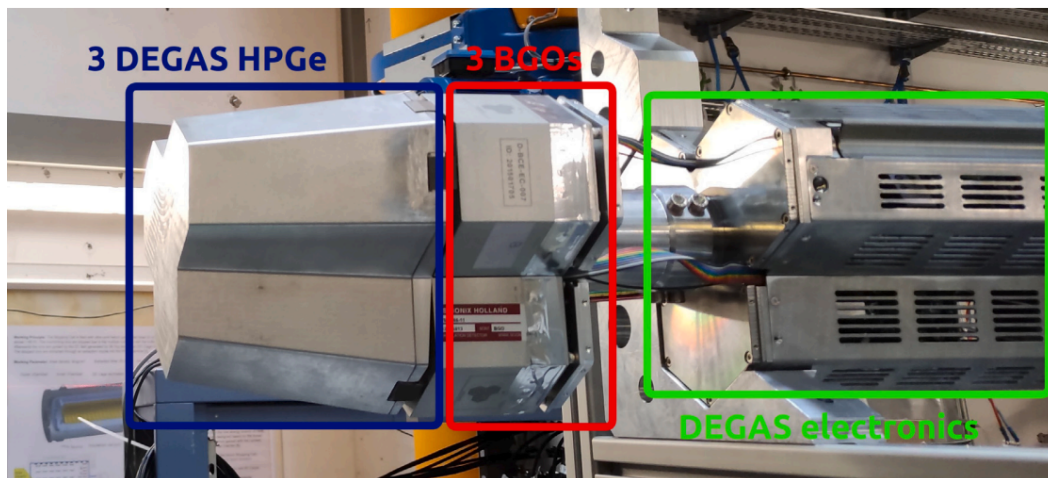


Figure 7.5: Picture of a DEGAS cluster, consisting of three HPGe crystals and three BGO back-catchers behind. Taken from Ref. [100]

7.1.5 Data acquisition

In contrast to the previously covered DESPEC experiment, where every detector system has its own data acquisition based on the MultiBranch System (MBS) [52], for the currently discussed test experiment a single MBS DAQ was used for all detectors. This was primarily due to the fact that except for DEGAS and the BGOs, which were readout via FEBEX digitizers, the rest of the detector systems used the standard VME analog-to-digital (ADC) and time-to-digital (TDC) converters.

The FEBEX and VME systems have their own internal time and if one wants to correlate events from the two an external signal is needed to serve as a reference. In the DESPEC setup this role was played by the White Rabbit timing system, which however was not available in the hall, where the SDB test experiment was performed. In an attempt to solve this problem, the β Plastic trigger was fed to the two electronics systems.

7.2 Preparation and execution of the experiment

In the proposal for the SDB test experiment 15 parasitic or 6 regular shifts of ^{64}Ni beam (or similar) were requested. The experiment was finally scheduled to run for 4 days simultaneously, as a parasitic experiment, alongside a primary DESPEC experiment. Due to this scheduling the only available beam was ^{208}Pb . Additionally, as a consequence of a number of issues (lack of manpower, vacuum leaks, problems with the DSSSD flange, debugging of the online monitoring code, etc.) only one shift could be utilized.

Nevertheless, experimental data was collected for different degrader thicknesses, using the local MBS DAQ (in list mode). Additionally, traces of some detector signals were recorded using oscilloscopes.

7.3 Data analysis and results

Review of the oscilloscope data indicates that very few coincidences are observed between the MCPs, where the β Plastic trigger signal is also present. Fig. 7.6 shows a coincidence event, where all three MCP detectors were triggered, but the β Plastic accepted trigger is missing. It is currently unclear why this data is dominated by such events, however the oscilloscope traces are but a fraction of the data saved using the MBS DAQ. Nonetheless, in case this trend preserves also for the list mode data, a lot of coincidence events between MCPs could be lost due to the missing β Plastic signal, which opens the collection window.

The MBS data is currently under analysis and will be utilized to enhance the SDB setup. Efforts are already underway to improve the SDB detectors and data acquisition system in preparation for future experiments.

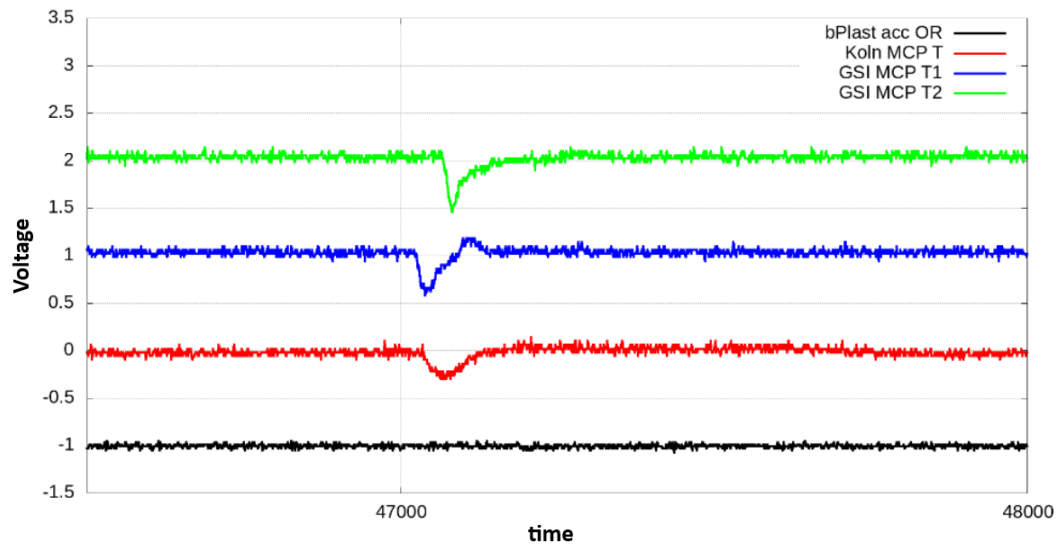


Figure 7.6: Coincidences between detectors seen in the oscilloscope data (figure, courtesy of G. Kósir)

Chapter 8

Conclusion

In this thesis results from the first experiment of the DESPEC campaign are presented. The fast timing technique was successfully implemented and used to remeasure the lifetimes the $I^\pi = 6^+, 4^+$ and 2^+ yrast states in the ^{96}Pd , validating the analysis method. The half-life and transition rates of the intermediate $I^\pi = 8^+$ and 6^+ states in ^{94}Pd were measured for the first time. A range of interactions and model spaces were employed to reproduce the level energies and experimental $B(E2)$ values, with the LSSM approach showing the best agreement. This model suggests that there is no development of deformation for Pd isotopes, which is predicted along the $N = Z$ line based on a parallel potential energy surface analysis. Based on this conclusion, the $T = 0$ contribution of the pn interaction emerges as the dominant factor in the transition strengths of the 8^+ seniority remnant state and the 14^+ isomeric state. The results and discussion related to the nuclear structure of ^{94}Pd in this thesis, were published in Ref. [101].

Additionally, this work reports on the preparation and execution of an experiment aimed at testing detector prototypes for the future HISPEC-10 campaign at FAIR.

Bibliography

- [1] M. G. Mayer, *On Closed Shells in Nuclei. II*, Phys. Rev. **75**, 1969 (1949).
- [2] O. Haxel, J. H. D. Jansen and H. E. Suess, *On the “Magic Numbers“ in Nuclear Structure*, Phys. Rev. **75**, 1766 (1949).
- [3] T. Faestermann, M. Górska and H. Grawe, *The structure of ^{100}Sn and neighbouring nuclei*, Prog. Part. Nucl. Phys. **69**, 85 (2013).
- [4] M. Górska, *Trends in the Structure of Nuclei near ^{100}Sn* , Physics **4**, 364 (2022).
- [5] F. J. D. Serduke, R. D. Lawson and D. H. Gloeckner, *Shell-model study of the $N = 49$ isotones*, Nucl. Phys. A **256**, 45 (1976).
- [6] R. Gross and A. Frenkel, *Effective interaction of protons and neutrons in the $2p_{1/2}$ - $1g_{9/2}$ subshells*, Nucl. Phys. A **267**, 85 (1976).
- [7] J. Blomqvist and L. Rydström, *Shell Model Description of the $N = 50$ Isotones Between ^{88}Sr and ^{100}Sn* , Phys. Scr. **31**, 31 (1985).
- [8] I. P. Johnstone and L. D. Skouras, *Charge-independent effective interactions for shell-model studies in the $0g_{9/2}$ - $1p_{1/2}$ space*, Eur. Phys. J. A **11**, 125 (2001).
- [9] A. F. Lisetskiy, B. A. Brown, M. Horoi and H. Grawe, *New $T = 1$ effective interactions for the $f_{5/2}$ $p_{3/2}$ $p_{1/2}$ $g_{9/2}$ model space: Implications for valence-mirror symmetry and seniority isomers*, Phys. Rev. C **70**, 044314 (2004).
- [10] M. Hjorth-Jensen, T. T. S. Kuo and E. Osnes, *Realistic effective interactions for nuclear systems*, Phys. Rep. **261**, 125 (1995).
- [11] M. Honma, T. Otsuka, T. Mizusaki and M. Hjorth-Jensen, *New effective interaction for f_5pg_9 -shell nuclei*, Phys. Rev. C **80**, 064323 (2009).
- [12] B. S. Nara Singh *et al.*, *16^+ Spin-Gap Isomer in ^{96}Cd* , Phys. Rev. Lett. **107**, 172502 (2011).

-
- [13] A. Escuderos and L. Zamick, *Seniority conservation and seniority violation in the $g_{9/2}$ shell*, Phys. Rev. C **73**, 044302 (2006).
- [14] P. Van Isacker and S. Heinze, *Partial Conservation of Seniority and Nuclear Isomerism*, Phys. Rev. Lett. **100**, 052501 (2008).
- [15] C. Qi, *Partial conservation of seniority in the $j = 9/2$ shell: Analytic and numerical studies*, Phys. Rev. C **83**, 014307 (2011).
- [16] L. Zamick and A. Escuderos, *Single j -shell studies of cross-conjugate nuclei and isomerism: $(2j - 1)$ rule*, Nucl. Phys. A **889**, 8 (2012).
- [17] C. Qi, *Partial conservation of seniority and its unexpected influence on $E2$ transitions in $g_{9/2}$ nuclei*, Phys. Lett. B **773**, 616 (2017).
- [18] H. Mach *et al.*, *Ultrafast-timing lifetime measurements in ^{94}Ru and ^{96}Pd : Breakdown of the seniority scheme in $N = 50$ isotones*, Phys. Rev. C **95**, 014313 (2017).
- [19] Y. Qian and C. Qi, *Partial seniority conservation and solvability of single- j systems*, Phys. Rev. C **98**, 061303 (2018).
- [20] B. Das *et al.*, *Nature of seniority symmetry breaking in the semimagic nucleus ^{94}Ru* , Phys. Rev. C **105**, L031304 (2022).
- [21] B. Das *et al.*, *Broken seniority symmetry in the semimagic proton mid-shell nucleus ^{95}Rh* , Phys. Rev. Res. **6**, L022038 (2024).
- [22] L. Zamick, *Gaps in nuclear spectra as traces of seniority changes in systems of both neutrons and protons*, Phys. Rev. C **93**, 034327 (2016).
- [23] A. Blazhev *et al.*, *Observation of a core-excited $E4$ isomer in ^{98}Cd* , Phys. Rev. C **69**, 064304 (2004).
- [24] A. Blazhev *et al.*, *High-energy excited states in ^{98}Cd* , J. Phys.: Conf. Ser. **205**, 012035 (2010).
- [25] P. Boutachkov *et al.*, *High-spin isomers in ^{96}Ag : Excitations across the $Z = 38$ and $Z = 50$, $N = 50$ closed shells*, Phys. Rev. C **84**, 044311 (2011).
- [26] B. Cederwall *et al.*, *Evidence for a spin-aligned neutron-proton paired phase from the level structure of ^{92}Pd* , Nature (London) **469**, 68 (2011).
- [27] P. J. Davies *et al.*, *The role of core excitations in the structure and decay of the 16^+ spin-gap isomer in ^{96}Cd* , Phys. Lett. B **767**, 474 (2017).

- [28] P. J. Davies *et al.*, *Toward the limit of nuclear binding on the $N = Z$ line: Spectroscopy of ^{96}Cd* , Phys. Rev. C **99**, 021302(R) (2019).
- [29] G. Lorusso *et al.*, *Half-lives of ground and isomeric states in ^{97}Cd and the astrophysical origin of ^{96}Ru* , Phys. Lett. B **699**, 141 (2011).
- [30] M. La Commara *et al.*, *Beta decay of medium and high spin isomers in ^{94}Ag* , Nucl. Phys. A **708**, 167 (2002).
- [31] C. Plettner *et al.*, *On the β -decaying (21^+) spin gap isomer in ^{94}Ag* , Nucl. Phys. A **733**, 20 (2004).
- [32] J. Park *et al.*, *Properties of γ -decaying isomers and isomeric ratios in the ^{100}Sn region*, Phys. Rev. C **96**, 044311 (2017).
- [33] J. Park *et al.*, *New and comprehensive β - and βp -decay spectroscopy results in the vicinity of ^{100}Sn* , Phys. Rev. C **99**, 034313 (2019).
- [34] G. Häfner *et al.*, *Properties of γ -decaying isomers in the ^{100}Sn region populated in fragmentation of a ^{124}Xe beam*, Phys. Rev. C **100**, 024302 (2019).
- [35] N. Mărginean *et al.*, *Delayed alignments in the $N = Z$ nuclei ^{84}Mo and ^{88}Ru* , Phys. Rev. C **65**, 051303 (2002).
- [36] B. Cederwall *et al.*, *Isospin Properties of Nuclear Pair Correlations from the Level Structure of the Self-Conjugate Nucleus ^{88}Ru* , Phys. Rev. Lett. **124**, 062501 (2020).
- [37] S. Zerguine and P. Van Isacker, *Spin-aligned neutron-proton pairs in $N = Z$ nuclei*, Phys. Rev. C **83**, 064314 (2011).
- [38] Z. X. Xu, C. Qi, J. Blomqvist, R. J. Liotta and R. Wyss, *Multistep shell model description of spin-aligned neutron-proton pair coupling*, Nucl. Phys. A **877**, 51 (2012).
- [39] C. Qi, J. Blomqvist, T. Bäck, B. Cederwall, A. Johnson, R. J. Liotta and R. Wyss, *Spin-aligned neutron-proton pair mode in atomic nuclei*, Phys. Rev. C **84**, 021301 (2011).
- [40] P. Van Isacker, *Neutron-proton pairs in nuclei*, Int. Journal Mod. Phys. E **22**, 1330028 (2013).
- [41] A. P. Zuker, A. Poves, F. Nowacki and S. M. Lenzi, *Nilsson- $SU3$ self-consistency in heavy $N = Z$ nuclei*, Phys. Rev. C **92**, 024320 (2015).

-
- [42] M. Górska *et al.*, *Proton-neutron interaction at $N \cong Z$ — First observation of the $T_z = 1$ nucleus ${}^{94}_{46}\text{Pd}_{48}$ in-beam*, Z. Phys., A At. nucl. **353**, 233 (1995).
- [43] R. Grzywacz *et al.*, *New μs isomers in $T_z=1$ nuclei produced in the ${}^{112}\text{Sn}(63A \text{ MeV})+{}^{\text{nat}}\text{Ni}$ reaction*, Phys. Rev. C **55**, 1126 (1997).
- [44] T. S. Brock and others (RISING Collaboration), *Observation of a new high-spin isomer in ${}^{94}\text{Pd}$* , Phys. Rev. C **82**, 061309 (2010).
- [45] S. Frauendorf and A. O. Macchiavelli, *Overview of neutron-proton pairing*, Prog. Part. Nucl. Phys. **78**, 24 (2014).
- [46] A. S. Mare and A. Petrovici, *Shape coexistence and isomeric states in ${}^{94}\text{Pd}$ within a beyond-mean-field approach*, Phys. Rev. C **106**, 054306 (2022).
- [47] N. Bohr, *On the Constitution of Atoms and Molecules, Parts I, II, III*, Philos. Mag. **26**, pp. 1, 476, 857 (1913).
- [48] K. S. Krane, *Introductory Nuclear Physics* (John Wiley & Sons, 1988).
- [49] P. J. Brussaard and P. W. M. Glaudemans, *Shell-Model applications in nuclear spectroscopy* (North-Holland Publishing Company, 1977).
- [50] K. Heyde, *The Nuclear Shell Model* (Springer, Berlin, 1994).
- [51] K. A. Brückner, *Two-Body Forces and Nuclear Saturation. III. Details of the Structure of the Nucleus*, Phys. Rev. **97**, 1353 (1955).
- [52] J.-M. Régis *et al.*, *The generalized centroid difference method for picosecond sensitive determination of lifetimes of nuclear excited states using large fast-timing arrays*, Nucl. Instrum. Methods Phys. Res. A **726**, 191 (2013).
- [53] J.-M. Régis *et al.*, *The Generalized Centroid Difference method for lifetime measurements via $\gamma - \gamma$ coincidences using large fast-timing arrays*, EPJ Web of Conferences **93**, 01013 (2015).
- [54] H. Geissel *et al.*, *The GSI projectile fragment separator (FRS): a versatile magnetic system for relativistic heavy ions*, Nucl. Instrum. Methods Phys. Res. B **70**, 286 (1992).
- [55] *GSI Helmholtzzentrum für Schwerionenforschung GmbH* ().
- [56] H. Geissel *et al.*, *The Super-FRS project at GSI*, Nucl. Instrum. Methods Phys. Res. B **204**, 71 (2003).

- [57] P. Spiller and G. Franchetti, *The FAIR accelerator project at GSI*, Nucl. Instrum. Methods Phys. Res. A **561**, 305 (2006).
- [58] *UNILAC*.
- [59] *Heavy Ion Synchrotron SIS18*.
- [60] G. Münzenberg, *The separation techniques for secondary beams*, Nucl. Instrum. Methods Phys. Res. B **70**, 265 (1992).
- [61] A. B. Garnsworthy *et al.*, *Isomeric states in neutron-deficient $A \sim 80$ – 90 nuclei populated in the fragmentation of ^{107}Ag* , Phys. Rev. C **80**, 064303 (2009).
- [62] A. K. Mistry *et al.*, *The DESPEC setup for GSI and FAIR*, Nucl. Instrum. Methods Phys. Res. A **1033**, 166662 (2022).
- [63] O. Hall *et al.*, *The Advanced Implantation Detector Array (AIDA)*, Nucl. Instrum. Methods Phys. Res. A **1050**, 168166 (2023).
- [64] A. Goasduff *et al.*, *The GALILEO γ -ray array at the Legnaro National Laboratories*, Nucl. Instrum. Methods Phys. Res. A **1015**, 165753 (2021).
- [65] P. R. John *et al.*, *Assembly of 8 Galileo TC at Institut für Kernphysik TU Darmstadt for the DESPEC Campaign* (2020).
- [66] M. Rudigier *et al.*, *FATIMA - FAst TIMing Array for DESPEC at FAIR*, Nucl. Instrum. Methods Phys. Res. A **969**, 163967 (2020).
- [67] *GSI accelerator facility* ().
- [68] J.-J. Gaimard and K. H. Schmidt, *A reexamination of the abrasion-ablation model for the description of the nuclear fragmentation reaction*, Nucl. Phys. A **531**, 709 (1991).
- [69] *FRagment Separator (FRS)* ().
- [70] *FRS ion optics* ().
- [71] H. Stelzer, *Multiwire chambers with a two-stage gas amplification*, Nucl. Instrum. Methods Phys. Res. A **310**, 103 (1991).
- [72] *MultiWire Proportional Counters (MWPCs)*.
- [73] A. Stolz and R. Schneider, *Technical Manual Ionisation Chamber MU-SIC80* (2000).

- [74] O. Frisch, British Atomic Energy Report **BR-49** (1944).
- [75] *Plastic scintillators for ToF measurement*.
- [76] F. Naqvi, *Probing the collectivity in neutron-rich Cd isotopes via γ -ray spectroscopy* (2011), PhD thesis.
- [77] D. Braga *et al.*, *AIDA: A 16-channel amplifier ASIC to read out the advanced implantation detector array for experiments in nuclear decay spectroscopy*, 2009 IEEE Nuclear Science Symposium Conference Record (NSS/MIC) , 1924 (2009).
- [78] A. Banerjee *et al.*, *Analog front-end for FPGA-based readout electronics for scintillation detectors*, Nucl. Instrum. Methods Phys. Res. A **1028**, 166357 (2022).
- [79] *GSI Multi Branch System (MBS)*.
- [80] *General Machine Timing System at GSI and FAIR*.
- [81] *unpack and check every single bit (ucesb)*.
- [82] J.-M. Régis *et al.*, *Abrupt shape transition at neutron number $N = 60$: $B(E2)$ values in $^{94,96,98}\text{Sr}$ from fast $\gamma - \gamma$ timing*, Phys. Rev. C **95**, 054319 (2017).
- [83] A. Yaneva, S. Jazrawi, B. Das, M. Mikolajczuk, M. Górska, P. H. Regan, C. B., J. Jolie *et al.*, *Fast-timing Measurement in ^{96}Pd : Improved Accuracy for the Lifetime of the (4_1^+) State*, Acta Phys. Pol. B Proc. Suppl. **16**, 4 (2023).
- [84] M. Górska, P. Regan, B. Cederwall, J. Jolie *et al.*, *Structure of the heaviest $N=Z$ nuclei: Seniority Transitions and EM Transition Rates in ^{94}Pd* , GSI (2019).
- [85] H. Grawe *et al.*, *The (6^+) isomer in ^{102}Sn revisited: Neutron and proton effective charges close to the double shell closure*, Phys. Lett. B **820**, 136591 (2021).
- [86] D. D. Dao and F. Nowacki, *Nuclear structure within a discrete nonorthogonal shell model approach: New frontiers*, Phys. Rev. C **105**, 054314 (2022).
- [87] M. Rocchini *et al.*, *First Evidence of Axial Shape Asymmetry and Configuration Coexistence in ^{74}Zn : Suggestion for a Northern Extension of the $N = 40$ Island of Inversion*, Phys. Rev. Lett. **130**, 122502 (2023).

- [88] R. Machleidt, *High-precision, charge-dependent Bonn nucleon-nucleon potential*, Phys. Rev. C **63**, 024001 (2001).
- [89] L. Coraggio, A. Covello, A. Gargano and N. Itaco, *$g_{9/2}$ nuclei and neutron-proton interaction*, Phys. Rev. C **85**, 034335 (2012).
- [90] Y. Blumenfeld, T. Nilsson and P. Van Duppen, *Facilities and methods for radioactive ion beam production*, Phys. Scr. **2013**, 014023 (2013).
- [91] *FAIR Facility for Antiproton and Ion Research GmbH*.
- [92] T. Glasmacher, *Intermediate-energy Coulomb excitation*, Nucl. Phys. A **693**, 90 (2001).
- [93] *Technical Report for the Design, Construction and Commissioning of the HISPEC/DESPEC Beam Line, Infrastructure and Tracking Detectors*.
- [94] F. Naqvi, P. Boutachkov, M. Górska *et al.*, *Development of slowed down beams at the fragment separator for FAIR*, Acta Phys. Pol. B **42**, 725 (2011).
- [95] N. Iwasa, H. Geissel, G. Münzenberg, C. Scheidenberger, T. Schwab and H. Wollnik, *MOCADI, a universal Monte Carlo code for the transport of heavy ions through matter within ion-optical systems*, Nucl. Instrum. Methods Phys. Res. B **126**, 284 (1997).
- [96] G. Montagnoli *et al.*, *The large-area micro-channel plate entrance detector of the heavy-ion magnetic spectrometer PRISMA*, Nucl. Instrum. Methods Phys. Res. A **547**, 455 (2005).
- [97] *Technical Report for the Design, Construction and Commissioning of the DESPEC Germanium Array Spectrometer DEGAS*.
- [98] G. Li, C. Lizarazo, J. Gerl, I. Kojouharov, H. Schaffner, M. Górska, N. Pietralla, S. Saha, M. L. Liu and J. G. Wang, *Simulated characteristics of the DEGAS γ -detector array*, Nucl. Instrum. Methods Phys. Res. A **890**, 148 (2018).
- [99] S. Akkoyun, A. Algora, B. Alikhani, F. Ameil, G. de Angelis *et al.*, *AGATA - Advanced GAMMA Tracking Array*, Nucl. Instrum. Methods Phys. Res. A **668**, 26 (2012).
- [100] G. Kosir, J. Vesic, I. Kojouharov, H. Schaffner, J. Gerl, N. Kurz, M. Reese and M. Vencelj, *BGO active shield for DEGAS*, Nucl. Instrum. Methods Phys. Res. A **1062**, 169157 (2024).

- [101] A. Yaneva, S. Jazrawi, M. Mikolajczuk, M. Górska, P. H. Regan, B. Das *et al.*, *The shape of the $T_z = +1$ nucleus ^{94}Pd and the role of proton-neutron interactions on the structure of its excited states*, Phys. Lett. B **855**, 138805 (2024).

List of Publications

Publications in refereed journals

- A. Yaneva, D. Kocheva, G. Rainovski, J. Jolie, N. Pietralla, A. Blazhev, A. Dewald, M. Djongolov, C. Fransen, K. A. Gladnishki, C. Henrich, I. Homm, K. E. Ide, P. R. John, D. Kalaydjieva, V. Karayonchev, R. Kern, J. Kleemann, Th. Kröll, C. Müller-Gatermann, M. Scheck, P. Spagnoletti, M. Stoyanova, V. Werner.
Experimental evidence for low-lying quadrupole isovector excitation of ^{208}Po
Eur. Phys. J. A 56, 246 (2020).
- D. Kalaydjieva, D. Kocheva, G. Rainovski, V. Karayonchev, J. Jolie, N. Pietralla, M. Beckers, A. Blazhev, A. Dewald, M. Djongolov, A. Esmaylzadeh, C. Fransen, K. A. Gladnishki, A. Goldkuhle, C. Henrich, I. Homm, K. E. Ide, P. R. John, R. Kern, J. Kleemann, T. Kröll, C. Müller-Gatermann, M. Scheck, P. Spagnoletti, M. Stoyanova, K. Stoychev, V. Werner, A. Yaneva, S. S. Dimitrova, G. De Gregorio, H. Naïdja and A. Gargano.
Microscopic structure of the one-phonon 2^+ states of ^{208}Po .
Phys. Rev. C 104 (2021), 024311.
- B. Das, B. Cederwall, C. Qi, M. Górska, P. H. Regan, Ö. Aktas, H. M. Albers, A. Banerjee, M. M. R. Chishti, J. Gerl, N. Hubbard, S. Jazrawi, J. Jolie, A. K. Mistry, M. Polettini, A. Yaneva, S. Alhomaidhi, J. Zhao, T. Arici, S. Bagchi, G. Benzoni, P. Boutachkov, T. Davinson, T. Dickel, E. Haettner, O. Hall, C. Hornung, J. P. Hucka, P. R. John, I. Kojouharov, R. Knöbel, D. Kostyleva, N. Kuzminchuk, I. Mukha, W. R. Plass, B. S. Nara Singh, J. Vasiljević, S. Pietri, Z. Podolyák, M. Rudigier, H. Rösch, E. Sahin, H. Schaffner, C. Scheidenberger, F. Schirru, A. Sharma, R. Shearman, Y. Tanaka, J. Vesić, H. Weick, H. J. Wollersheim, U. Ahmed, A. Algora, C. Appleton, J. Benito, A. Blazhev, A. Bracco, A. M. Bruce, M. Brunet, R. Canavan, A. Esmaylzadeh, L. M. Fraile, G. Häfner, H. Heggen, D. Kahl, V. Karayonchev, R. Kern, A. Korgul, G. Kosir, N. Kurz, R. Lozeva, M.

Mikolajczuk, P. Napiralla, R. Page, C. M. Petrache, N. Pietralla, J.-M. Régis, P. Ruotsalainen, L. Sexton, V. Sanchez-Temble, M. Si, J. Vilhena, V. Werner, J. Wiederhold, W. Witt, P. J. Woods and G. Zimba.

Nature of seniority symmetry breaking in the semimagic nucleus ^{94}Ru .

Phys. Rev. C 105 (2022), L031304.

- A. Mistry, H. Albers, T. Arici, A. Banerjee, G. Benzoni, B. Cederwall, J. Gerl, M. Górska, O. Hall, N. Hubbard, I. Kojouharov, J. Jolie, T. Martinez, Z. Podolyák, P. Regan, J. Tain, A. Tarifeno-Saldivia, H. Schaffner, V. Werner, G. Ağgez, J. Agramunt, U. Ahmed, Ö. Aktas, V. Alcayne, A. Algora, S. Alhomaïdhi, F. Amjad, C. Appleton, M. Armstrong, M. Balogh, K. Banerjee, P. Bednarczyk, J. Benito, C. Bhattacharya, P. Black, A. Blazhev, S. Bottoni, P. Boutachkov, A. Bracco, A. Bruce, M. Brunet, C. Bruno, I. Burrows, F. Calvino, R. Canavan, D. Cano-Ott, M. Chishti, P. Coleman-Smith, M. Cortés, G. Cortes, F. Crespi, B. Das, T. Davinson, A. De Blas, T. Dickel, M. Doncel, A. Ertoprak, A. Esmaylzadeh, B. Fornal, L. Fraile, F. Galtarossa, A. Gottardo, V. Guadilla, J. Ha, E. Haettner, G. Häfner, H. Heggen, P. Herrmann, C. Hornung, S. Jazrawi, P. John, A. Jokinen, C. Jones, D. Kahl, V. Karayonchev, E. Kazantseva, R. Kern, L. Knafla, R. Knöbel, P. Koseoglou, G. Kosir, D. Kostyleva, N. Kurz, N. Kuzminchuk, M. Labiche, J. Lawson, I. Lazarus, S. Lenzi, S. Leoni, M. Llanos-Expósito, R. Lozeva, A. Maj, J. Meena, E. Mendoza, R. Menegazzo, D. Mengoni, T. Mertzimekis, M. Mikolajczuk, B. Million, N. Mont-Geli, A. Morales, P. Morral, I. Mukha, J. Murias, E. Nacher, P. Napiralla, D. Napoli, B. Nara-Singh, D. O'Donnell, S. Orrigo, R. Page, R. Palit, M. Pallas, J. Pellumaj, S. Pelonis, H. Pentilla, A. Pérez de Rada, R. Pérez-Vidal, C. Petrache, N. Pietralla, S. Pietri, S. Pigliapoco, J. Plaza, M. Polettini, C. Porzio, V. Pucknell, F. Recchia, P. Reiter, K. Rezyunkina, S. Rinta-Antila, E. Rocco, H. Rösch, P. Roy, B. Rubio, M. Rudigier, P. Ruotsalainen, S. Saha, E. Şahin, C. Scheidenberger, D. Seddon, L. Sexton, A. Sharma, M. Si, J. Simpson, A. Smith, R. Smith, P. Söderström, A. Sood, A. Soylu, Y. Tanaka, J. Valiente-Dobón, P. Vasileiou, J. Vasiljevic, J. Vesic, D. Villamarin, H. Wick, M. Wiebusch, J. Wiederhold, O. Wieland, H. Wollersheim, P. Woods, A. Yaneva, I. Zanon, G. Zhang, J. Zhao, R. Zidarova, G. Zimba and A. Zyriliou.

The DESPEC setup for GSI and FAIR.

Nucl. Instrum. Methods Phys. Res. A 1033 (2022), 166662.

- M. M. R. Chishti, S. Jazrawi, R. Shearman, P. H. Regan, Zs. Podolyák, S. M. Collins, M. Górska, B. Cederwall, A. Yaneva, G. X. Zhang, J. Cederkall, A. Goasduff, H. M. Albers, S. Alhomaiddhi, A. Banerjee, A. M. Bruce, G. Benzoni, B. Das, T. Davinson, L. M. Fraile, J. Gerl, G. Häfner, J. Jolie, N. Hubbard, P. R. John, R. Lozeva, A. K. Mistry, B. S. Nara Singh, M. Mikolajczuk, M. Polettini, N. Pietralla, J. M. Regis, M. Rudigier, E. Sahin, A. Sharma, M. Si, J. Vesic and V. Werner
Response of the FAsT TIMing Array (FATIMA) for DESPEC at FAIR Phase-0.
Nucl. Instrum. Methods Phys. Res. A 1056 (2023), 168597.
- B. Das, B. Cederwall, C. Qi, M. Górska, P. H. Regan, Ö. Aktas, H. M. Albers, A. Banerjee, M. M. R. Chishti, J. Gerl, N. Hubbard, S. Jazrawi, J. Jolie, A. K. Mistry, F. Nowacki, M. Polettini, A. Yaneva, U. Ahmed, S. Alhomaiddhi, A. Algora, C. Appleton, T. Arici, S. Bagchi, G. Benzoni, J. Benito, A. Blazhev, P. Boutachkov, A. Bracco, A. M. Bruce, M. Brunet, R. Canavan, T. Davinson, T. Dickel, A. Esmaylzadeh, L. M. Fraile, E. Haettner, O. Hall, G. Häfner, H. Heggen, Ch. Hornung, J. P. Hucka, P. R. John, D. Kahl, V. Karayonchev, R. Kern, R. Knöbel, A. Korgul, G. Kosir, I. Kojouharov, D. Kostyleva, N. Kuzminchuk, N. Kurz, R. Liotta, R. Lozeva, M. Mikolajczuk, I. Mukha, P. Napiralla, R. Page, C. M. Petrache, N. Pietralla, S. Pietri, W. R. Plass, Zs. Podolyák, J.-M. Régis, M. Rudigier, H. Rösch, P. Ruotsalainen, E. Sahin, V. Sánchez-Tembleque, H. Schaffner, C. Scheidenberger, F. Schirru, L. Sexton, B. S. Nara Singh, A. Sharma, R. Shearman, M. Si, Y. K. Tanaka, J. Vasiljević, J. Vesić, J. Vilhena, H. Weick, H. J. Wollersheim, V. Werner, J. Wiederhold, W. Witt, P. J. Woods, G. Zimba, J. Zhao
Broken seniority symmetry in the semimagic proton mid-shell nucleus ^{95}Rh .
Phys. Rev. Res. 6, L022038 (2024)
- A. Yaneva, S. Jazrawi, M. Mikolajczuk, M. Górska, P. H. Regan, B. Das, H. M. Albers, S. Alhomaiddhi, T. Arici, A. Banerjee, G. Benzoni, B. Cederwall, M. M. R. Chishti, D. D. Dao, T. Davinson, A. Gargano, J. Gerl, O. Hall, N. Hubbard, J. Jolie, I. Kojouharov, A. K. Mistry, F. Nowacki, M. Polettini, M. Rudigier, E. Sahin, H. Schaffner, A. Sharma, M. Armstrong, H. J. Wollersheim, P. Boutachkov, T. Dickel, E. Haettner, H. Heggen, Ch. Hornung, R. Knöbel, D. Kostyleva, N. Kurz, N. Kuzminchuk, I. Mukha, S. Pietri, W. R. Plass, Zs. Podolyák, C. Scheidenberger, Y. K. Tanaka, J. Vesic, H. Weick, U. Ahmed, Ö. Aktas, A. Algora, C. Appleton, J. Benito, A. Blazhev, A.

Bracco, A. M. Bruce, M. Brunet, R. Canavan, A. Esmaylzadeh, L. M. Fraile, G. Häfner, K. P. Hucka, P. R. John, D. Kahl, V. Karayonchev, R. Kern, G. Kosir, R. Lozeva, P. Napiralla, B. S. Nara Singh, R. Page, C. M. Petrache, N. Pietralla, J.-M. Régis, H. Rösch, P. Ruotsalainen, V. Sanchez-Temble, L. Sexton, R. Shearman, M. Si, V. Werner, J. Wiederhold, K. Wimmer, W. Witt, P. Woods, G. Zimba

The shape of the $T_z = +1$ nucleus ^{94}Pd and the role of proton-neutron interactions on the structure of its excited states.

Phys. Lett. B 855, 138805 (2024)

Conference proceedings

- D. Kocheva, A. Yaneva, D. Kalaydjieva, G. Rainovski, J. Jolie, N. Pietralla, M. Beckers, A. Blazhev, L. Bussmann, M. Cappellazzo, A. Dewald, F. Diel, M. Djongolov, F. Dunkel, A. Esmaylzadeh, B. Falk, C. Fransen, J. Garbe, L. Gerhard, R.-B. Gerst, K. A. Gladnishki, A. Goldkuhle, G. Hackenberg, C. Henrich, I. Homm, K. Ide, V. Karayonchev, R. Kern, J. Kleeman, L. Knafel, L. Kornweibel, T. Kröll, M. Ley, C. Müller-Gatermann, M. Scheck, T. Schmidt, P. Spagnoletti, M. Stoyanova and V. Werner.

Lifetime measurements of the low-lying excited states of ^{208}Po .

J. Phys. Conf. Ser. 1555 (2020), 012020.

- M. Stoyanova, V. Karayonchev, G. Rainovski, J. Jolie, N. Pietralla, A. Blazhev, A. Dewald, M. Djongolov, A. Esmaylzadeh, C. Fransen, J. Garbe, L. Gerhard, K. A. Gladnishki, K. Ide, P. R. John, R. Kern, J. Kleemann, D. Kocheva, T. Kröll, C. Müller-Gatermann, J.-M. Régis, P. Spagnoletti, V. Werner and A. Yaneva.

Evolution of the structure of the 4_1^+ states in Po isotopes.

J. Phys. Conf. Ser. 1555 (2020), 012019.

- M. Polettini, S. Jazrawi, M. M. R. Chishti, A. Yaneva, B. Das, A. Banerjee, N. Hubbard, A. K. Mistry, H. M. Albers, R. Shearman, M. Górski, J. Gerl, P. H. Regan, B. Cederwall, J. Jolie, S. Alhomaidhi, T. Arici, G. Benzoni, P. Boutachkov, T. Davinson, T. Dickel, E. Haettner, O. Hall, H. Heggen, P. R. John, I. Kojouharov, N. Kurz, B. S. N. Singh, S. Pietri, Z. Podolyak, M. Rudigier, E. Sahin, H. Schaffner, C. Scheidenberger, A. Sharma, J. Vesic, H. Weick, H. J. Wollersheim, U. Ahmed, Ö. Aktas, A. Algora, C. Appleton, J. Benito, A. Blazhev, A. Bracco, A. Bruce, M. Brunet, R. Canavan, A. Esmaylzadeh, L. M. Fraile, H. Grawe, G. Häfner, D. Kahl, V. Karayonchev, R. Kern, G. Kosir, R. Lozeva, P. Napiralla, R. Page, C. M. Petrache, J.

Petrovic, N. Pietralla, J.-M. Régis, P. Ruotsalainen, L. Sexton, V. Sanchez-Temble, M. Si, J. Vilhena, V. Werner, J. Wiederhold, W. Witt, P. Woods and G. Zimba.

DESPEC Phase-0 campaign at GSI.

IL Nuovo Cimento C 044 (2021).

- S. Jazrawi, [A. Yaneva](#), M. Polettini, B. Das, P. Regan, M. Górska, B. Cederwall, J. Jolie, H. Albers, M. Chishti, A. Banerjee, N. Hubbard, A. Mistry, M. Rudigier, G. Benzoni, J. Gerl, A. Bruce, Z. Podolyák, B. Nara Singh, G. Zhang, S. Alhomaidhi, C. Appleton, T. Arici, A. Blazhev, T. Davinson, A. Esmaylzadeh, L. Fraile, G. Häfner, O. Hall, P. John, V. Karayonchev, I. Koujoharov, N. Kurz, M. Mikolajczuk, N. Pietralla, S. Pietri, J. Regis, E. Sahin, L. Sexton, H. Schaffner, C. Scheidenberger, A. Sharma, J. Vesic, H. Weick and V. Werner.

Commissioning the FAst TIMing array (FATIMA) at FAIR Phase-0: Half-lives of excited states in the N=50 isotones ^{96}Pd and ^{94}Ru . Radiat. Phys. Chem. (2022), 110234.

- M. Polettini, J. Pellumaj, G. Benzoni, J. J. Valiente-Dobón, G. Zhang, D. Mengoni, R. M. P. Vidal, D. Genna, A. Bracco, G. Aggez, U. Ahmed, Ö. Aktas, M. A. Aqueel, B. Alayed, H. M. Albers, A. Algora, S. Alhomaidhi, C. Appleton, T. Arici, M. Armstrong, K. Arnsward, M. Balogh, A. Banerjee, J. B. Garcia, A. Blazhev, S. Bottoni, P. Boutachkov, A. Bruce, C. Bruno, F. Camera, B. Cederwall, M. M. R. Chishti, M. L. Cortés, D. M. Cox, F. C. L. Crespi, B. Das, T. Davinson, G. D. Angelis, T. Dickel, M. Doncel, R. Donthi, A. Ertoprak, R. Escudeiro, A. Esmaylzadeh, L. M. Fraile, L. Gaffney, E. R. Gamba, J. Gerl, M. Górska, A. Gottardo, J. Ha, E. Haettner, O. Hall, H. Heggen, Y. Hrabar, N. Hubbard, S. Jazrawi, P. R. John, J. Jolie, C. Jones, D. Joss, D. Judson, D. Kahl, V. Karayonchev, E. Kazantseva, R. Kern, L. Knafla, I. Kojouharov, A. Korgul, W. Korten, P. Koseoglou, G. Kosir, D. Kostyleva, T. Kurtukian-Nieto, N. Kurz, N. Kuzminchuk, M. Labiche, S. Lenzi, S. Leoni, M. L. Expósito, R. Lozeva, T. J. Mertzimekis, M. Mikolajczuk, B. Million, A. K. Mistry, A. Morales, I. Mukha, J. R. Murias, D. Napoli, B. S. N. Singh, D. O'Donnell, S. E. A. Orrigo, R. Page, S. Pelonis, J. Petrovic, N. Pietralla, S. Pietri, S. Pigliapoco, Z. Podolyak, C. Porzio, B. Q. Arnes, F. Recchia, P. H. Regan, J.-M. Régis, P. Reiter, K. Rezynekina, P. Roy, M. Rudigier, P. Ruotsalainen, E. Sahin, L. G. Sarmiento, M.-M. Satrazani, H. Schaffner, C. Scheidenberger, L. Sexton, A. Sharma, J. Smallcombe, P.-A. Söderström, A. Sood, P. Vasileiou, J. Vesic, J. Vilhena, L. Waring, H. Weick, V. Werner, J. Wiederhold, O. Wieland, K. Wimmer,

H. J. Wollersheim, P. Woods, A. Yaneva, I. Zanon, J. Zhao, R. Zidarova, S. Ziliani, G. Zimba and A. Zyriliou.

Decay studies in the $A \sim 225$ Po-Fr region from the DESPEC campaign at GSI in 2021.

IL Nuovo Cimento C 045 (2022).

- M. Górska, H. M. Albers, T. Arici, A. Banerjee, G. Benzoni, A. Blazhev, B. Cederwall, B. Das, T. Davinson, J. Gerl, H. Grawe, O. Hall, N. Hubbard, S. Jazrawi, J. Jolie, M. Mikolajczuk, A. K. Mistry, D. Mengoni, Zs. Podolyák, M. Polettini, P. H. Regan, M. Rudigier, A. Yaneva, J. Vesic, G. Zhang.
Nuclear structure aspects of the heaviest $N \sim Z$ nuclei south of ^{100}Sn .

J. Phys.: Conf. Ser. 2453, 012027 (2023).

- A. Yaneva, S. Jazrawi, B. Das, M. Mikolajczuk, M. Górska, P. H. Regan, B. Cederwall, J. Jolie, G. Benzoni, H. M. Albers, S. Alhomaidhi, T. Arici, A. Banerjee, M. M. R. Chishti, T. Davinson, J. Gerl, O. Hall, N. Hubbard, I. Kojouharov, A. K. Mistry, M. Polettini, M. Rudigier, E. Sahin, H. Schaffner, A. Sharma, H. J. Wollersheim, P. Boutachkov, T. Dickel, E. Haettner, H. Heggen, C. Hornung, R. Knöbel, D. Kostyleva, N. Kurz, N. Kuzminchuk, I. Mukha, S. Pietri, W. R. Plass, Zs. Podolyak, C. Scheidenberger, Y. K. Tanaka, J. Vesic, H. Weick, U. Ahmed, Ö. Aktas, A. Algora, C. Appleton, J. Benito, A. Blazhev, A. Bracco, A. Bruce, M. Brunet, R. Canavan, A. Esmaylzadeh, L. M. Fraile, G. Häfner, K. P. Hucka, P. R. John, D. Kahl, V. Karayonchev, R. Kern, G. Kosir, R. Lozeva, P. Napiralla, B. S. Nara Singh, R. D. Page, C. M. Petrache, N. Pietralla, J.-M. Régis, H. Rösch, P. Ruotsalainen, V. Sanchez-Temble, L. Sexton, R. Shearman, M. Si, V. Werner, J. Wiederhold, K. Wimmer, W. Witt, P. Woods, G. Zimba
Fast-timing Measurement in ^{96}Pd : Improved Accuracy for the Lifetime of the 4_1^+ State.

Acta Phys. Pol. B Proc. Supp. 16, 4-A30 (2023).

- T. Parry, M. Armstrong, Zs. Podolyák, M. Górska, J. Acosta, Z. Q. Chen, A. Jungclaus, K. Wimmer, P. Doornenbal, N. Aoi, H. Baba, G. Bartram, F. Browne, C. Campbell, H. Crawford, H. De Witte, C. Fransen, H. Hess, S. Iwazaki, J. Kim, A. Kohda, T. Koiwai, B. Mauss, B. Moon, P. Reiter, D. Suzuki, R. Taniuchi, S. Thiel, J. A. Tostevin, Y. Yamamoto, A. Yaneva, C. Yuan

Gamma-ray spectroscopy of exotic neutron-rich nuclei in the doubly magic ^{132}Sn region.

J. Phys.: Conf. Ser. 2586, 012071 (2023)

- S. Alhomaidhi, E. Sahin, V. Werner, J. Jolie, P. H. Regan, N. Pietralla, J. Gerl, M. Górska, G. Benzoni, A. K. Mistry, N. Hubbard, G. Aggez, H. M. Albers, T. Arici, M. Armstrong, A. Banerjee, B. Das, T. Davinson, O. Hall, I. Kojouharov, P. Koseoglou, M. Mikolajczuk, Zs. Podolyák, M. Polettini, M. Rudigier, H. Schaffner, H-J. Wollersheim, A. Yaneva, P. Boutachkov, T. Dickel, E. Haettner, H. Heggen, C. Hornung, R. Knöbel, D. Kostyleva, N. Kurz, N. Kuzminchuk, I. Mukha, S. Pietri, W. Plass, C. Scheidenberger, Y. Tanaka, H. Weick, U. Ahmed, Ö. Aktas, A. Algora, C. Appleton, A. Blazhev, A. Bruce, B. Cederwall, M. M. R. Chishti, M. L. Cortes, F. Crespi, J. J. Dobon, M. Doncel, A. Ertoprak, A. Esmaylzadeh, M. L. Expósito, L. M. Fraile, J. B. García, A. Gottardo, J. Ha, S. Jazrawi, P. R. John, C. Jones, V. Karayonchev, R. Kern, L. Knafla, G. Kosir, Gregor R. Lozeva, D. Mengoni, T. J. Mertzimekis, B. Million, A. Morales, J. R. Murias, S. E. A. Orrigo, J. Pllumaj, S. Pelonis, J. Petrović, S. Pigliapoco, B. Quintana, F. Recchia, K. Rezyunkina, L. Sexton, N. Singh, P. Söderström, A. Sood, P. Vasileiou, J. Vesic, J. Wiederhold, G. Zhang, R. Zidarova, A. Zyriliou
Isomeric Lifetime Measurement in the Neutron-rich ^{189}Ta .
EPJ Web of Conf. 290, 02007 (2023)

Acknowledgements

First and foremost, I would like to express my sincere gratitude to my PhD supervisors Dr. Magdalena Górska and Prof. Dr. Jan Jolie for their continuous support, patience, and encouragement throughout my research and thesis writing process. When it comes to Dr. Magdalena Górska, throughout my PhD period she has provided me with sound advice and good teaching, making great efforts to explain things clearly and simply. We have butted heads a few times, but I remain gratefully for all the support and patience she has shown me thought the years.

I would like to extend a special thanks to Dr. Ivan Kojouharov, who has always been available to address my questions, regardless of his busy schedule. The discussions we have had were always fun and fulfilling. Attending the group seminars, journal club and engaging in stimulating discussions within the GSI gamma spectroscopy group have greatly benefited me. I have gained a lot during these, thanks to Dr. Jürgen Gerl, Dr. Hans-Jürgen Wollersheim, Henning Schaffner and Dr. Kathrin Wimmer.

I am also grateful to my many colleagues and friends at the GSI for providing a stimulating and enjoyable environment that naturally fosters learning and growth.

I also extend my gratitude towards the many people, who have contributed and helped me with data analysis and numerous other tasks related to this thesis. Arzoo Sharma, Mathias Rudigier, Michal Mikolajczuk, Biswarup Das, Gregor Kosir just to name a few.

Lastly, I am deeply indebted to my family for their unwavering support and encouragement. To my parents, who have always believed in me and encouraged my academic pursuits, and to my siblings, whose constant support has been a source of strength for me. Thank you with all my heart.

Curriculum vitae

Personal Data

Name: Aleksandrina Yaneva
Day of birth: 2 June 1995
Place of birth: Varna, Bulgaria
Nationality: Bulgarian
Address: Bachstr. 22B,
64291 Darmstadt-Arheilgen, Germany

Education history

2020 - 2024	Doctorate in Experimental Physics at University of Cologne, Cologne, Germany in cooperation with GSI Helmholtzzentrum für Schwerionenforschung, Darmstadt, Germany
2018 - 2020	M. Sc. Nuclear and Particle Physics at Sofia University "St. Kliment Ohridski", Sofia, Bulgaria
2014 - 2018	B. Sc. Physics at Sofia University "St. Kliment Ohridski", Sofia, Bulgaria
2009 - 2014	High School (Secondary Education) Diploma at First Language School, Varna, Bulgaria

Erklärung zur Dissertation

Hiermit versichere ich an Eides statt, dass ich die vorliegende Dissertation selbstständig und ohne die Benutzung anderer als der angegebenen Hilfsmittel und Literatur angefertigt habe. Alle Stellen, die wörtlich oder sinngemäß aus veröffentlichten und nicht veröffentlichten Werken dem Wortlaut oder dem Sinn nach entnommen wurden, sind als solche kenntlich gemacht. Ich versichere an Eides statt, dass diese Dissertation noch keiner anderen Fakultät oder Universität zur Prüfung vorgelegen hat; dass sie - abgesehen von unten angegebenen Teilpublikationen und eingebundenen Artikeln und Manuskripten - noch nicht veröffentlicht worden ist sowie, dass ich eine Veröffentlichung der Dissertation vor Abschluss der Promotion nicht ohne Genehmigung des Promotionsausschusses vornehmen werde. Die Bestimmungen dieser Ordnung sind mir bekannt. Darüber hinaus erkläre ich hiermit, dass ich die Ordnung zur Sicherung guter wissenschaftlicher Praxis und zum Umgang mit wissenschaftlichem Fehlverhalten der Universität zu Köln gelesen und sie bei der Durchführung der Dissertation zugrundeliegenden Arbeiten und der schriftlich verfassten Dissertation beachtet habe und verpflichte mich hiermit, die dort genannten Vorgaben bei allen wissenschaftlichen Tätigkeiten zu beachten und umzusetzen. Ich versichere, dass die eingereichte elektronische Fassung der eingereichten Druckfassung vollständig entspricht.

Teilpublikationen:

A.Yaneva et al., "Fast-timing measurement in ^{96}Pd : Improved accuracy for the lifetime of the 4_1^+ state", Acta Phys. Pol. B Proc. Suppl. 16, 4-A30 (2023)

A.Yaneva et al., "The shape of the $T_z = +1$ nucleus ^{94}Pd and the role of proton-neutron interaction on the structure of its excited states", Phys. Lett. B 855, 138805 (2024)

A.Yaneva et al., "Seniority mixing in ^{96}Pd ", (manuscript in preparation)

Darmstadt, 18.06.2024

(Place, Date)



(Aleksandrina Yaneva)